Fermi Surfaces and Where to Find Them:

Quantum Oscillations in Kondo Insulators and High-Temperature Superconductors

Máté Hartstein

Cavendish Laboratory

University of Cambridge

This dissertation is submitted for the degree of

Doctor of Philosophy

Magdalene College February 2021

Declaration

This dissertation is the result of my own work and includes nothing which is the outcome of work done in collaboration except as declared in the Preface and specified in the text. It is not substantially the same as any that I have submitted, or, is being concurrently submitted for a degree or diploma or other qualification at the University of Cambridge or any other University or similar institution except as declared in the Preface and specified in the text. I further state that no substantial part of my dissertation has already been submitted, or, is being concurrently submitted for any such degree, diploma or other qualification at the University of Cambridge or any other University or similar institution except as declared in the Preface and specified in the text. This dissertation does not exceed the prescribed word limit of 60,000 by the Degree Committee for the Faculty of Physics and Chemistry.

The research projects were performed under supervision of Suchitra E. Sebastian. For the measurements in Chapter 4 and 5: SmB_6 and YbB_{12} single crystals were grown by Geetha Balakrishnan's group at the University of Warwick, and by Natalya Shitsevalova at the National Academy of Sciences of Ukraine. Máté Hartstein, Yu-Te Hsu and Hsu Liu cut them and electropolished them, and prepared the resistivity and torque measurements. High magnetic field measurements were performed in a group setting with colleagues from our group and supporting staff at high magnetic field facilities. Specific heat measurements on SmB_6 were performed by the Takano group at the University of Florida, and the Yamashita group at Osaka University. Thermal conductivity measurements on SmB_6 were performed by the Sutherland group at the University of Cambridge, and the Hill group at the University of Waterloo. Specific heat measurements on YbB_{12} were performed by Hsu Liu. Band structure calculations for YbB_{12} were performed by Michelle D. Johannes. Analysis of the SmB_6 measurements were analysed principally by Máté Hartstein, and analysis of the YbB_{12} measurements were analysed by Máté Hartstein and Hsu Liu. For the measurements in Chapter 6: $YBa_2Cu_3O_{6+x}$ single crystals were grown the Bernhard Keimer's group at the Max Planck Institute for Solid State Research, and by Yu-Te Hsu and Alexander J. Davies. Yu-Te Hsu and Alexander J. Davies detwinned them, added gold pads and performed the oxygen annealing. Máté Hartstein, Yu-Te Hsu and Alexander J. Davies attached wires for transport measurements, Máté Hartstein and Yu-Te Hsu prepared the torque measurements, and Máté Hartstein prepared the PDO measurements. High magnetic field measurements were performed in a group setting with colleagues from our group and supporting staff at high magnetic field facilities. Analysis of the measurements were analysed by Máté Hartstein, Yu-Te Hsu and Alexander J. Davies.

Results on SmB_6 presented in Chapter 4 have been published in Science, 349, 287–290 (2015), Nature Physics, 14, 166–172 (2018) and iScience, 23, 101632 (2020). Results on YbB_{12} presented in Chapter 5 have been published in Journal of Physics: Condensed Matter, 30, 16LT01 (2018). Results on $YBa_2Cu_3O_{6+x}$ presented in Chapter 6 have been published in Nature Physics, 16, 841–847 (2020), and Proceedings of the National Academy of Sciences, 118(7), e2021216118 (2021). A number of figures are made with inputs from Yu-Te Hsu (Figs. 4.6, 6.11, 6.12, 6.13, 6.14, 6.15), Hsu Liu (Figs. 4.1, 4.12, 5.1, 5.2, 5.4, 5.6, 5.7), Alexander J. Davies (Figs. 6.11, 6.14), and Alexander J. Hickey (Figs. 6.18, 6.19).

Máté Hartstein
February 2021

Abstract

The Fermi surface is a geometric concept that codifies the momenta of all electrons at the Fermi level. It is these electrons that underpin most physical properties of metals, and have made quantum oscillations, the experimental manifestation of the Fermi surface, a hallmark signature of metals. In this thesis we have studied systems that are distinctly non-Fermi liquid, and discovered that, contrary to this canon, quantum oscillations occur even in the absence of a Fermi liquid. We present the high magnetic field studies of two classes of correlated electron systems. We survey the striking quantum oscillations in the magnetisation of SmB_6 and YbB_{12}, two strongly-correlated Kondo insulators. We also present magnetic and transport measurements of underdoped $YBa_2Cu_3O_{6+x}$, a high-temperature superconductor, that prompt us to reinterpret the quantum oscillations previously associated with the non-superconducting normal state.

The surprising observation of quantum oscillations in the magnetisation of Kondo insulating SmB_6, but unaccompanied by oscillations in the electrical resistance, has attracted much attention. Here, we detail magnetic torque measurements that establish the intrinsic, bulk nature of the quantum oscillations, and reveal a moderate angular dependence of the oscillation frequencies, characteristic of a bulk, three-dimensional Fermi surface. We identify a finite linear specific heat coefficient down to the lowest temperatures, a distinguishing feature between metals and insulators. We demonstrate that the measured finite linear specific heat coefficient is in good agreement with the density of states at the Fermi level estimated from quantum oscillations. The unconventional nature of the ground state of SmB_6 is further evidenced by a non-zero thermal conductivity that is enhanced in a magnetic field. Through an extensive suite of characterisation techniques we confirm the high purity of our single crystals, with material properties consistent with an impurity concentration of less than 0.05%, and therefore further establishing the intrinsic character of the observed quantum oscillations.

In the search for other non-Fermi liquids that are host to a Fermi surface, we identify YbB_{12} as the second Kondo insulator that exhibits intrinsic, bulk quantum oscillations. We present a detailed study of the de Haas–van Alphen oscillations, corresponding to a heavy semimetal Fermi surface. Our results show many similarities with the ground state of SmB_6, including the large absolute size of the quantum oscillations and a finite linear specific heat coefficient, but also some key differences, namely the heavy effective masses and the proximity to a magnetic-field-induced or applied-pressure-induced insulator-metal transition.

The observation of quantum oscillations in underdoped $YBa_2Cu_3O_{6+x}$ refocused efforts to understand the pseudogap ground state of cuprate superconductors. Distinct from the large hole orbits of the Fermi liquid-like overdoped regime, the pseudogap regime was found to be characterised by a small electron pocket and the absence of antinodal states. A proposal associated the quantum oscillations with a conventional metallic state that emerges at a magnetic field of ≈ 20 T, however magnetic and thermal measurements have been at odds with the destruction of the superconducting order parameter at such modest magnetic fields. We employ high-magnetic fields to explore the region characterised by quantum oscillations, in search for the origin of the missing antinodal states in underdoped $YBa_2Cu_3O_{6+x}$, and the true extent of superconductivity. We find that the measured quantum oscillations display a signature sawtooth waveform, that rule out vestigial residual density of states, and instead point towards a complete gapping of the antinodal regions. We present current-dependent transport measurements performed in DC magnetic fields, down to millikelvin temperatures, that reveal the high-field superconducting state to be characterised by non-ohmic signatures associated with a quantum vortex matter state. In contrast to previous proposals, the quantum oscillations are found to occur well within this gapped vortex phase, as established by their co-existence with zero resistivity and hysteretic torque magnetisation, that are found to persist to magnetic fields beyond 45 T.

Table of contents

Chapter 1

Introduction

Condensed matter physics has had many triumphs over the course of its history, ranging from theoretical discoveries that preceded congruent developments in high energy physics (e.g. the Anderson-Higgs mechanism [1]), to experimental achievements that became the foundation of entire industries [2]. Its success is undoubtedly related to its potential to be a playground for phase phenomena, with different materials essentially governed by their own modified laws of physics, whether through modified interaction strengths or quasiparticle masses. Experiments can take advantage of this through the careful tuning of material properties by changing parameters such as doping, applied pressure, magnetic field, or temperature, thus enabling the study of the evolution between different phases. This pliability is coupled with the important role held by emergence, the notion that addresses why an ensemble is often found to behave dramatically differently than what would be expected from its constituents. An example pertinent to the work presented here is that of impurities which usually act to reduce crystalline order, but under certain conditions, they lead to unexpected behaviour. Such a behaviour is demonstrated by the Kondo effect, where magnetic impurities in metals transform the material into a strongly correlated insulator. Another unexpected behaviour manifests in type-II superconductors, where disorder works to pin vortices, therefore making the superconducting vortex solid phase more resilient.

Many of the advancements in condensed matter physics have been driven by experiments. We only have to go as far as the examples from above: the discovery of both Kondo insulators [3] and high-T_c superconductors [4] came as surprises at the time and presaged any theoretical predictions. Choosing a future direction for research is often a contest between problem solution and problem formulation. It is impossible to judge if efforts dedicated to pushing the boundaries for already existing tools (e.g. improving measurement sensitivity, building a record-breaking magnet) or to the development of entirely new tools will prove to be more influential. It is just as crucial to acknowledge that major breakthroughs often appear as a challenge to prevailing scientific orthodoxy, and can deter researchers from pursuing them further. Lev Landau, in his paper where the idea of Landau quantisation originates from [5], predicted oscillations in magnetisation as the magnetic field is varied, however deemed it to be experimentally unobservable, and therefore the idea of quantum oscillations was dismissed. A similar story unfolds about the discovery of unconventional superconductivity. A superconducting transition was first found in magnetic UBe_{13} [6], four years before similar reports for $CeCu_2Si_2$ [7], but the result was considered an artefact caused by filamentary superconductivity. We have the advantage of hindsight, but it is still unfortunate that with the potential upside of these early results, there was not enough impetus for further inspection.

In this thesis we focus on strongly correlated electron systems. The physical properties of most metals and semiconductors are well-understood using Fermi liquid theory. Challenge lies in materials that don't fall in this category, namely materials that exhibit instabilities of the Fermi liquid or even the breakdown of Fermi-liquid behaviour, rendering the conventional quasiparticle picture ineffective. Certainly, this area of condensed matter physics has many unsolved questions; here we attempt to tackle some of them.

It is fundamentally understood that in metals the charge-carrying electrons flow freely, while in insulators they are stuck in place, resisting forces exerted by an electric or magnetic field. This dichotomy is further demonstrated by their respective band structures, with the electrons in a metal having energy states available to them right above the highest occupied energy state, whereas electrons in an insulator are separated from the lowest lying empty energy state by a charge gap (see Fig. 1.1). This also means that there exists a Fermi surface for metals (the locus in momentum space defined by the electrons at the Fermi level), but no such Fermi surface can be defined for insulators.

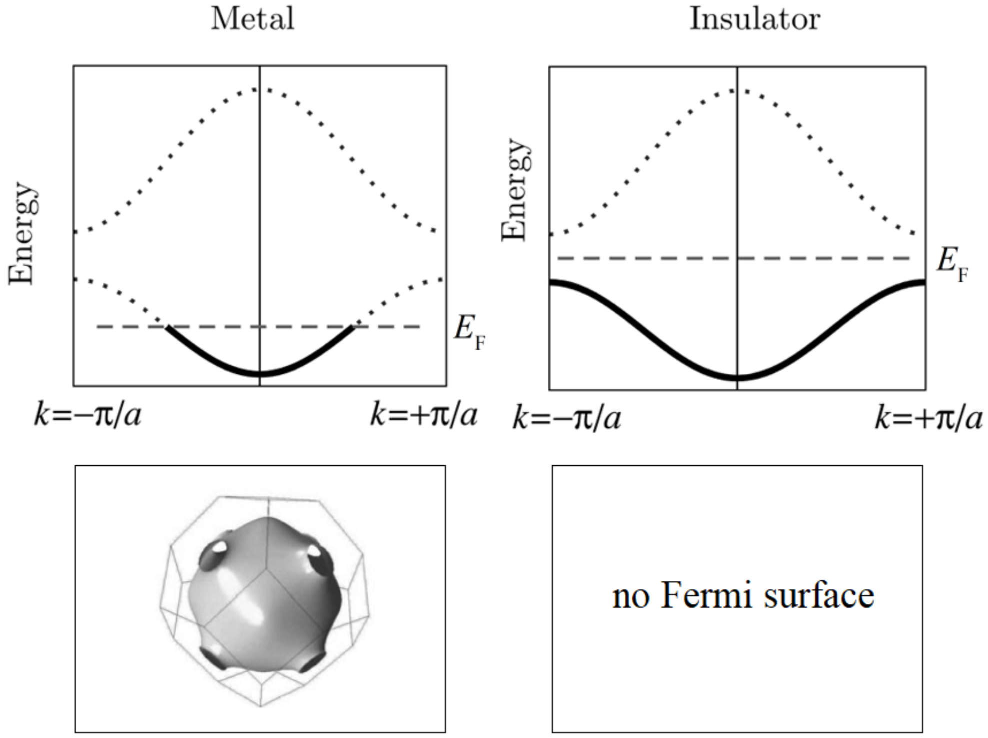

Fig. 1.1 The band structure of a metal showing a half-filled valance band. The states at the Fermi level (E_F) form a locus in momentum-space, leading to a large, three-dimensional Fermi surface, a hallmark signature of metals. This is contrasted with the band structure of an insulator, which has no states at the Fermi level, and therefore no Fermi surface. Adapted from Ref. [8].

SmB_6 is the earliest known example of a Kondo insulator [3], a material that becomes an insulator at low temperatures due to collective hybridisation between localised f- and itinerant d-electrons (see Fig. 1.2). This is why it was so surprising when quantum oscillation were first observed in SmB_6 [9, 10]. Quantum oscillations have been the hallmark signature of metals ever since they were first observed in copper, and according to the conventional theory of quantum oscillations, their observation in SmB_6 would require that the charge carriers form cyclotron orbits covering distances of the order of 100 nm. How could this be possible in a highly resistive insulator, where, under an applied electric current, charge carriers traverse no further than 10^{-4} nm before scattering? Ref. [9] associated the quantum oscillations with a topological surface state, a unit cell thick surface layer that is host to conduction electrons, whereas Ref. [10] found evidence that the oscillations are coming from the bulk of the material,

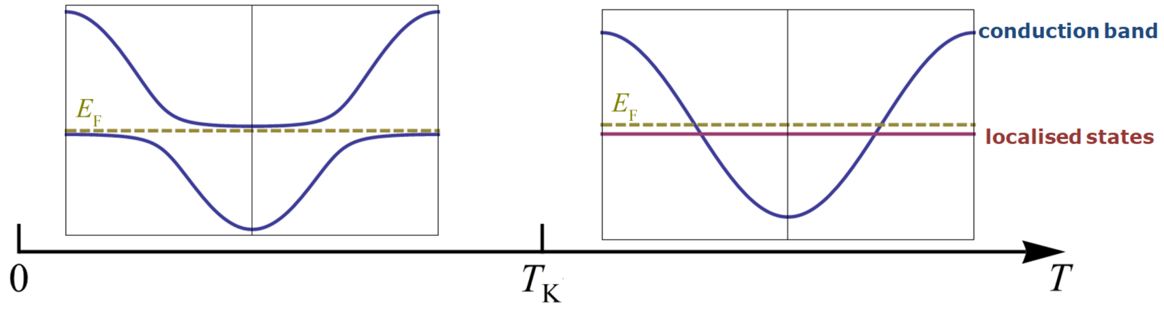

Fig. 1.2 The gapped band structure of Kondo insulators at low temperature and the metal-like band structure at room temperature. The band structure undergoes a hybridisation below the Kondo temperature T_K. This transformation manifests in a dramatic change in physical properties, including the development of a charge gap, an exponential increase in resistivity, and localized magnetic moments forming Kondo singlets.

a vastly different scenario. In this thesis we present results that reinforce the interpretation that quantum oscillations in SmB_6 originate from the insulating bulk, and identify YbB_{12} as the second Kondo insulator that is host to quantum oscillations [11, 12]. These materials present a remarkable experimental opportunity to measure something that challenges former scientific thinking. The observed dual metallic-insulating behaviour in the case of both materials constitutes a startling repudiation of known theories of insulators, contradicting the premise that Fermi surfaces are a signature of Fermi liquids alone [13].

The discovery of high-temperature cuprate superconductors in 1986 [4] was truly a breakthrough. It was the refutation of the long-held view that superconductivity was limited to temperatures below 40 K. It established the family of copper-oxides as a new class of superconductors, even though previously they would have been considered some of the least likely candidates due to their antiferromagnetic parent state and bad conduction properties. The discovery kickstarted a very exciting period of research, however many questions about the nature of superconductivity in these materials still remain. In this thesis we focus on $YBa_2Cu_3O_{6+x}$, arguably the most studied superconductor (and deservedly coined ’superconductor for grownups’). It was the first truly high-T_c superconductor with a critical temperature above the boiling point of liquid nitrogen [14], and the first cuprate to show quantum oscillations [15].

Some of the most important questions pertain to its magnetic phase diagram. The magnetic field–temperature phase diagram of conventional type-II superconductors is well-understood (Fig. 1.3a). At low magnetic fields and temperatures, they exist in the Meissner phase, which is characterised by perfect phase coherence, and therefore long-range order, and the complete expulsion of any applied magnetic field. For magnetic fields $> H_{c1}$ flux lines penetrate the material, leading to a 'crystalline' vortex lattice, with vortices arranged in a triangular Abrikosov lattice. The extent of this phase is marked by the H_{c2} line, where the superconducting order parameter disappears, giving way to the normal state. We highlight the natural analogy between the superconducting phases and the magnetic phases we are familiar with from undergraduate-level physics [16]. In this analogy the Meissner phase with its uniform phase corresponds to ferromagnetic order, whereas the vortex lattice has a periodic phase coherence that makes it analogous to antiferromagnetic order.

In the case of high-T_c superconductors the shorter coherence lengths ξ and the greater relevance of thermal fluctuations lead to a more intricate phase diagram (Fig. 1.3b). The region of the phase diagram with a superconducting order parameter is now shared by the vortex lattice and the vortex fluid phases. The transition between the two is the vortex melting transition, where the vortices become mobile, destroying phase coherence and long-range order, and leading to finite resistivity. This makes the vortex fluid phase analogous to the paramagnetic phase. Huse, Fisher, and Fisher proposed the existence of a vortex glass phase within the vortex lattice region with strong fluctuations [16]. Disorder is expected to disrupt the 'crystalline' lattice, precipitating in randomly located frozen vortices. The name was inspired by the similarities with the magnetic spin glass phase. Huse, Fisher, and Fisher also pointed out the notable field resilience of the vortex lattice phase in high-T_c superconductors, as H_{c2} is expected to scale with ξ^{-2}, and the small coherence lengths characterising the high-T_c superconductors indicate upper critical fields in excess of 100 T [16].

A recent body of work argued for an unusually small H_{c2} of ≈ 20 T for underdoped $YBa_2Cu_3O_{6+x}$, with the vortex lattice phase terminating at the same magnetic field [18], and associated the observed quantum oscillation with the normal state. The resulting phase diagram is consistent with neither the type-II or high-T_c picture. In this thesis we investigate these claims

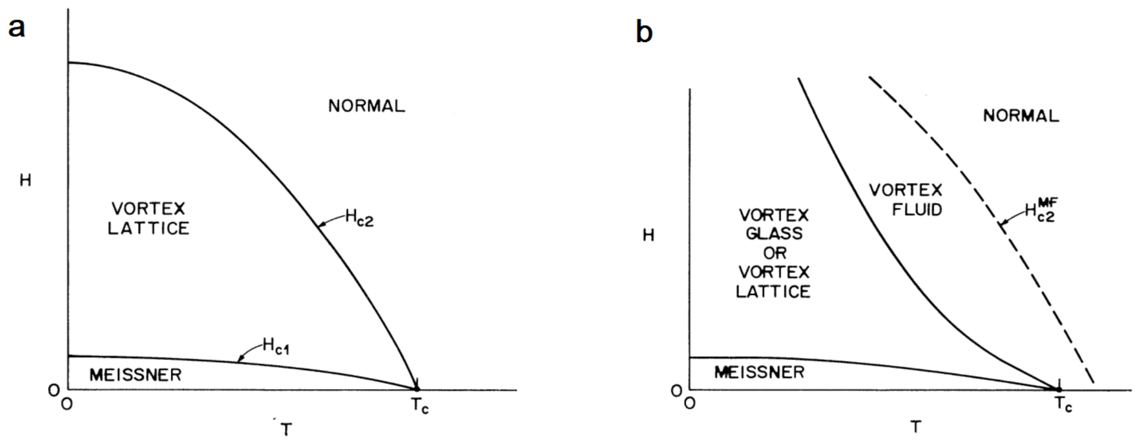

Fig. 1.3 (a) The schematic magnetic field (H) – temperature (T) phase diagram of a conventional type-II superconductor, showing a sharp phase transition between the vortex lattice and normal phases. (b) The magnetic phase diagram of a type-II superconductor with strong thermal fluctuations (such as high-T_c superconductors) based on the model by Fisher, Fisher, and Huse (FFH) [17]. The phase diagram is characterised by a field-resilient vortex lattice phase, and a phase-incoherent vortex liquid phase, with the crossover from the vortex lattice phase occuring near the mean-field H_{c2} transition, but rendered washed out. Adapted from Ref. [17].

by exploring the phase diagram through electrical transport and magnetic torque measurements. We access the previously unexplored regime of millikelvin temperatures and high magnetic fields, unaffected by eddy currents present in pulsed magnetic fields. Our results reveal a field-resilient vortex lattice phase and a phase diagram consistent with the high-T_c picture. The refutation of the normal state description brings back to the fore one of the cardinal questions of the field: what is the low-temperature ground state of the underdoped cuprates? To this end we present high-resolution quantum oscillation measurements as a result of improved sample quality and measurement sensitivity, and identify a single nodal Fermi surface pocket that reflects the pseudogap. The suite of experimental results we present highlights the relevance of a superconducting order parameter even at high magnetic fields, and prompts us to interpret the low temperature ground state outside the context of Fermi liquid theory.

The outline of this dissertation is as follows: Chapter 2 discusses relevant theoretical concepts. Chapter 3 describes the experimental details of the high magnetic field measurements discussed in subsequent chapters. Chapter 4 presents quantum oscillation measurements of the strongly correlated insulator SmB_6, together with thermal measurements and material quality tests. Chapter 5 discusses the discovery of quantum oscillations in a second Kondo insulator, YbB_{12}. Chapter 6 presents electrical transport and magnetic torque measurements of underdoped $YBa_2Cu_3O_{6+x}$, that aid the reinterpretation of its magnetic phase diagram, and underline many of the still outstanding questions pertaining to its ground state. Chapter 7 summarises the conclusions drawn from the work presented here, and outlines future research ideas.

Chapter 2

Relevant theoretical aspects

2.1 The Doniach model and Kondo insulators

Looking at the history of the field, we find that the first experimental evidence of the low-temperature insulating state in SmB_6 [3], and therefore the first example of a Kondo insulator, came before the term heavy fermion was coined [7], and still before the Kondo lattice picture was developed [19]. Breaking from the historic narrative, here we introduce these theoretical concepts first. The Kondo effect, proposed by Jun Kondo in 1962 [20], describes the interaction of a magnetic ion embedded in a non-magnetic metallic host with its conduction electrons. There is a coupling between the two spins, quantified by the Hamiltonian

$$H = -J\boldsymbol{S_i} \cdot \boldsymbol{S_e}$$

where J is the coupling term between the spin of the magnetic ion $\boldsymbol{S_i}$ and the spin of the electron $\boldsymbol{S_e}$. It is energetically favourable for the system to minimize the energy resulting from the interaction by screening the spin of the magnetic impurity, leading to the formation of a non-magnetic Kondo singlet. It yields a characteristic energy scale defined by the coupling term J and the density of states of the conduction electrons at the Fermi energy $g(E_\mathrm{F})$, given by

$$k_\mathrm{B} T_K \propto \frac{1}{g(E_\mathrm{F})} e^{-\frac{1}{Jg(E_\mathrm{F})}}$$

The Kondo temperature T_K emerges as the characteristic temperature below which Kondo singlets are formed. Originally, the Kondo effect was invoked to explain the resistance minima observed at low temperatures in dilute magnetic alloys [21].

Many materials can be described as a dense lattice of magnetic ions, for which one can expand the Kondo effect to serve as the basis of the Kondo lattice effect, by assuming a magnetic impurity at every lattice site. A competing long-range exchange interaction exists between localized magnetic impurities, called the Ruderman-Kittel-Kasuya-Yosida (RKKY) exchange interaction, innate to atoms with highly localized f-electrons. Here the spins of the f-shells are shielded by the conduction electrons, so only an indirect exchange is possible by inducing a spin polarisation in the conduction electrons that is then felt by a different magnetic ion. This couples them over long distances, leading to long range magnetic order and the emergence of the energy scale

$$k_{\mathrm{B}} T_{\mathrm{R}KKY} \propto J^2 g(E_{\mathrm{F}})$$

characterised by $T_{\mathrm{R}KKY}$.

We see that both energy scales are dependent on the coupling term J and the density of states $g(E_{\mathrm{F}})$. For different J, different interactions will be dominant. The RKKY interaction favours magnetic order, while the Kondo interaction will try to compensate for magnetic spins. This interplay leads to the Doniach phase diagram (Fig. 2.1). As J increases, a long range magnetic order appears (non-zero Néel temperature T_N), however it reaches a maximum as the Kondo interaction becomes more relevant. When the two effects are equal and opposite for J_c, the system reaches a quantum critical point (QCP), where the two ground states are degenerate. By further increasing J, we tune away from this point. Ultimately, heavy-fermion properties are realised in the intermediate region, when a hopping term between sites is introduced, that leads to mobile heavy quasiparticles.

To show that the origin of heavy fermions lies in the Kondo effect, we return to Jun Kondo's original paper [21], where he predicted a logarithmic term in the scattering cross-section, that would diverge as the electronic energy approaches the Fermi energy. Soon Henry Suhl recognised [23], that the singularity is replaced by a resonance in the electronic scattering amplitude centred at the Fermi energy, now called the Abrikosov-Suhl or Kondo resonance.

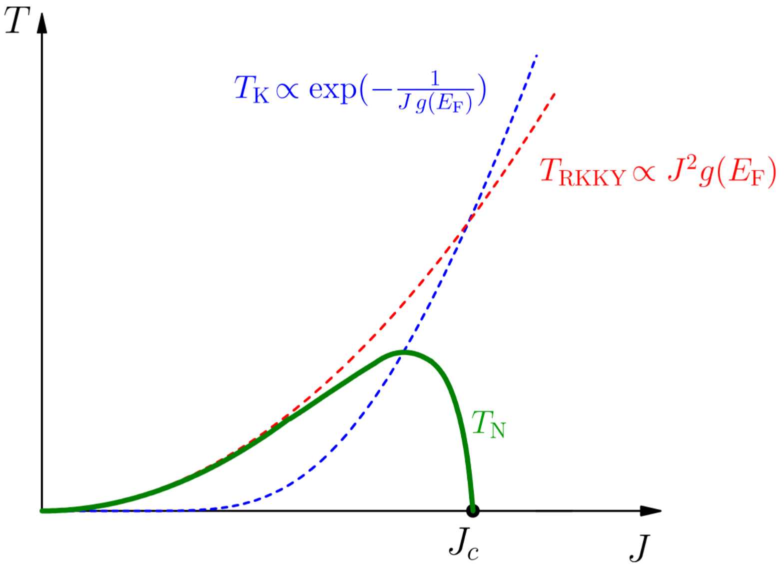

Fig. 2.1 The Doniach phase diagram demonstrates the evolution of the Kondo and RKKY energy scales with respect to the coupling term J, and its effect on the magnetic transition temperature T_N. As the energy scales become comparable, magnetism is suppressed and the system reaches a quantum critical point at J_c. It is this intermediate region where strong correlations and heavy-fermion physics are expected (from Ref. [22]).

This introduces a peak in the density of states for the conduction electrons below the Kondo temperature T_K, which is what enhances both the effective mass and the specific heat coefficient, the characteristic properties of heavy-fermions at low temperatures.

When lowering the temperature below T_K the screening of local moments by the Kondo effect is amplified, leading to phase coherence between scattering sites, and resulting in a drop in the electrical conductivity and the magnetic susceptibility. Many heavy-fermion systems develop superconductivity at low temperatures. However, in the special case of a half-filled Kondo lattice, there is no hopping term and no mobile quasiparticles, and instead, phase coherence leads to an increase in resistivity corresponding to a charge gap of order T_K. Thus, we establish that Kondo insulators are a special class of heavy fermions. We also find that such insulating behaviour is sensitive to disorder, as small amounts of impurities can lead to either hole or electron doping that reintroduces mobile quasiparticles.

2.2 Quantum oscillations

The measurement of the Fermi surface is vital for understanding the electronic structure of metals, as it is the electrons near the Fermi level that have the biggest influence on electronic, and therefore most physical properties. Out of complementary techniques, quantum oscillation measurements provide the highest k-space resolution for characterising Fermi surfaces. Further strengths are that all crystallographic directions can be accessed with equally high resolution, and that the dataset required for the characterisation of a Fermi surface also allows numerous other quantities of the sample to be extracted (i.e. effective mass, mean free path, etc.). The limiting factor is usually sample quality, with impurities that lead to damping, making the quantum oscillation signal difficult to resolve even at the highest magnetic fields and extremely low temperatures. With so many great primers on the theory of quantum oscillations [13, 24, 25], here we omit a derivation of the theory and present a brief overview of the results that we apply in later chapters of this thesis.

The basic phenomenon behind quantum oscillations is that in the presence of a magnetic field B, the electrons form cyclotron orbits, each with quantized energy levels, known as Landau levels, separated by $\Delta E = \hbar\omega_c$. These orbits can be thought of as concentric tubes in k-space (Fig. 2.2). ω_c is proportional to the magnetic field B, so by increasing B, the tubes move through the Fermi surface one by one, resulting in oscillatory changes in the chemical potential Ω, periodic in $1/B$. Importantly, the frequency F is related to the cross-sectional area A_k of the Fermi surface perpendicular to B via the Onsager relation,

$$A_k = 2\pi eF/\hbar$$

All slices of the Fermi surface give rise to oscillations of varying phase and frequency, however slices that do not correspond to extremal areas cancel out due their varying phase, leading to a small number of oscillatory frequencies as a function of inverse magnetic field that manifest in the chemical potential. Measuring these frequencies for different field orientations allows one to uncover the entire Fermi surface.

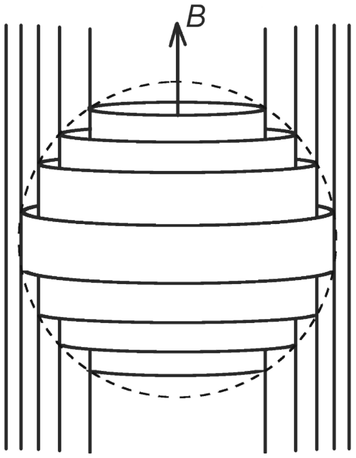

Fig. 2.2 The Landau level tubes in *k*-space inside a spherical Fermi surface, that pop through the Fermi level as the magnetic field increases, leading to the oscillatory behavior in the chemical potential and derived quantities with respect to magnetic field (from Ref. [13]).

The same oscillatory changes appear in derived quantities of the chemical potential. Quantum oscillations in magnetic torque τ or magnetisation M are called the de Haas–van Alphen effect, and quantum oscillations in resistivity ρ are called the Shubnikov–de Haas effect, both described by the Lifshitz–Kosevich (LK) equation (see Refs. [13, 24] for an extensive treatment). The formula in its most digestible form is

$$M,\, \rho \propto \sum_F D \cdot R_\mathrm{T} R_\mathrm{D} R_\mathrm{S} \cdot \sin(2\pi F/B + \phi)$$

where F is the oscillation frequency corresponding to an extremal cross-section area of the Fermi surface, B is the applied magnetic field, ϕ is the phase, $R_\mathrm{T} R_\mathrm{D} R_\mathrm{S}$ are different phase smearing terms that attenuate the oscillations, and D is the prefactor, which is dependent on what physical quantity is measured and whether the Fermi surface is three-dimensional and two-dimensional.

Theoretical amplitude of de Haas–van Alphen oscillations

Imperative for the comparison of the measured amplitude of quantum oscillations to the theoretical estimate from the Lifshitz–Kosevich theory is the value of the prefactor D. Here, we

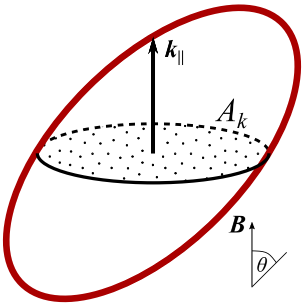

Fig. 2.3 The extremal cross-sectional area A_k and the Fermi wavevector along the applied field direction $k_{\parallel}$ in the case of an ellipsoidal Fermi surface.

discuss what the prefactor is in the case of de Haas–van Alphen oscillations in magnetisation originating from a three-dimensional and a two-dimensional Fermi surface.

The theoretical amplitude for a three-dimensional Fermi surface as defined by the prefactor is (derived in Chapter 2 of Ref. [13])

$$D_{3\mathrm{D}} = f(r)\frac{8m_e}{m^*}\left(\frac{k_\mathrm{F}}{k_\mathrm{BZ}}\right)^3\sqrt{\frac{B}{8F}}$$

Here, m_e is the free electron mass, m^* is the effective mass, k_F is the Fermi wavevector, $k_\mathrm{BZ} = 2\pi/a_{\mathrm{u.}c.}$ is the size of the Brillouin zone, $a_{\mathrm{u.}c.}$ is the lattice constant, F is the quantum oscillation frequency, and $f(r)$ is the anisotropy term defined as

$$f(r) = \sqrt{\frac{2\pi}{|A_k''|}} = \sqrt{\frac{2\pi}{\left|(\partial^2 A_k)/(\partial k_{\parallel}^2)\right|}}$$

Here, $k_{\parallel}$ is the Fermi wavevector along the applied field direction, and A_k is the extremal cross-sectional area of the Fermi surface perpendicular to the applied magnetic field (see Fig. 2.3). A_k'' is the curvature factor that accounts for the number of states that contribute to the extremal orbit. For an ellipsoidal Fermi surface, which we consider in later chapters, it can be shown that the curvature factor is given by $A_k'' = 2A_k/k_{\parallel}^2$ [13]. Our expression for $D_{3\mathrm{D}}$ gives the amplitude of the quantum oscillatory magnetisation in units of Bohr magnetons μ_B per unit cell.

The theoretical amplitude for a two-dimensional Fermi surface is a bit more straight-forward. It is given by the carrier density per unit surface area n, normalised by the effective mass of the quasiparticles m^* (based on Appendix 7 of Ref. [13])

$$D_{2\mathrm{D}} = n a_{\mathrm{u}.c.}^2 \frac{2m_e}{\pi m^*}$$

where $n = 2\pi k_{\mathrm{F}}^2/(2\pi)^2$, accounting for a factor of 2 for spin degeneracy. The expression becomes

$$D_{2\mathrm{D}} = \frac{4m_e}{m^*}\left(\frac{k_{\mathrm{F}}}{k_{\mathrm{BZ}}}\right)^2$$

where k_{BZ} is the size of the Brillouin zone, and k_{F} is the Fermi wavevector. Again, the expression is for the quantum oscillatory magnetisation in units of Bohr magnetons μ_{B} per unit cell.

The envelope of the quantum oscillations for various physical quantities

The field dependence of the prefactor D varies for different physical quantities, which leads to different envelopes for the quantum oscillations as a function of magnetic field. The field dependence is particularly important when fitting to the measured quantum oscillations with the Lifshitz–Kosevich equation, which is often done to obtain different quantities such as the impurity damping factor. In the previous section we established that for a three-dimensional Fermi surface the envelope of quantum oscillations in magnetisation has a field dependence of $B^{1/2}$. Below, we summarise the field dependence of the envelope for the most common physical quantities.

$$\tau = |\boldsymbol{M}|\,|\boldsymbol{B}| \propto B^{3/2}$$

$$M = -grad_B\Omega,\ \rho \propto B^{1/2}$$

$$\chi = \frac{dM}{dB} \propto B^{-3/2}$$

For a two-dimensional Fermi surface, the powers would be reduced by a further 1/2.

Phase smearing terms

One must account for the effects of finite temperature, sample purity, and electron spin, which all lead to the attenuation of the quantum oscillation amplitude.

For finite temperature, the density of states around the chemical potential is broadened by the Fermi–Dirac distribution, which in turn leads to phase smearing given by

$$R_{\mathrm{T}} = \frac{X}{\sinh X}, \quad X = \frac{2\pi^2 k_{\mathrm{B}} T m^*}{e\hbar B}$$

where T is the temperature, m^* is the effective mass and B is the applied magnetic field. Due to this factor, quantum oscillation measurements are best resolved at low temperatures. This dependence on the temperature can also be used to its advantage by taking measurements at different temperatures, and fitting to the temperature dependence to obtain a value for the effective mass m^*.

As previously mentioned, one of the biggest obstacles for quantum oscillation measurements is sample quality. Meaningful measurements can only be carried out for high purity crystals. This difficulty arises from quasiparticles that decay before completing a cyclotron orbit, and leads to the attenuation of the quantum oscillation signal via the phase smearing term

$$R_{\mathrm{D}} = \exp\left(-\frac{B_0}{B}\right)$$

Here B_0 is the damping factor (also denoted as Γ' in Chapter 6), which is related to the mean free path l as given by

$$l = \frac{\pi\hbar k_{\mathrm{F}}}{eB_0}$$

where k_{F} is the Fermi wavevector. Higher quality samples have longer mean free paths, and therefore a lower B_0, which leads to less attenuation. High magnetic fields are necessary to minimise the attenuation by the term R_{D}.

Lastly, we consider Zeeman splitting, which also has an attenuating effect on the amplitude of quantum oscillations. It is equivalent to introducing a phase shift between the oscillations corresponding to spin-up quasiparticles and spin-down quasiparticles. The term is given by

$$R_{\mathrm{S}} = \cos\left(\frac{\pi g m_s}{2 m_e}\right)$$

where g is the spin-splitting factor, m_s is the spin effective mass (renormalised by electron–electron interactions only). In contrast, the effective mass m^* obtained from the finite temperature term is renormalised by both electron–electron and electron–phonon interactions. For certain orbits the spin-splitting term can lead to the vanishing of the amplitude along particular field orientations, called spin-zeros. Identifying such angles can be used to determine the value of the spin-splitting factor g.

We note that in the zero-temperature, infinite-field limit these phase smearing terms saturate to unity. The Lifshitz–Kosevich equation has also been expanded to include other phase smearing terms, due to effects such as superconductivity [26], field inhomogeneity or mosaic crystal structure [13].

Harmonics

In an attempt to keep things simple, the equations above only account for the fundamental frequency F. In practice, harmonics of fundamental frequencies are also often seen for high-quality samples and low temperatures. When accounting for all harmonics, the Lifshitz–Kosevich equation becomes a sum over the harmonic number p for each fundamental frequency F

$$\tau,\ \rho \propto \sum_F \sum_p D_p \cdot R_{\mathrm{T},p} R_{\mathrm{D},p} R_{\mathrm{S},p} \cdot \sin(2\pi p F/B + \phi_p)$$

with the phase smearing terms

$$R_{\mathrm{T},p} = \frac{X}{\sinh X}, \quad X = p\frac{2\pi^2 k_{\mathrm{B}} T m^*}{e\hbar B}$$

$$R_{\mathrm{D},p} = \exp\left(-p\frac{B_0}{B}\right)$$

$$R_{\mathrm{S},p} = \cos\left(p\frac{\pi g m_s}{2m_e}\right)$$

We note two things. We find that the phase ϕ_p varies with harmonic number, and that the attenuation caused by phase smearing terms increase with p. An analysis of the Fermi surface based on resolving different harmonics is possible for two-dimensional Fermi surfaces at high enough magnetic fields (with 10-20 Landau levels still occupied). In this special case, instead of being constant, the chemical potential becomes pinned to the highest occupied Landau level, and oscillates with the magnetic field [27]. In the zero-temperature limit this leads to discontinuous jumps in the chemical potential as the highest occupied Landau level empties out, and jumps to the next highest occupied filled Landau level. The result is the sharp sawtooth oscillation of the chemical potential with field. It corresponds to the phases ϕ_p to be the same for all harmonics, leading to the same forward sawtooth waveform in the magnetisation. The presence of any open Fermi surface sheets, however, will lead to a more complicated dependence of the phase and the amplitude on the harmonic number, and alter this waveform [27]. This pronounced effect of the presence of any one-dimensional density of states on the quantum oscillations waveform can be used to quantify the size of any open sheets relative to the two-dimensional Fermi surface.

2.3 The specific heat and thermal conductivity within the Sommerfeld model

The Sommerfeld model was one of the early triumphs of condensed matter physics, providing a self-contained framework to interpret the physical properties of metals [8]. It was the first theory to treat electrons as fermions, by extending the kinetic Drude model through the application of the exclusion principle. It is also known as the free electron model, as it ignores all interactions between constituent particles.

The Sommerfeld model recognised the contribution of electrons near the Fermi level to the specific heat, which finally explained the measured low-temperature behaviour of the specific heat that could not be accounted for just by phonons. The expression for the specific heat at low temperatures within the Sommerfeld model became

$$C_p = \gamma T + \beta T^3$$

Here, the first term is the electronic term, with γ being the linear specific heat coefficient, which is given by

$$\gamma = \frac{\pi^2 k_{\mathrm{B}}^2}{3} g(E_{\mathrm{F}}) \tag{2.1}$$

where $g(E_{\mathrm{F}})$ is the quasiparticle density of states at the Fermi energy. In the simplest case, it can be shown that at $T = 0$ K the density of states becomes $g(E_{\mathrm{F}}) = 3N/2k_{\mathrm{B}}T_F$, where N is the total number of states and T_F is the Fermi temperature [8]. Hence, we have for the linear specific heat coefficient

$$\gamma = \frac{\pi^2}{2} k_{\mathrm{B}} N \frac{1}{T_F} \tag{2.2}$$

For the coefficient of the phonon term we have

$$\beta = \frac{12\pi^4}{5} \frac{N k_{\mathrm{B}}}{\Theta_D^3}$$

where Θ_D is the Debye temperature, the characteristic temperature where phonon mode degrees of freedom become full, and $V_{\mathrm{u.c.}}$ is the unit cell volume. Fitting with the expression for C_p to measurements can be used to estimate the value of γ and Θ_D.

The thermal conductivity is directly related to the specific heat via

$$\kappa = \frac{1}{3} C_v \langle v \rangle d$$

where $\langle v \rangle$ is the average thermal velocity, and d is the scattering length. For high purity samples phonons become boundary-limited at low temperatures, and the scattering length is given by the average sample dimension. For a sample with thickness t and width w, it is usually estimated using $d = \sqrt{4tw/\pi}$. For non-boundary limited electrons, the mean free path can be estimated from the Fermi velocity v_F and the scattering rate τ via $l = v_F\tau$, and using $T_F = m^* v_F^2/2k_\mathrm{B}$. With γ given by Eq. 2.2 the electronic part of the thermal conductivity becomes

$$\kappa_{el.} = \frac{\pi^2 k_\mathrm{B}^2 N l}{3m^* v_F} T$$

where we set the average thermal velocity to v_F. Hence, by measuring the linear coefficient of the thermal conductivity one can estimate the mean free path of the heat-carrying quasiparticles. The sound velocity, which can be determined from alternative measurements, is used for the average thermal velocity of phonons, and is given by

$$v_s = \frac{2k_\mathrm{B}}{h} \Theta_D \left(\frac{\pi}{6n}\right)^{1/3}$$

where h is the Planck constant, and n is the number density, given by $n = a_\mathrm{u.c.}^{-3}$ for a cubic crystal. By relating the sound velocity to the Debye temperature, we obtain an expression of the phonon term of the thermal conductivity just in terms of Θ_D and the temperature

$$\kappa_{ph.} = \frac{8}{5}\pi^4 \left(\frac{\pi}{6}\right)^{1/3} \frac{k_\mathrm{B}^2 d}{h a_{u.c.}^2} \frac{T^3}{\Theta_D^2}$$

This has the advantage that the Debye temperature can be obtained from measurements of the thermal conductivity that display a clear T^3. Alternatively, for datasets displaying a more complicated behaviour, the value of Θ_D inferred from specific heat can be used to estimate the phonon contribution to the thermal conductivity, which then can be subtracted away.

The Sommerfeld model allows for a quantitative comparison between the measured specific heat and the measured Fermi surface. Eq. 2.1 demonstrated the relationship between the linear specific heat coefficient γ and the density of states at the Fermi energy $g(E_\mathrm{F})$

$$g(E_\mathrm{F}) = \frac{3\gamma}{\pi^2 k_\mathrm{B}^2}$$

The quasiparticle density of states can also be expressed as an integral over the Fermi surface S with quasiparticle velocity v^*

$$g(E_\mathrm{F}) = \frac{1}{4\pi^3\hbar}\int_S \frac{dS}{|v^*|}$$

This can be calculated analytically for simpler Fermi surface shapes, such as ellipsoids. The relevant calculation for prolate ellipsoids was presented in Ref. [28], and for general ellipsoids in Ref. [29]. For a known Fermi surface, which in the case of an ellipsoidal Fermi surface amounts to determining the size of the semi-principal axes and the effective mass, the density of states can be calculated, and within the free electron model would be expected to agree with the measured electronic term of the specific heat.

Chapter 3

Measurement techniques in high magnetic fields

This chapter describes the most important measurement techniques employed during my PhD in our Cambridge lab, and also at high magnetic field labs in Tallahassee, Los Alamos, Toulouse, Wuhan, and Tokyo. The availability of central high magnetic field facilities has been a great boost for the study of phase phenomena and fermiology, making new regimes of the phase diagram accessible, and allowing the measurement of quantum oscillations in materials that proved to be a challenge at lower fields. As we demonstrated in Chapter 2, the amplitude of quantum oscillations rapidly increases with increasing magnetic field, and even an extra tesla could make the difference between observing quantum oscillations and measuring just noise. High magnetic fields also come with their own limitations. They require measurement techniques that are suitable for the small bore sizes (between 30 and 50 mm for DC magnets, and $\approx$ 10 mm for pulsed magnets). Vibrational noise becomes significant at high magnetic fields, and especially so at the peak fields of pulsed magnets. For pulsed fields, measurement techniques also have to adapt to the short duration of the pulses. Pulsed magnets can reach 60 T in 10 ms. For comparison, the maximum sweep rate of DC magnets is typically $\approx$ 0.03 T/s. Extra care needs to be taken for isothermal measurements, as the thermometers are usually not calibrated to the highest fields, and unwanted heating can lead to a temperature change that only becomes apparent at the end of a field sweep. Temperature sweeps can be especially challenging due to the time constraints during a magnet time, and therefore rehearsal sweeps at zero magnetic field are necessary to avoid wasting precious magnet time. Here we detail three measurement techniques that we have successfully employed at high magnetic fields.

3.1 Four-point electrical transport measurements

Four-point transport measurements are conceptually the most straightforward technique for measuring electrical resistivity. Four highly conductive wires, usually made out of gold or silver, are attached to the sample with silver paste or silver epoxy. The pair further apart is used to send an electric current through the sample, while the inner pair is used to measure the potential difference. This way we can measure the resistance, which can be converted into resistivity for known sample dimensions.

Realising this technique at higher magnetic fields requires a bit more finesse when preparing the samples, and the optimisation of the measurement setup. Long samples with minimal thickness (< 50 μm) are preferred to maximise the signal, especially for highly conductive samples like the cuprates at low temperatures. One should aim for low contact resistances (a few Ω), so current flowing through them does not lead to Joule heating, and to minimise their capacitive inductance that would make measurements difficult at the kHz frequencies employed in pulsed field measurements. One must ensure the wires are held firmly to the sample as the forces on the sample and wires can move them, and thus degrade the quality of the contact mid-sweep. During contacting we arrange the wires to minimise any current loops, which would lead to induced voltages as the magnetic field is varied. This is most difficult for the current wires, as those contacts are the furthest away, but can be reduced to close to zero for the Hall contacts if one lead is taken under the sample (see Fig. 3.1). Crosstalk between samples is reduced by keeping corresponding wirings away from each other. A spectrum analyser is usually employed to assess crosstalk for each channel when using DC magnets, whereas for pulsed field measurements one would inspect the Fourier Transform of the raw signal to see if any unwanted frequency peaks appear. Further difficulties arise when measuring superconductors in pulsed magnets. The suppression of the zero-resistivity superconducting

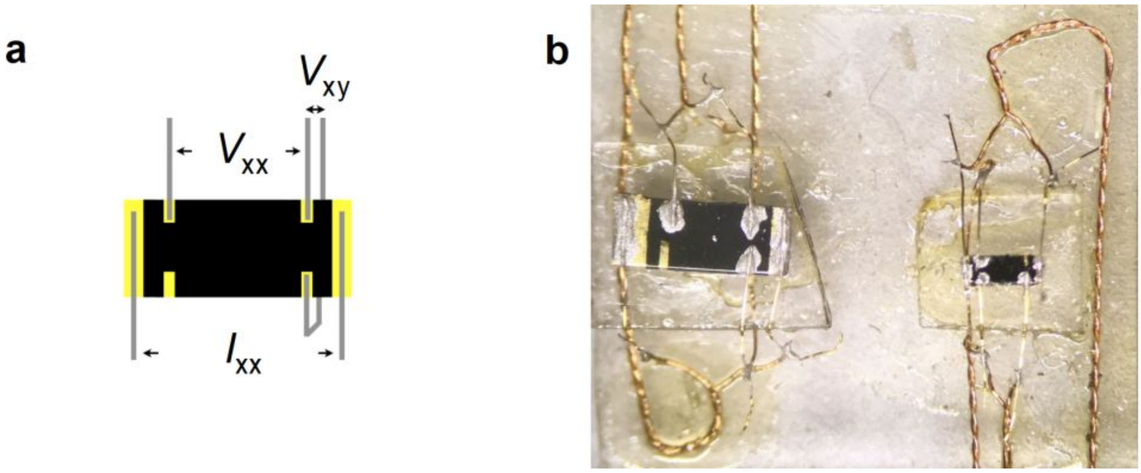

Fig. 3.1 (a) Schematic diagram of the wiring of a $YBa_2Cu_3O_{6+x}$ sample with deposited gold contacts showing the arrangement of the different current and voltage wires. I_{xx} refers to the current contact pairs, V_{xx} refers to the longitudinal voltage contact pairs, and V_{xy} refers to the Hall contact pairs. (b) Photo of two samples prepared for high magnetic field measurements following the same arrangement.

state and the generated Eddy currents results in significant heat dissipation in a very short amount of time, preventing the attainment of isothermal conditions. This effect (and any other heating) manifests in the absence of an overlap between the data measured during the up-sweep and the down-sweep parts of the magnetic field pulse. To minimise this effect, smaller samples and longer pulse lengths are necessary.

For measurements in DC magnets we employed NF Corporation SA-400F3 pre-amplifiers, in conjunction with Stanford Research Systems SR865 lock-ins, and Keithley 6221 current sources. A typical applied current was 1 mA with a frequency of a few hundred Hz. Under ideal conditions typical peak-to-peak noise was $\approx$ 10 nV, which would convert to a noise in the measured resistance of 0.01 mΩ for a current of 1 mA. For measurements in pulsed magnets we employed Stanford Research Systems SR560 pre-amplifiers with their in-built filters, or passive filters (with a fixed band pass frequency) produced by the Cavendish Electronics Workshop in combination with NF Corporation SA-400F3 pre-amplifiers. We used various National Instruments DAQs for applying a current and measuring the voltage. A typical applied current was 10 mA with a frequency between 10 and 100 kHz to avoid the frequency range dominated by vibrational noise (< 5 kHz). Under ideal conditions typical peak-to-peak noise was ≈ 1 µV, which would convert to a noise in the measured resistivity of 0.1 mΩ for a current of 10 mA.

3.2 Contactless transport measurements

A complementary technique is provided by the contactless resistivity method, which has become an established method for measuring phase transitions and Shubnikov–de Haas oscillations at high magnetic fields [30–32]. It does not provide an absolute measure of the resistivity, but accommodates similarly small samples as the 4-point method, without the tricky contact making. Furthermore, it only takes up two connections on the measurement probe for each sample, which is often a constraint on the narrow probes used in high field labs.

Here, the sample is placed on an inductor coil, which is connected to a resonant LC tank circuit. The effective inductance of the inductor coil the sample sits on is sensitive to the change in the physical properties of the material (including the sheet resistance and the magnetic susceptibility). Based on the equation for the resonant frequency f of an LC-circuit

$$f = \frac{1}{2\pi\sqrt{LC}}$$

this change in the effective inductance of the inductor coil alters the resonant frequency of the circuit. It is the resonant frequency that is measured by the proximity detector oscillator (PDO) circuit and the radio-frequency processing stage (Fig. 3.2a). The name comes from the PDO chip, which is used to compensate for the losses in the LC circuit by operating it in the negative effective resistance regime, therefore maintaining a lossless LC circuit [30]. It follows the same principles as an earlier technique based on tunnel diode oscillators (TDO). The latter is considered to have better stability, but relies on frail and expensive diodes, and has a narrower range of operating parameters. TDO circuits also operate at higher frequencies (up to GHz frequencies as opposed to ≈ 30 MHz in the case of PDO circuits), where RF effects become relevant. Another important advantage of the PDO technique is its higher operating power, which means that the resonant circuit can couple to the sample from further away, allowing it to be placed outside the cryostat. This way the circuit is under more stable conditions, as it is

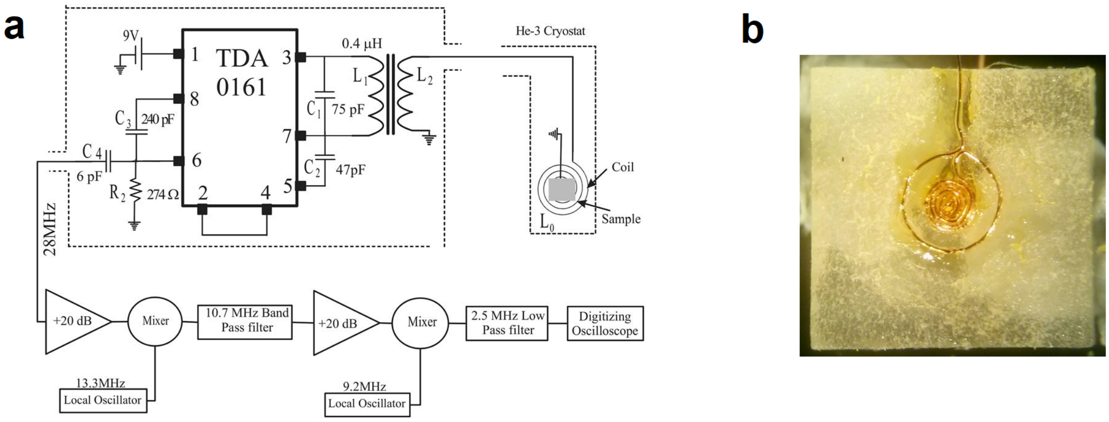

Fig. 3.2 (a) The circuit diagram for the contactless resistivity setup. The sample is mounted on an inductor coil, which is connected to the PDO LC circuit and the radio-frequency processing stage. Adapted from Ref. [30]. (b) A sample coil showing the copper wire arranged in a tightly wound spiral and a counter-wound circle, onto which the sample is glued.

not exposed to large changes in temperature and magnetic field, and can be adjusted without warming up the measurement probe.

For the PDO chip we employed an integrated circuit component from STMicroelectronics (TDA0161), which is used in metal detector circuits. From the PDO chip the signal goes through a sequence of frequency mixers and band pass filters. The goal is to mix the signal frequency to the band pass frequency of the filter, and have any noise away from this frequency filtered out. The sample coil is made out of AWG 50 enamelled copper wire. It is wound by hand on a rotary table into a spiral. One applies very thin GE varnish after every quarter of a turn to stop it from unwinding. The number of turns is defined by the size of the sample, which has to cover the entire coil. This normally means 5-6 turns, which is followed by a counter-wound circle, with an area matched to the total cross-sectional area of each 'ring' of the spiral. This acts to cancel any induced voltages generated in a pulsed magnetic field. See Fig. 3.2b for an example. The sample is then pressed down on the coil and secured with GE varnish.

The PDO circuit is made in a way to oscillate even without a load by shorting pins 2 and 4 (see Fig. 3.2a). The amplitude of the oscillations is usually reduced once the circuit is connected to the measurement probe, that leads to losses. Coupling to the sample can be improved by tuning the PDO resonant circuit we have outside the cryostat. Varying the coupling between the internal coil (L_1) and the secondary coil (L_2) by adding/removing turns from the latter can increase the oscillation amplitude of the LC-circuit. When adjusting the effective inductance of the circuit one should also maintain the resonant frequency within the optimal range of 25 MHz to 40 MHz. This is achieved by choosing the appropriate capacitor in place of C_2 once L_2 is changed (see Fig. 3.2a). Under ideal conditions the peak-to-peak noise was ≈ 50 Hz in pulsed fields, and ≈ 5 Hz in DC fields. This represents higher sensitivity when compared to four-point transport measurements. We also found the PDO technique to be less affected by vibrational noise, and to be more robust to thermal cycling, unlike four-point measurements that tend to suffer from contact degrading.

3.3 Capacitive torque measurements

An equally important avenue for the measurement of quantum oscillations is the measurement of the magnetisation, which can reveal de Haas–van Alphen oscillations. In the studies presented in later chapters we measured the magnetic torque τ, which is related to the magnetic moment $\mathbf{m}$ via

$$\tau = |\mathbf{m} \times \mathbf{B}|$$

where $\mathbf{B}$ is the applied magnetic field. Thus, measuring the magnetic torque can be used to determine the component of the magnetic moment that is perpendicular to the applied magnetic field. We used a torque magnetisation technique by means of a capacitive torque cantilever setup. Similar setups have been used for the detection of de Haas–van Alphen oscillations with great success since 1973 [33].

A schematic diagram of our torque magnetometer is shown in Fig. 3.3a. The sample is mounted on a T-shaped cantilever made out of nonmagnetic BeCu, which is anchored down at its end, similar to a diving board. Depending on the size of the sample and its magnetic moment we would use a cantilever with a thickness of 20 to 35 μm. The cantilever shown in Fig. 3.3b has an arm length of $L = 3.8$ mm, whilst its head has an area of 5.5×2.5 mm^2. This

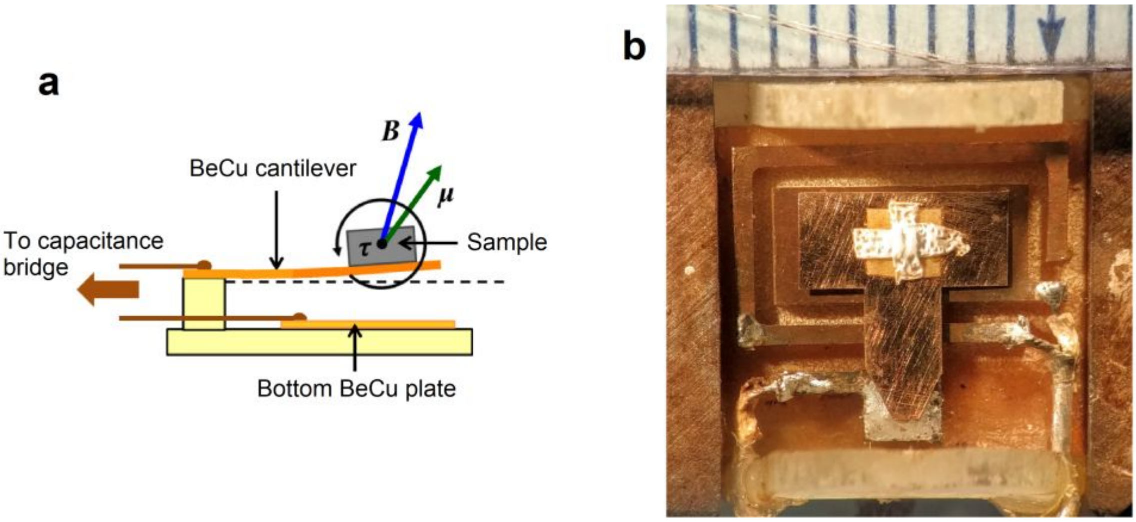

Fig. 3.3 (a) A schematic drawing of the torque cantilever setup, showing the sample mounted on a flexible BeCu cantilever, which hangs above a fixed BeCu plate below it, forming the two plates of a capacitor. Adapted from Ref. [34]. (b) A photo showing the top view of the cantilever setup, with a small sample mounted under the teflon tape. The ruler markings correspond to 1 mm.

area overlaps with a fixed BeCu plate underneath it, completing a capacitor formed by the two parallel plates. For a typical separation of 100 μm between them the capacitance is around 1 pF. A lead is attached to each plate using Gore miniature coax cables. The principle of the measurement technique is that sweeping the applied magnetic field changes the magnetic torque of the sample. This manifests in a deflection of the cantilever, which changes the separation between the cantilever and the bottom plate, therefore changing the capacitance, which we measure with a capacitance bridge. To allow for angular studies we would use measurement probes with a rotating stage. Once the magnetometer setup is prepared, but before the probe is put into the cryostat, it is important to check the full rotational range to ensure there is sufficient slack for the cables, that the cantilever does not touch the bottom plate, and that the capacitance reading behaves as expected as a function of angle. A change of 0.1 pF is possible between extremal positions just from the weight of the cantilever and the sample. Monitoring the capacitance reading during a slow cooldown is just as crucial, as the capacitance will change with temperature, and we want to avoid the cantilever pulling too much towards the bottom plate, which would increase the likelihood that they would touch at high magnetic fields. The torque cantilever setup can be calibrated to enable the conversion of the measured change in capacitance to absolute units of magnetic torque. The necessary parameters are the dimensions of the cantilever and its spring constant. The latter can be estimated from various methods: measuring the deflection for known weights, calculating it from material properties, and measuring the displacement under a magnetic field gradient (Faraday balance technique).

For our measurements we employed two kinds of capacitance bridges: the Andeen-Hagerling (AH) 2700A digital capacitance bridge, and the General Radio (GR) 1616 analogue capacitance bridge. The AH digital bridge is a self-contained instrument for measuring the capacitance in absolute units (<10 pF). It applies a maximum voltage of 15 V across the capacitor plates. The GR analogue bridge is similar to a Wheatstone bridge, but instead of measuring resistance, it measures capacitance. One can balance its reference capacitance, adjusted by the mechanical dials, to match it with the capacitance of the magnetometer setup. This leads to a voltage output of zero. As the cantilever deflects, it changes the capacitance value of the magnetometer, giving rise to a voltage output from the GR bridge, which is proportional to the difference between the reference capacitance and magnetometer capacitance. We would measure this voltage via a Stanford Research Systems SR865 lock-in. To power the capacitance bridge, we initially employed General Radio voltage sources, but they proved unreliable, with the output voltage drifting in amplitude and frequency. We achieved better performance using Stanford Research Systems DS360 low distortion function generators (maximum voltage output of 20 V), which we amplified to 100 V through a transformer built by the Cavendish Electronics Workshop.

Important for the fine-tuning of the setup are the elimination of any ground loops, and the careful choice of the frequency of each measurement channel. For this task we would use a spectrum analyser to pick the frequencies and constantly monitor the noise in the measured data. With this setup the optimal peak-to-peak noise was around $\approx 10^{-7}$ pF, which is at least an order of magnitude better than the noise performance with the AH digital capacitance bridge. Using the GR analogue bridge in conjunction with the lock-in also provides better control of the averaging and filtering of the data, and as a result yields more data points per unit time. To estimate the noise level in units of torque we use the equation

$$\tau = Lk\delta = Lkd_0\frac{\Delta C}{C}$$

where L is the cantilever arm length, k is the spring constant, δ is the deflection, d_0 is the separation between capacitor plates, ΔC is the noise in units of capacitance, and C is the capacitance of the plates without deflection. For the typical values of $L = 3.8$ mm, $k = 28$ N/m, $d_0 = 0.1$ mm, and $C = 1$ pF we get a noise level in units of magnetic torque of $\approx 10^{-12}$ Nm, which matches the noise level of similar designs [35]. In principle, the sensitivity can be further increased by choosing a thinner cantilever, which would have a smaller spring constant. However, a balance needs to be found between the magnetic moment of the sample and the cantilever thickness to avoid the non-linear deflection of the cantilever at high magnetic fields. Increasing the area of the capacitor plates, or reducing the separation between them can also improve the sensitivity, as it would make the capacitance of the magnetometer bigger. Here, the constraints are the limited space for the magnetometer, and the difficulty of achieving perfectly parallel capacitor plates that would allow for a smaller separation.

Chapter 4

Fermi surface in the absence of a Fermi liquid in SmB_6

4.1 Introduction

SmB_6 is the earliest known example of a Kondo insulator, a material with metallic properties near room temperature, that change dramatically due to the emergence of a charge gap at low temperature. In the germinal study by Menth *et al.* [3] this was evidenced by the exponential increase in electrical resistivity, but the charge gap also manifests in specific heat [36], nuclear magnetic resonance [37], point-contact spectroscopy [38], reflectivity [39], and electron tunnelling measurements [40]. Despite the low-temperature insulating state attested by the host of experimental probes, there remained an asterisk next to SmB_6 due to two low temperature properties atypical of insulators: a robust finite resistivity plateau evidenced in most existing literature on SmB_6 (persisting for different growth methods, residual resistivity ratios, and sample qualities [3, 41, 42]), and a finite linear specific heat coefficient [43] larger than that of metallic LaB_6 [36]. With the unfolding experimental and theoretical progress on topological insulators, the finite resistivity plateau in SmB_6 made the material a promising candidate to be a topological Kondo insulator [44]. The resulting experimental search established metallic surface conduction in the material [45, 46], but direct tests of its purported topological nature proved to be less conclusive. One of the first such studies presented quantum oscillations in

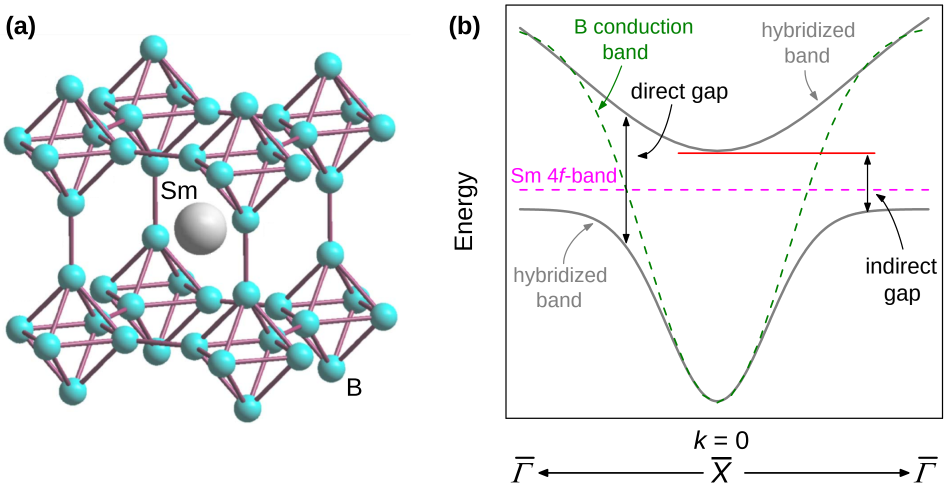

Fig. 4.1 (a) The unit cell of SmB_6 adapted from Ref. [47]. (b) Schematic picture of the band structure showing the hybridisation between the samarium $4f$-bands and $5d$-bands leading to a small indirect gap at low temperatures.

magnetisation, a measure of the bulk, unaccompanied by quantum oscillations in resistivity, the physical property governed by surface conduction, but the study still interpreted the oscillations to originate from a two-dimensional Fermi surface from topological surface states [9]. In contrast, our group reported high-frequency de Haas–van Alphen oscillations and associated them with a large three-dimensional Fermi surface from the insulating bulk [10].

In this chapter we will pick up the thread here. We will discuss the relevant physical properties of SmB_6 that make it the only Kondo insulating rare-earth hexaboride. We will then present our quantum oscillation measurements, building on earlier work [10], and establish the three-dimensional bulk nature of the quantum oscillations, which, together with the measured thermodynamic signatures, point towards a bulk Fermi surface in the absence of a Fermi liquid. Next, I discuss the range of measurements we performed to evaluate sample quality, and therefore establish the intrinsic character of the observed quantum oscillations, and conclude with a brief overview of relevant theoretical proposals.

4.2 The Kondo insulating state of SmB_6

The single crystals of SmB_6 employed in our studies were grown by the Warwick group, using the floating zone growth technique detailed in Ref. [48] and the flux growth technique, and by the Kiev group, using the floating zone growth technique. Certain measurements revealed differences between single crystals grown by the two different techniques, with results overall indicative of the lesser quality of flux-grown single crystals. We will discuss these differences later in this chapter.

SmB_6 shares the same crystal structure with other rare-earth hexaborides, generally referred to as CaB_6 structure, which is a simple cubic structure with the rare-earth atom at the centre of the unit cell and boron octahedral cages in the corners (see Fig. 4.1a).

Even before the identification of the low-temperature insulating state in SmB_6, it was discovered to be one of the earliest known examples of a mixed valence compound [49]. Normally, the samarium ions would be in the Sm^{2+} state, which corresponds to an electron configuration of $4f^6$, however in SmB_6 more than half of the samarium ions exist in the Sm^{3+} state, corresponding to $4f^5 5d^1$, with an average valence of 2.64 that reduces modestly to 2.55 at low temperatures [50]. Mixed valency is also exhibited by other f-electron Kondo insulators [51]. Gap formation is caused by the interaction between $4f$ electrons, that act as localised magnetic moments at room temperature, and the sea of conduction electrons from the broad $5d$-band, which, upon lowering the temperature, couple to form Kondo singlets and lead to a nonmagnetic state characterised by a charge gap due to the hybridisation of the two bands (see Fig. 4.1b). The Kondo insulating state precludes any magnetic order, but high-pressure experiments revealed that the insulating state can be suppressed by pressures of around 10 GPa, leading to magnetic ordering [52]. Interestingly, the insulating state has proved to be robust against even the highest accessible magnetic fields, with the charge gap surviving up to an applied magnetic field of at least 90 T [53].

Fig. 4.2a shows the measured resistivity as a function of temperature for pristine floating zone-grown single crystals of SmB_6 and LaB_6, both grown by the Warwick group using similar growth conditions. We find the resistivity of SmB_6 to increase by five orders of magnitude upon cooling, with any further increase curtailed by the low-temperature surface

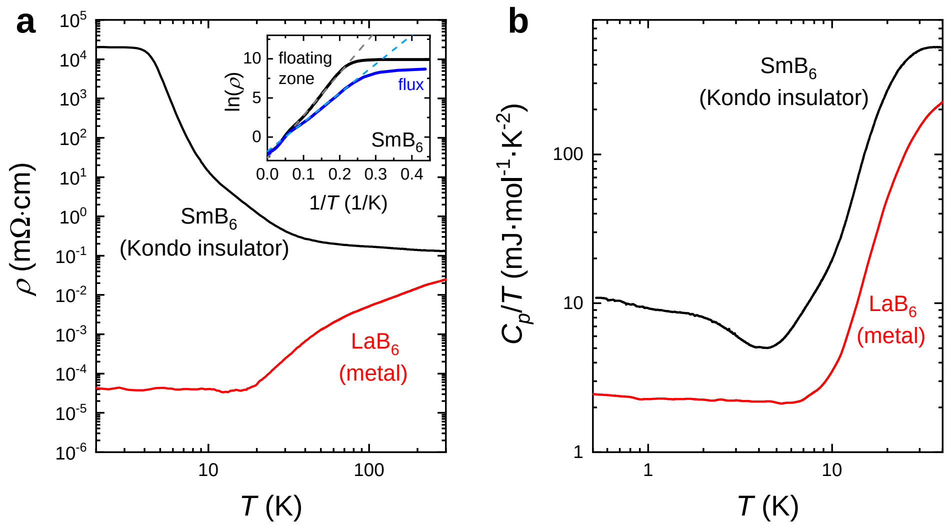

Fig. 4.2 (a) The resistivity ρ as a function of temperature for two rare-earth hexaborides, Kondo insulating SmB$_6$ and metallic LaB$_6$. SmB$_6$ shows an activated behaviour due to the Kondo gap forming at ≈ 30 K and leads to insulating behaviour at low temperatures. LaB$_6$ shows metallic behaviour with a decreasing resistivity with decreasing temperature (the noise in the data below 20 K is due to reaching the measurement limit). The inset shows the Arrhenius plot for the floating zone-grown single crystal from the main panel and a flux-grown single crystal for comparison, with linear fits marked by the dashed lines used to extract the activation gap. (b) While the electrical transport measurements show a nine order of magnitude difference in the low temperature resistivity between the two materials, the measured specific heat reveals a comparable finite specific heat divided by temperature C_p/T for the two materials, characteristic of metals (data for LaB$_6$ adapted from [54]).

conduction channel. The jury is still out for a conclusive description of this residual conductivity in SmB$_6$, and whether the surface states are topological [55]. The presence of the low-temperature resistivity plateau is found to be robust in SmB$_6$, featuring in most existing literature, although it has been shown to be affected by samarium vacancies, that push the plateau lower in temperature [56], and magnetic impurities, that lead to a lower resistivity [57] and a positive magnetoresistance [58] (as opposed to a negative magnetoresistance expected for the Kondo effect). Hence, a large value of the resistivity at low temperature and a clear plateau below 4 K are desirable for high-quality samples. Whilst the inverse residual resistivity ratio, iRRR$= \rho(2\text{ K})/\rho(300\text{ K})$, is often used to gauge sample quality, we found that the iRRR normalised by sample thickness t, iRRR$/t$, is more appropriate due to the value of the low-temperature plateau being independent of sample thickness. For our best floating zone-grown single crystals we found $\mathrm{iRRR}/t \approx 400$ (for t in µm), whereas for our best flux-grown single crystals we found $\mathrm{iRRR}/t \approx 200$.

With such a large change in resistivity with temperature, it is important to ask if it means both good metallic properties at high temperature and good insulating properties at low temperature. Based on the measured resistivity values we identify SmB_6 to be a resistive metal at room temperature and a semiconductor at low temperature. In all reports on SmB_6 the resistivity at 300 K is found to be at least 10^{-6} Ωm, which is considered fairly resistive, most likely due to Kondo scattering, and makes it comparable to nichrome, a metal often used as resistance wire. For the samples with the highest iRRR [59], the low-temperature resistivity is found to be between 10^{-1} and 10^{-0} Ωm, which makes it comparable to germanium at 10 K, a semiconductor with a gap of 10 meV [60]. In comparison, the room temperature resistivity of LaB_6, $\approx 10^{-7}$ Ωm, corresponds to a fairly good metal, a value similar to that of tin and platinum. Upon cooling we see the resistivity of our single crystal of LaB_6 drop by at least a factor of 500, which is comparable to the highest RRR found in the literature [61], a testament of the high-quality of the samples grown by the Warwick group. Such a low value of the low-temperature resistivity makes LaB_6 comparable to copper [16]. The inset of Fig. 4.2a shows the Arrhenius plot of the same floating zone-grown single crystal as the one shown in the main panel with $\mathrm{iRRR}/t = 400$, and of a flux-grown single crystal with $\mathrm{iRRR}/t = 170$. We infer an activation gap of 5 meV and 3 meV, respectively. This is representative of most samples with the activation gap of flux-grown samples usually smaller than that of floating zone-grown samples. Similar gap values were observed by nuclear magnetic resonance (NMR) [37, 62], electron spin resonance [63], and reflectivity [39].

Whilst the electrical transport measurements show a drastic nine order of magnitude difference in the low-temperature resistivity between Kondo insulating SmB_6 and metallic LaB_6, the low-temperature specific heat of the two materials look surprisingly similar. They resemble the specific heat of a metal, exhibiting a finite linear specific heat coefficient, and therefore a finite density of states at the Fermi energy (see Fig. 4.2b). For SmB_6 we find $\gamma \approx 4$ mJ·mol^{-1}·K^{-2} and for LaB_6 $\gamma \approx 2$ mJ·mol^{-1}·K^{-2}. At even lower temperatures the

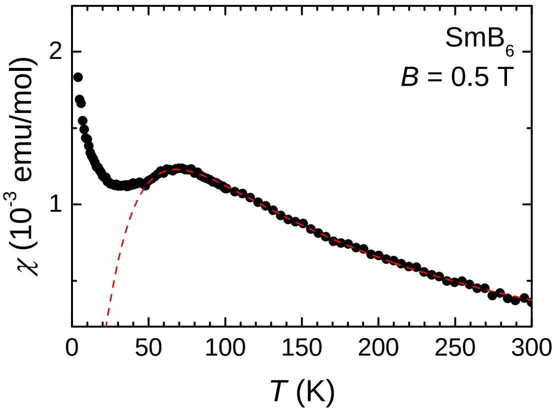

Fig. 4.3 The measured molar susceptibility of a floating zone-grown SmB$_6$ single crystal as a function of temperature with an applied magnetic field of 0.5 T shows an activation type dependence at higher temperatures. The dashed red line denotes the spin gap fit with a spin gap value of $\Delta = 6$ meV.

specific heat divided by temperature of SmB$_6$ shows an increase, yet another feature that has evaded explanation, although some similarities can be drawn with the specific heat of heavy fermion systems [64, 65], that also show an enhancement of the specific heat at low temperature, thought to be due to the increase of γ with decreasing temperature. Recent studies have extended the list of experimental results unexpected for an insulator: NMR has found a constant NMR relaxation rate divided by temperature [66], and terahertz spectroscopy has revealed sizeable bulk conductivity at higher frequencies [67], both indicative of bulk states within the charge gap.

Fig. 4.3 shows the temperature dependence of the molar susceptibility of a floating zone-grown SmB$_6$ single crystal. Fitting to the activation type dependence at higher temperatures we obtain a spin gap value of $\Delta = 6$ meV, which is comparable to the activation gap inferred from electrical transport measurements. The low-temperature behaviour is likely due to magnetic impurities, although intra-gap magnetic excitations were also suggested in the past [68]. The value of the low-temperature molar susceptibility, $\chi_m = 2 \cdot 10^{-3}$ emu/mol in cgs units (which coverts to a molar susceptibility in SI units of $\chi_m = 3 \cdot 10^{-8}$ m^3/mol), is comparable to the value found by other studies [48, 68]. It is worth noting here, that the Sommerfeld-Wilson ratio, a dimensionless quantity that is of order 1 for Fermi liquids, and even for most heavy fermions [69], comes out as $R_W \approx 200$ (using the susceptibility and linear specific heat coefficient values found above, and a Landé g-factor of 1), reinforcing the strong correlations that are at play in SmB_6.

The de Gennes relation, the scaling of the magnetic ordering temperature with the de Gennes factor (dG$= (g_J - 1)^2 J(J+1)$, where g_J is the Landé g-factor, and J is the total orbital angular momentum) is often a great utility to understand how the ground states evolve for entire families of compounds (i.e. $RENi_2B_2C$ [70] and $RE_3Pt_{23}Si_{11}$ [71] families). Whilst the relationship does not hold that accurately for the rare-earth hexaboride series, we still find their properties to be strongly influenced by the number of f-electrons, leading to an increasing magnetic ordering temperature with increasing moment. LaB_6 has no f-electrons, so no magnetic ordering, and a well-understood band structure [72], whereas CeB_6, PrB_6, and NdB_6 have antiferromagnetic metallic ground states with increasing transition temperatures. EuB_6 is a ferromagnetic semimetal, probably due to the rare-earth ions being divalent. In another Universe it would also be interesting to see what is the low-temperature ground state of PmB_6. Interestingly, CeB_6, which has the same J as SmB_6, shows an increasing resistivity with decreasing temperature above the transition temperature, with an inferred gap of ≈ 0.2 meV [73], but the RKKY interaction overcomes the Kondo interaction to induce a transition to antiferromagnetism below 2 K. The diverse properties exhibited by the rare-earth hexaborides underscore the many interactions that are at play, which in the case of SmB_6, the cuckoo's egg among the magnetically ordered hexaborides, combine to form a non-magnetic correlated insulator with all its anomalous properties.

4.3 De Haas–van Alphen oscillations in SmB_6

Our first report on the striking observation of de Haas–van Alphen oscillations in SmB_6 [10] kick-started the search for a description of a Fermi surface in the absence of a Fermi liquid, that is also supported by complimentary measurements. This motivated our subsequent study [29], which presented quantum oscillation measurements that reinforce the three-dimensional bulk character of the observed Fermi surface through the investigation of the angular dependence

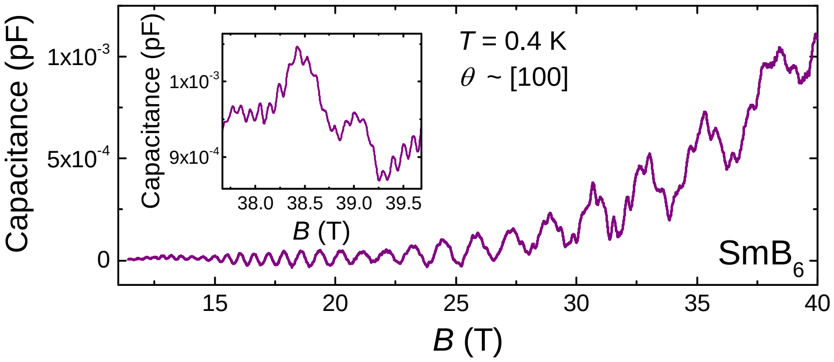

Fig. 4.4 The measured de Haas–van Alphen oscillations in a floating zone-grown SmB$_6$ single crystal using the capacitive torque technique. θ marks the direction of the applied magnetic field relative to crystallographic axes. We see several oscillation frequencies as big in amplitude as the paramagnetic background. The inset shows a zoomed-in view of the high field oscillations revealing fast oscillations corresponding to large Fermi surface sections.

and absolute amplitude of the oscillations, and presented measurements of the specific heat, oscillatory entropy and thermal conductivity with signatures in support of bulk low-energy excitations. In the next two sections we revisit our measurements performed on high-quality floating zone-grown single crystals, and present a comprehensive discussion of the measured quantum oscillations and thermodynamic signatures.

Fig. 4.4 shows an example of the measured quantum oscillations in the magnetic torque of a floating zone-grown single crystal of SmB$_6$ before any background subtraction. The oscillation pattern suggests the presence of multiple oscillation frequencies, with the inset of the figure showing evident rapid oscillations for the higher field ranges. The rapid oscillation frequencies, corresponding to large Fermi surface sections, and the large oscillation amplitude, as large as the paramagnetic torque background, are already evocative of some of the discussions to follow.

We plot the measured quantum oscillation frequencies for a floating zone-grown sample as a function of angle for field sweeps performed in the [001]-[111]-[110] rotation plane (Fig. 4.5a). We compare this to the quantum oscillation frequencies observed for metallic LaB$_6$ and PrB$_6$ (Fig. 4.5b and c [74]). We recognise frequency branches over the entire frequency range in the angular dependence of SmB$_6$, that also exist for the metallic hexaborides. Their Fermi surface

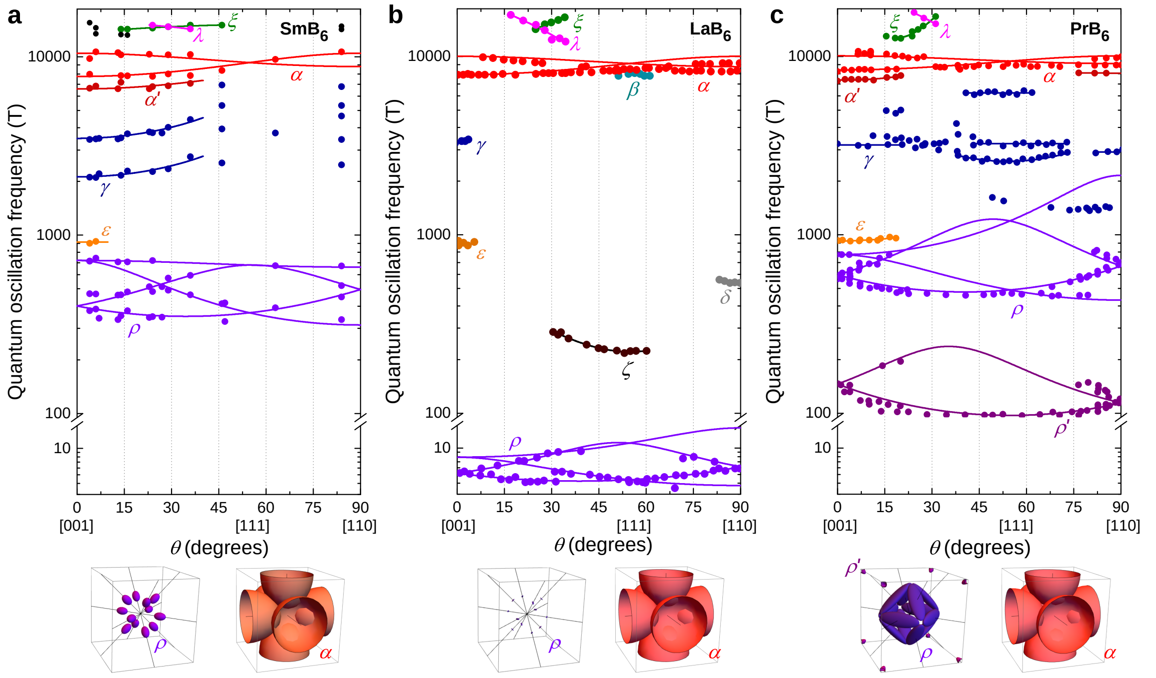

Fig. 4.5 The angular dependence of the quantum oscillation frequencies in the [001]-[111]-[110] rotation plane of floating zone-grown (a) SmB$_6$, (b) LaB$_6$ [74], and (c) PrB$_6$ [74]. We see very similar features in SmB$_6$ as were observed for the metallic hexaborides, and best described by a three-dimensional ellipsoidal Fermi surface model [75, 76]. The model describes three large prolate ellipsoidal electron pockets along the $\langle 100 \rangle$ directions, corresponding to the red frequencies marked as α, and twelve smaller ellipsoidal electron pockets along the $\langle 110 \rangle$ directions, acting as necks between the large α ellipsoids, corresponding to the purple frequencies marked as ρ. Fits with this model to the α and ρ frequencies are shown for each of the materials, with the resulting Fermi surface pockets shown in the images below.

is described by an ellipsoidal Fermi surface model [75, 76], that comprises of three large prolate ellipsoidal electron pockets along the $\langle 100 \rangle$ directions (shown in red in the Fermi surface images below the panels), and twelve smaller ellipsoidal electron pockets along the $\langle 110 \rangle$ directions, acting as connecting necks between the large α ellipsoids (shown in purple in the images below the panels). We find that this model can fully account for the angular dependence observed for SmB$_6$. We identify the frequencies shown in red as the large α ellipsoids, forming two frequency branches in the 8 to 11 kT frequency range spanning the entire angular range, and crossing at [111], this resembles the angular dependence of the metallic hexaborides. These large pockets constitute to more than 90% of the Fermi surface sections of the ellipsoidal

Compound	Sheet	$F_{\min}$ (T)	m^* (m_e)	ak_0 (nm^{-1})	b/a	c/a	γ
SmB_6	α	7750(90)	0.70(4)	4.85(3)	1	1.35(2)	3.0(5)
	ρ	314(14)	0.18(1)	2.15(9)	0.47(3)	0.44(3)	1.1(4)
LaB_6 [73, 77, 28]	α	7890	0.64	4.89(3)	1	1.27	2.6
	ρ	4	0.05	0.07	4.5	2.1	0.1
PrB_6 [73]	α	8400	1.95	5.05	1	1.2	7.8
	ρ	431	0.68	0.69	5	2.8	2.1
	ρ'	97	0.28	0.54	1	2.44	0.1

Table 4.1 A comparison of the parameters obtained from fitting to the measured angular dependence of the oscillation frequencies (Fig. 4.5) that are used to estimate the contribution of each Fermi surface sheet to the linear specific heat coefficient γ, a measure of the quasiparticle density of states and to be compared with the value obtained from the heat capacity. The parameters are the measured oscillation frequency corresponding to the smallest cross-section of the Fermi surface sheet F_{min}, the corresponding effective mass m^*, and the ratios of the semi-principal axes of the modeled ellipsoidal Fermi surface sheets denoted by a, b and c. γ has units of mJ·mol^{-1}·K^{-2}.

Fermi surface of metallic hexaborides. Interestingly, the Fermi energy contours imaged by ARPES, with large pockets centred at the X points, are quite reminiscent of the α pockets of the three-dimensional ellipsoidal Fermi surface model [78]. The frequencies corresponding to the small ρ ellipsoids are shown in purple, forming four branches. The angular dependence of the ρ pockets is the same across the three materials, whilst their size seem to vary due to subtle differences in the geometry of the α pockets. The angular dependence of the cross-section of an ellipsoid can be described by closed-form functions [29, 13], which we use to fit to the α and ρ frequencies of each material, with the resulting fits shown by the red and purple fit lines. Table 4.1 lists the different parameters obtained from the fits, including the eccentricities of the different ellipsoidal pockets. Other commonalities across the three materials include the ε and γ frequencies shown in orange and blue, which correspond to hole orbits enclosed by four touching α ellipsoids at special angles (centred at the Γ and M points respectively) [74], and the λ and ξ frequencies shown in dark green and magenta, crossing at the same angle for all three materials, corresponding to figure-eight orbits formed by two neighbouring α ellipsoids and reaching across two Brillouin zones [79].

In the case of PrB_6, we also identify a lower frequency branch marked as ρ'. Previous proposals for this frequency branch included the existence of two necks (ρ and ρ') [80], and splitting of the ρ pocket into an up-spin and down-spin pocket [74]. A similar splitting of the Fermi surface was expected for CeB_6, but has not been observed, and would also disagree with the measured specific heat coefficient [28]. We find that fitting to the ρ' frequencies assuming a second set of neck ellipsoids along the $\langle 110 \rangle$ directions does not work well, but instead find a good fit assuming small ellipsoids orientated along the $\langle 111 \rangle$ directions. Such pockets also appear in band structure calculations for PrB_6, which reside at the R points, the corners of the Brillouin zone [72]. We note that the lowest frequency oscillations of ≈ 50 T in SmB_6, that appear along certain angles [10, 81], but do not conclusively form a Fermi surface pocket, and therefore are not shown in the angular dependence figures, could correspond to tiny pockets residing in the corners of the Brillouin zone, similar to PrB_6.

It is important to consider the possibility of magnetic breakdown due to the high magnetic fields involved. There are different scenarios to consider. One theory paper proposed a magnetic breakthrough scenario through the Kondo gap [82] (similar to the proposal in Ref. [83]), that would lead to orbits enclosing areas similar to the Fermi surface areas found for the metallic hexaborides, and claim could be observable for the magnetic fields we employed. Another scenario is the magnetic breakdown between interconnecting sheets among the ellipsoids, similar to what was proposed initially for LaB_6 [75]. They reported the observation of frequencies they assigned to breakdown orbits from magnetic fields as low as 4.3 T (which we see down to $\approx$3.2 T in our Warwick-grown samples). In later reports [76, 74], however, these frequencies were recognised as orbits expected for the three-dimensional ellipsoidal Fermi surface model. If magnetic breakdown is possible at such low fields for the metallic hexaborides, then some of the observed SmB_6 frequencies could also be due to breakdown orbit. Importantly, they would not be very different from the frequencies we already observe, a majority of which are already assigned to correspond to sheets expected for the three-dimensional ellipsoidal Fermi surface model. What we can exclude with certainty is the third scenario, namely that all the high-frequency oscillations are caused by magnetic breakdown of the small ρ pockets. We use Blount's criterion [84] to estimate at what magnetic field magnetic breakdown effects would

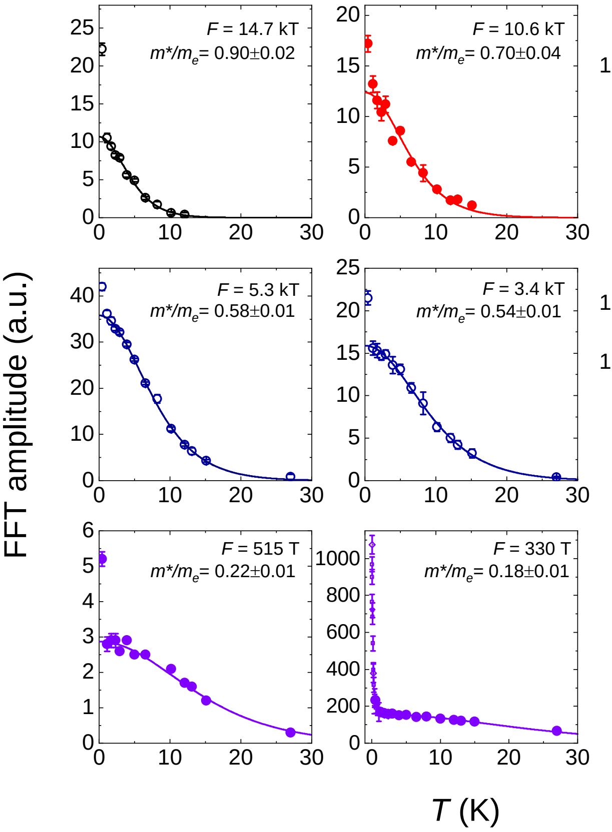

Fig. 4.6 The temperature dependence of the quantum oscillation amplitude of the measured frequencies in a floating zone-grown SmB$_6$ single crystal measured at an angle ≈[110]. The quantum oscillation amplitude values were obtained from Fourier transforms using a magnetic field window of 21 T to 40 T. We use the Lifshitz–Kosevich equation to fit the observed temperature dependences (shown as lines) to extract the effective mass m^* of each frequency for a temperature range of 1 K to 30 K. We see a divergence from the Lifshitz–Kosevich behaviour below 1 K for several frequencies, most clearly seen for the $F = 330$ T frequency.

become relevant:

$$H_{\mathrm{breakdown}} = \frac{\pi\hbar}{e}\left(\frac{k_g^3}{a+b}\right)^{1/2}$$

Here $1/a$ and $1/b$ are the radii of curvature of the two closest Fermi surface sections (neighbouring ρ ellipsoids) and k_g is their separation in reciprocal space. We have a separation of one quarter of the Brillouin zone between neighbouring ρ pockets, $k_g \approx 3.8$ nm^{-1}, and a

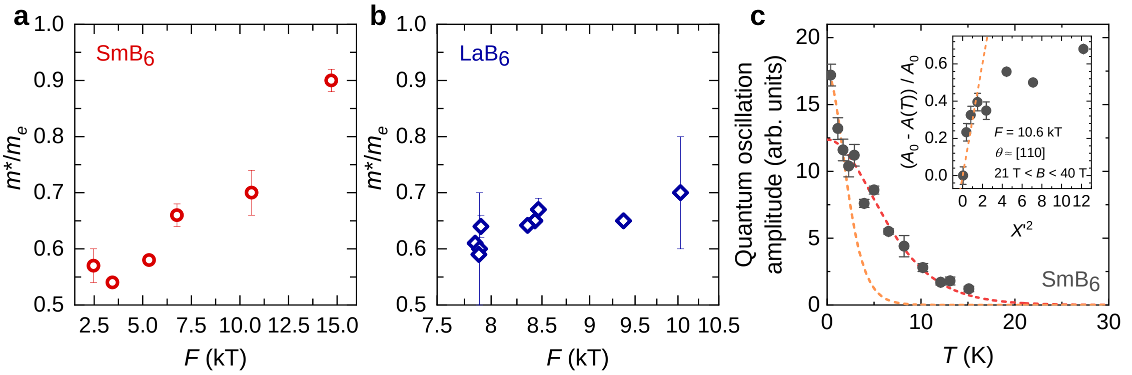

Fig. 4.7 Comparison of the effective masses as a function of quantum oscillation frequency (a) for SmB$_6$ measured along [110], and (b) for LaB$_6$ measured along different field directions based on Refs. [74, 73, 76, 77, 75, 85]. For both materials the effective mass scales with frequency down to 1 kT, as expected for Fermi surface pockets that originate from the same band. (c) The quantum oscillation amplitude of the 10.6 kT frequency as a function of temperature between 550 mK and 30 K, showing a prominent low-temperature upturn below 1 K. The dashed red line represents the Lifshitz–Kosevich fit to the temperature region with effective mass $m^*/m_\mathrm{e} = 0.7$ that fits the amplitude as a function of temperature for $T \gtrapprox 1$ K. For temperatures below 1 K a Lifshitz–Kosevich fit with effective mass $m^*/m_\mathrm{e} = 1.8$ was performed (orange dashed line). The inset shows the 10.6 kT frequency amplitude $A(T)$ with respect to A_0, the amplitude at the lowest measured temperature, as a function of X'^2, where $X' = 2\pi^2 k_\mathrm{B} T m_\mathrm{e}/e\hbar\mu_0 H_0$, the temperature damping coefficient in the Lifshitz–Kosevich formula, as expected for the Fermi Dirac statistical distribution [13]. The increase in amplitude at low temperatures is linear in X'^2 (shown by orange dashed line). A similar deviation from the Lifshitz-Kosevich temperature dependence is also observed for other frequencies, as reported in Refs. [10, 29] and shown in Fig. 4.6.

radius of curvature $1/a = 1/b \approx 1\ \mathrm{nm}^{-1}$, taken from Table 4.1. This gives a giant magnetic breakdown field of ≈ 10000 T, well above the magnetic fields where we observe high-frequency oscillations.

In Fig. 4.6 we plot the temperature dependence of the quantum oscillation amplitude for different oscillation frequencies of SmB$_6$. We perform Lifshitz–Kosevich fits to find their respective effective masses. For the lowest temperatures we also see a divergence from the Lifshitz–Kosevich behaviour for several frequencies. Above 1 K the Lifshitz–Kosevich fits yield effective masses between 0.2 and 0.9 electron masses, increasing with the size of the pocket. We plot this relationship for SmB$_6$ in Fig. 4.7a, and similarly for LaB$_6$ in Fig. 4.7b. For both materials we find a linear relationship between the measured effective mass and the oscillation frequency down to 1 kT, so all frequencies but the ones originating from the neck-like ρ pockets. The significance of the relationship $m^* \propto F$ is that all these frequencies must originate from the same band, as $\hbar^2 k^2/2m^* =$ constant. This has been established for LaB_6 before [73], the metallic hexaboride with the best-understood band structure, and the fact that it also applies to SmB_6 provides further support for the validity of the ellipsoidal Fermi surface model in its case.

4.4 Thermodynamic signatures of a Fermi surface in a band insulator

Based on the data presented so far we have found that SmB_6 behaves as a bulk insulator when an electric current is applied, but is host to quantum oscillations, a tell-tale signature of a metal, when we look at the magnetic torque. Starting with an Ansatz of quasiparticles, that give rise to magnetic quantum oscillations, but do not take part in charge transport, we are motivated to explore thermodynamic measurements, where such quasiparticles are expected to show up. The thermodynamic measurements presented in this section were performed by collaborators on the same samples or samples from the same batch of crystals as the ones employed in the magnetic torque measurements. Specific heat measurements were performed by the Takano group at the University of Florida, and the Yamashita group at Osaka University, and thermal conductivity measurements were performed by the Sutherland group at the University of Cambridge, and the Hill group at the University of Waterloo.

We first look at specific heat measurements. The finite linear specific heat, normally associated with free electrons, was one of the original curiosities about SmB_6 [43], and has remained a puzzle ever since. Measurements on our floating zone-grown single crystals also show a finite linear specific heat term, with a linear specific heat coefficient γ of $\approx 4(1)$ $\mathrm{mJ{\cdot}mol^{-1}{\cdot}K^{-2}}$ (Fig. 4.8a). Similarly to other rare-earth hexaborides, the phonon spectrum of SmB_6 is fairly complicated, and the high temperature part of the measured specific heat is not fitted well with just one phonon term. It likely requires both an Einstein term and a Debye term, as was shown for LaB_6 [89], but these terms do not contribute much below 10 K.

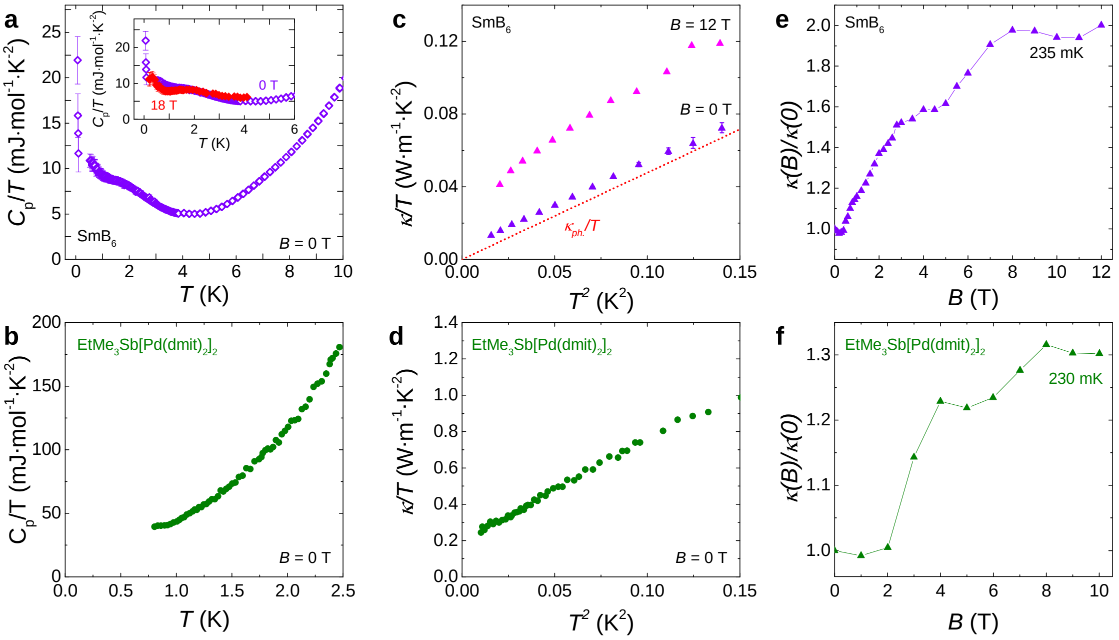

Fig. 4.8 (a) The measured specific heat C_p of a floating zone-grown SmB$_6$ single crystal at zero applied magnetic field, revealing a finite heat capacity divided by temperature at low temperatures, unexpected for an insulator, with a steep increase below 100 mK. The inset shows the specific heat divided by temperature at a magnetic field of 18 T. The linear contribution of the specific heat retains the same finite value at high magnetic fields. (b) The specific heat of an organic insulating spin liquid showing a similar finite linear specific heat coefficient at low temperatures [86]. (c) Thermal conductivity κ divided by temperature of a floating zone-grown SmB$_6$ single crystal at 0 T and 12 T. The phonon term $\kappa_{ph.}/T$ (red dotted line) accounts for most of the 0 T thermal conductivity, however a nearly fourfold enhancement of the thermal conductivity is seen at 12 T at the lowest measured temperatures. (d) Thermal conductivity κ divided by temperature of the same organic insulating spin liquid [87]. EtMe$_3$Sb[Pd(dmit)$_2$]$_2$ exhibits a finite linear thermal conductivity, which resembles the thermal conductivity of SmB$_6$ measured at 12 T. (e) The thermal conductivity as a function of magnetic field of SmB$_6$, showing a significant increase with magnetic field for the same floating zone-grown single crystal. (f) Very similar behaviour was observed for EtMe$_3$Sb[Pd(dmit)$_2$]$_2$ [87, 88].

We see a clear upturn at low temperatures that becomes even more dramatic below 100 mK. This might pertain to the anomalous temperature dependence of the quantum oscillations at similarly low temperatures [10, 29] (see also Fig. 4.7). The inset of Fig. 4.8a shows the specific heat measured in an applied magnetic field of 18 T overlaid on the zero field data. We find the overall behaviour unchanged with a similar upturn at low temperatures, and a finite specific heat with the coefficient γ comparable to the zero field value. This result is in accordance with a mostly field-independent charge gap as demonstrated by pulsed field electrical transport measurements [53].

The linear specific heat coefficient γ provides a measure of the quasiparticle density of states at the Fermi level, which in turn is set by the geometry of the Fermi surface. Hence, it allows for a quantitative comparison between a thermodynamic quantity and quantum oscillation measurements. We presented the relevant equations in Chapter 2, with the parameters of the Fermi surface geometry and the resulting estimate of γ for each Fermi surface sheet summarised in Table 4.1. Accounting for the three large α and the twelve smaller ρ ellipsoids, we get an estimate of $\approx 4.1(6)$ mJ·mol^{-1}·K^{-2}, which is in agreement with the estimate from the measured linear specific heat coefficient. A similarly good agreement has been demonstrated in the case of the metallic hexaborides LaB_6, with γ measured to be 2.6 mJ·mol^{-1}·K^{-2}, and the Fermi surface estimate being 2.7 mJ·mol^{-1}·K^{-2} (Table 4.1), and CeB_6, with γ measured to be 120 mJ·mol^{-1}·K^{-2} at 12.7 T [90], and the Fermi surface estimate being 113 mJ·mol^{-1}·K^{-2} [28]. This much higher value of γ is due to the very high effective masses of CeB_6. There are no low temperature specific heat data to compare with for PrB_6, but from quantum oscillation measurements we estimate γ to be ≈ 10 mJ·mol^{-1}·K^{-2}. The fact that the value of γ in SmB_6 remains unchanged upon the application of high magnetic fields (inset of Fig. 4.8a) suggests a field-independent character of the Fermi surface, in line with our findings (e.g. field-independent effective masses and no Fermi surface reconstruction with magnetic field).

Fig. 4.8c shows the thermal conductivity κ of a floating zone-grown SmB_6 single crystal at 0 T and 12 T. We plot the thermal conductivity κ divided by temperature as a function of the square of the temperature to highlight a clear T^3 dependence associated with phonons. We find that the phonon term $\kappa_{\mathrm{p}h.}/T$ (red dotted line, see Chapter 2 for formula, using sample dimensions of $t = 0.43$ mm, $w = 0.23$ mm, and a Debye temperature of $\theta_D = 373$ K) accounts for most of the 0 T thermal conductivity, leading us to conclude that the thermal conductivity in zero field is boundary-limited. Surprisingly, a nearly fourfold enhancement of the thermal conductivity is seen at 12 T at the lowest measured temperatures, which cannot be accounted for by phonons, and extrapolates to a finite linear term normally associated with heat-carrying

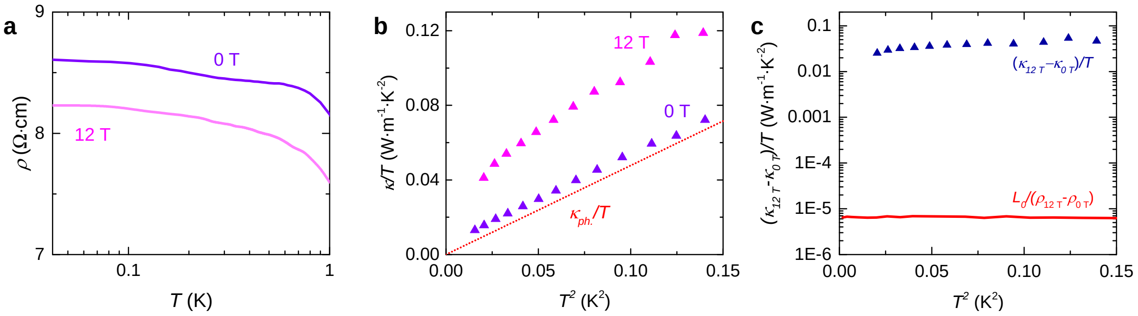

Fig. 4.9 (a) The electrical resistivity ρ as a function of temperature of a floating zone-grown single crystal measured at zero applied magnetic field (green) and 12 T (purple) below temperatures of 1 K, showing a small decrease in resistivity with applied magnetic field. (b) The thermal conductivity κ divided by temperature as a function of the square of the temperature of the same single crystal at 0 T and 12 T. Whilst the zero field data is mostly accounted for by the phonon contribution, we see a large enhancement of the thermal conductivity with applied magnetic field. (c) Comparison of the enhancement in the low-temperature thermal conductivity between 12 T and 0 T (blue triangles), with that expected from the enhancement in the surface electrical conductivity based on the Wiedemann–Franz law (red line). The enhancement in the low-temperature thermal conductivity is found to be almost four orders of magnitude larger, in clear violation of the Wiedemann–Franz law.

quasiparticles. This is contrary to the results presented in Ref. [91], where they found a non-boundary-limited phonon contribution in zero magnetic field, that becomes boundary-limited in a magnetic field, and a significantly smaller enhancement with field. Their observed behaviour is explained through some kind of a magnetic scattering process at zero field, that would get quenched in a magnetic field. However, our results show boundary-limited behaviour at 0 T, therefore any such magnetic scattering processes are absent from our samples, possibly due to their higher quality. We also note that no magnons have been observed by either muon spin resonance [92] or neutron scattering measurements [93]. In Fig. 4.8e we plot the measured thermal conductivity as a function of applied magnetic field, which reveals a large enhancement with field. Interestingly the overall behaviour of the measured specific heat and thermal conductivity of SmB_6 is very similar to that of the Mott insulating organic system $EtMe_3Sb[Pd(dmit)_2]_2$, which has been associated with novel spinon low-energy excitations [87, 88]. Whilst no quantum oscillations have been measured for this material, likely due to high scattering rates, evidence for neutral quasiparticles has been provided by the measured finite specific heat (shown in Fig. 4.8b), the finite linear temperature dependence of the thermal conductivity (Fig. 4.8d), and its enhancement with applied magnetic field (Fig. 4.8f). We note that the field enhancement of the thermal conductivity in SmB_6 is even more dramatic than in $EtMe_3Sb[Pd(dmit)_2]_2$.

Our thermal conductivity results are very much unexpected for an insulator, and encourage further measurements to help complete the picture. It would be interesting to see whether the relative orientation of the applied magnetic field and heat current would change the observed behaviour, and whether we could detect any anisotropy in the thermal conductivity of our samples, as suggested by Ref. [91]. It would also be interesting to see the effects of roughening the sample surface, and whether it would change the low temperature phonon behaviour. Another question is whether the field enhancement is sample dependent, or if it could also be observed for samples with shorter mean free path (a smaller phonon peak near 10 K). No field enhancement was observed for a flux-grown sample with an iRRR of 5000 [94].

The large field enhancement we observe in the thermal conductivity raises the question whether a similar change is manifested in the electrical resistivity, which is dominated by surface conduction at low temperatures. Here, however, we find a discrepancy between the electrical resistivity and the field enhanced thermal conductivity, in violation of the Wiedemann–Franz law. Whilst the change in resistivity upon the application of a large magnetic field is a small fraction of the total value (Fig. 4.9a), we see a large increase in the thermal conductivity (Fig. 4.9b). Applying the Wiedemann–Franz law, and multiplying the electrical conductivity by the Lorenz number we find that the enhancement of the electrical conductivity is four orders of magnitude smaller than what would be expected from the enhancement of the thermal conductivity divided by temperature.

Continuing with a picture of neutral quasiparticles that undergo Landau quantisation to produce quantum oscillations and also carry heat in thermal transport, a natural question becomes whether they are governed by the same scattering rate or mean free path. We estimate the mean free path from the damping term of the quantum oscillations, as derived in Chapter 2

$$l = \frac{\pi \hbar k_{\mathrm{F}}}{e B_0}$$

where $k_{\mathrm{F}} = \sqrt{2eF/\hbar} = 5.8 \cdot 10^9$ m^{-1} is the Fermi wave vector for the 11 kT frequency, and B_0 is the corresponding damping factor found to be ≈ 200 T for floating zone-grown samples, giving a mean free path of $l \approx 50$ nm in the magnetic field range 35 T $\leq B \leq$ 45 T. We compare this to the estimate of the mean free path from thermal conductivity based on the Sommerfeld model (see Chapter 2)

$$l = \frac{\kappa}{T} \frac{\hbar}{3k_{\mathrm{B}}^2 k_{\mathrm{F}}^2} \tag{4.1}$$

where k_{F} is the Fermi wave vector for the 11 kT frequency, and the linear coefficient of the thermal conductivity $\kappa/T = 0.04$ W·m^{-1}·K^{-2} at 12 T from Fig. 4.8c, giving a mean free path of $l \approx 2$ nm. An alternative estimate of the mean free path from thermal conductivity is based on a formula for a non-Fermi-liquid scenario with no well-defined quasiparticles [95]. It was also used by Ref. [96] to calculate the thermal conductivity of an organic system assuming a spinon Fermi surface with gapless excitations. For our floating zone-grown sample we have

$$l = \frac{\kappa}{T} \frac{\hbar k_{\mathrm{F}} a^3}{k_{\mathrm{B}}^2} \tag{4.2}$$

where k_{F} is the Fermi wave vector for the 11 kT frequency, and $\kappa/T = 0.04$ W·m^{-1}·K^{-2} at 12 T from Fig. 4.8c, giving a mean free path of $l \approx 9$ nm. Likely, the mean free path estimates from the thermal conductivity come out smaller due to the the lower magnetic fields at which the thermal conductivity was measured, but we still get results comparable within an order of magnitude. For comparison, the estimate for the mean free path based on the low temperature value of the electrical conductivity would be $\approx 10^{-6}$ nm. This is based on the Drude theory relating the electron mobility to the scattering rate, giving the formula

$$l = \sigma \frac{m^* v_F}{ne^2} \tag{4.3}$$

where the electrical conductivity σ is 0.8 S/m, $n = a_{\mathrm{u.c.}}^{-3}$, and the Fermi velocity v_F is given by $v_F = \hbar k_{\mathrm{F}}/m^*$, where k_{F} is the wavevector of the 11 kT oscillations, and m^* is the corresponding effective mass.

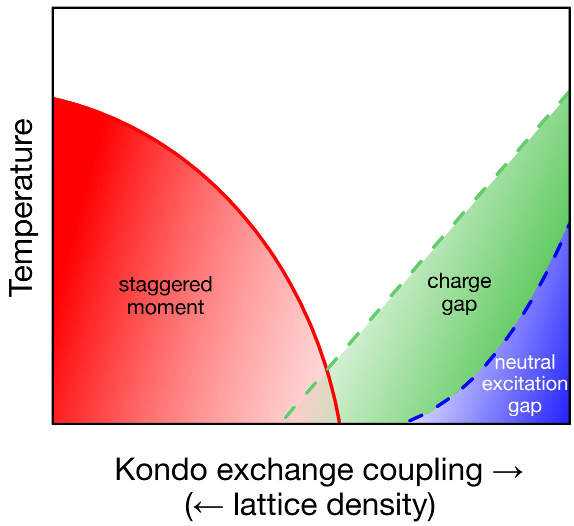

Fig. 4.10 Schematic phase diagram adapted from theoretical simulations [97], showing a region of the phase diagram with a finite charge gap but an already collapsed neutral excitation gap. We propose that SmB_6 is located at the edge of this region, with material differences between different samples that position them on either side of this boundary. The lattice density has been demonstrated to be a tuning parameter by applied pressure measurements [98–100], that can be used to collapse both gaps.

The observed thermodynamic signatures are very much contrary to the electrical properties of SmB_6, with a finite linear specific heat term, a field-enhanced thermal conductivity, a violation of the Wiedemann–Franz law, and an unexpectedly high mean free path, whereas quantitative comparison between thermodynamic and quantum oscillation measurements show several commonalities. This suggests that the same quasiparticles are responsible for the observed thermodynamic signatures and the quantum oscillations, but they do not take part in charge transport. The formation a theoretical model of such quasiparticles is made tricky by gauge invariance linking the Coulomb and Lorentz forces, but encouragingly, recent progress has been made by several theories on novel itinerant low-energy excitations that could give rise to quantum oscillations [101–105], invoking magnetic excitons [106], spinons [107–113], composite excitons [114] and Majorana fermions [115–119]. We note the sensitivity of some of the observed metallic signatures to the growth method [29]. We propose that the Kondo exchange coupling changes with the lattice density, and can tune SmB_6 from a Kondo insulator to a material that still retains a charge gap but is host to neutral low-energy excitations (Fig. 4.10).

4.5 Intrinsic character of bulk quantum oscillations in SmB_6

The observation of quantum oscillations in SmB_6 has lead to a flurry of investigations to establish a theoretical basis for the existence of a Fermi surface in a correlated insulator, something that has only been associated with metals before. Whilst most proposals centre around some form of novel itinerant low-energy excitations, a few proposals include disorder-induced in-gap state quantum oscillations [120], and proposals of quantum oscillations that originate from impurity inclusions [121, 122]. The variable sample quality across studies, partly due to different growth methods, has indeed caused difficulties when interpreting conflicting results. Disparity from the measured properties of stoichiometric SmB_6 has been demonstrated for samples with the presence of magnetic rare-earth impurities like Gd, Dy and Eu [57, 123–128], non-magnetic rare-earth impurities like La and Yb [57, 125–129], and metallic impurities like Al and C [41, 56, 121]. Particular care should be taken with the selection of flux-grown samples due to the use of extrinsic flux, that could lead to inclusions, which have been shown to yield associated quantum oscillations in other systems (e.g. UBe_{13} [130, 131], CaB_6 [132]). On the other hand, the floating zone growth technique is particularly effective in the case of materials with challenging phase diagrams such as incongruently melting compounds and compounds bounded by eutectic phase boundaries [133], like in the case of SmB_6. It is known to yield single crystals of excellent quality [48, 134], as their quality is determined by the purity of the starting samarium and boron powder, unlike other growth methods that can involve other starting elements, like aluminium-flux growth. Therefore, to be able to make the strongest case for the intrinsic nature of the quantum oscillations we observe, we limit the current section to measurements on single crystals grown by the floating zone technique only. We ascertain the extremely low impurity content that characterises our single crystals through a range of measurements used to evaluate sample quality of SmB_6 single crystals, and through direct comparisons with other studies. This section is based on our work presented in Ref. [135].

ppm Range	Elements
<limit of detection (100)	Al, As, Be, Bi, Ca, Cd, Co, Cr, Cu, Dy, Eu, Fe, Hf, Hg, Ho, Ir, K, La, Li, Lu, Mg, Mn, Mo, Na, Nb, , Ni, Os, Pb, Pt, Rb, Re, Ru, Sc, Si, Sn, Sr, Ti, Tm, V, Yb, Zn, Zr
<limit of detection (400)	Ag, Er, Ga, Nd, Se
100-1000	Te, Y
1000-10000	
10000 or >1%at	B, Sm

Table 4.2 The results of the inductively coupled plasma optical emission spectrometry (ICP-OES) on our pristine floating zone-grown SmB_6 single crystal showing the limits of the impurity concentration of different elements. ICP-OES was performed by Exeter Analytical UK Ltd., where ≈ 50 mg of single crystals were digested in a nitric acid matrix using microwaves and introduced to the spectrometer with internal standards to aid precision.

The first measurement we consider is inductively coupled plasma optical emission spectrometry (ICP-OES), which is an elemental analysis technique, where a single crystal needs to be fully decomposed to its constituent elements, and transformed into ions when introduced to the inductively coupled plasma. These ions can then be quantified with a mass spectrometer coupled to the instrument. This technique represents a direct way of performing elemental determination of the bulk volume of the sample. The results for one of our floating zone-grown single crystals is shown in Table 4.2, establishing that the concentration of all impurities are below the detection limit of the instrument (including aluminium and gadolinium inclusions), but tellurium and yttrium, which show a concentration above the detection limit, but still below 0.1%at.

We revisit our thermal conductivity measurements, and use them as a tool of comparison with samples from previous studies. We look at the high temperature phonon peak that appears in the regime where the mean free path goes from temperature-dependent (due to the decreasing number of phonons with decreasing temperature) to temperature-independent (instead determined by geometrical effects such as defects). This leads to a peak in thermal conductivity, with the peak height dependent on the low-temperature mean free path, and

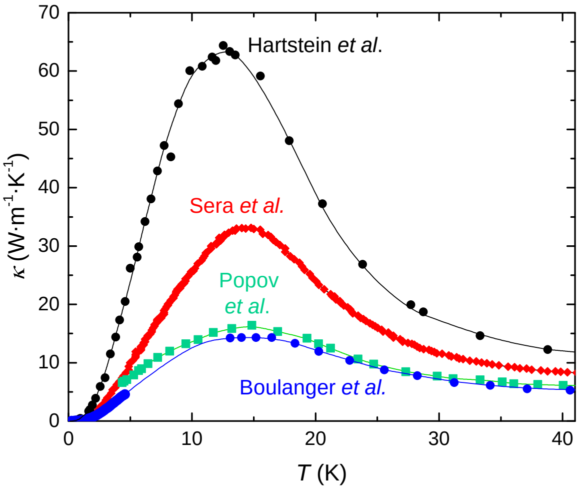

Fig. 4.11 The thermal conductivity κ as a function of temperature for a floating zone-grown SmB$_6$ single crystal grown by the Warwick group (black circles [48, 29]), compared to the thermal conductivity measured for floating zone-grown samples from previous studies (red diamonds [136], green squares [137], blue circles [91]). The size of the peak is found to be largest for the floating zone-grown crystal from the same batch of crystals as the ones employed in our quantum oscillation measurements, indicating high sample quality.

therefore acts as a gauge for sample quality. Fig. 4.11 compares the phonon peak observed for our floating zone-grown sample to that of samples from other studies [91, 136, 137]. We find the peak height of our single crystal to be several times larger than of other samples, confirming that it has the longest mean free path. Interestingly, the smallest peak is observed for the flux-grown sample from the study that argued for the non-boundary limited character of the thermal conductivity in zero applied magnetic field [91]. We find that to characterise the true underlying low-temperature state via the thermal conductivity, one requires the highest quality samples, that in turn demonstrate clear boundary-limited behaviour at low temperatures [29]. Results on EtMe$_3$Sb[Pd(dmit)$_2$]$_2$ lend credence to this [138], finding that only high-quality samples with longer mean free paths show a finite residual linear term in the thermal conductivity, attributed to itinerant gapless excitations.

Ref. [123] presents a study of SmB$_6$ samples with variable impurity content, and quantifies the relationship between magnetic impurities and observed material properties. We repeat the measurements on our pristine floating zone-grown single crystals to determine their sample quality in relation to the samples presented in Ref. [123] and elsewhere. We quantify the

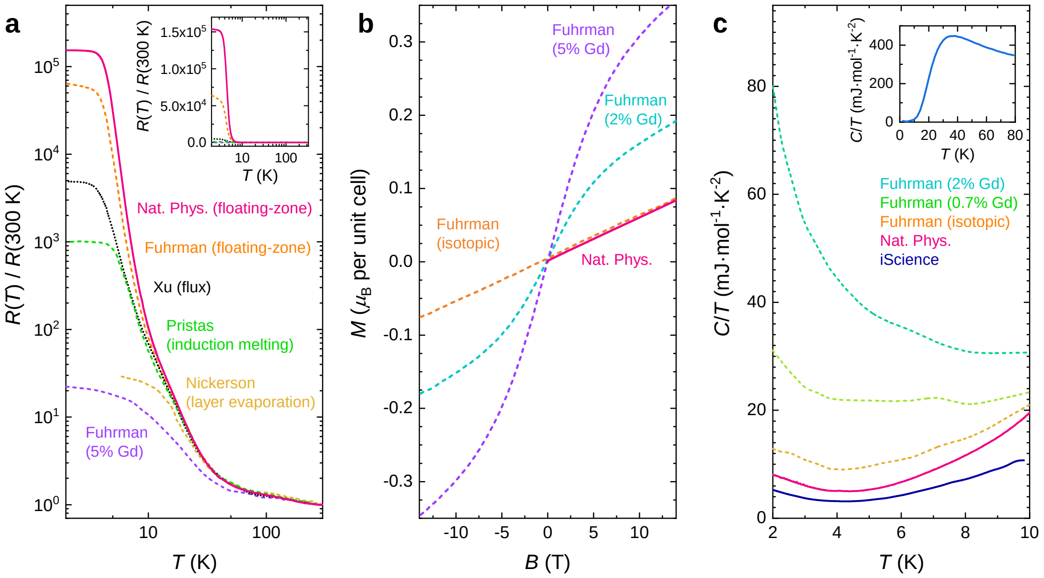

Fig. 4.12 (a) Measured electrical resistivity as a function of temperature normalised to 300 K. The inverse residual resistivity ratio of our samples reach a value of the order 10^5, higher than the isotopic floating zone-grown sample with minimal rare-earth impurities from Ref. [123], and samples grown by other growth methods (flux-grown [94], induction melting [139], layer evaporation [43]). The inset shows the resistivity on a linear scale. (b) Measured magnetisation of Gd-doped SmB$_6$ samples from Ref. [123] (dashed lines in purple and cyan), showing a non-linear magnetisation due to magnetic impurities. In contrast, the measured magnetisation of undoped floating zone-grown single crystals (magenta line, grown by the Warwick group [48, 29], orange dashed line, isotopic sample from Ref. [123]) show a linear paramagnetic behaviour as expected for impurity-free SmB$_6$. We estimate the magnetic impurity concentration of our sample by fitting with the Langevin function [123], finding it to be 0.04%at. (c) Measured specific heat capacity of SmB$_6$ for our floating zone-grown single crystals (blue [135] and magenta lines [48, 29]), an isotopic floating zone-grown sample (orange dashed line [123]) and flux-grown Gd-doped samples (green and cyan dashed lines [123]). The lowest finite heat capacity divided by temperature is observed for our floating zone-grown sample, which reaches a minimum of 3 mJ·mol^{-1}·K^{-2}, comparable to the value found for isotopically enriched SmB$_6$ [125, 134]. The inset shows the specific heat capacity up to 80 K of a single crystal of SmB$_6$ from the same growth batch as the one studied in Ref. [29].

magnetic impurity content of our samples by performing low-temperature magnetisation measurements as a function of magnetic field (Fig. 4.12b). For an impurity-free sample we expect a linear paramagnetic response. For any magnetic impurities this would be distorted according to the Langevin function [140]. Hence, fitting with this function provides a way to estimate the magnetic impurity concentration. For our sample (pink line) we see a linear response with a deviation from linearity consistent with a magnetic impurity concentration level of less than 0.05%, which is comparable to what was observed for the highest quality isotopic sample in Ref. [123] (orange dashed line). Off-stoichiometric samples have also shown an increase in the linear specific heat coefficient γ, with values of 8 mJ·mol^{-1}·K^{-2} and higher, whereas the lowest value is realised for isotopically enriched samples that have the lowest concentration of impurities and vacancies as identified by other measurement techniques [123, 126]. In Fig. 4.12c we plot the measured specific heat of our samples as a function of temperature against those presented in Ref. [123]. The γ values we find for our floating zone-grown single crystals are very low at $\approx$ 3 mJ·mol^{-1}·K^{-2} for one sample (blue line) and $\approx$ 4 mJ·mol^{-1}·K^{-2} for a second sample (orange line), suggesting a minimal vacancy content and putting them in their own class with the isotopically enriched sample of Ref. [126]. For a fourth test of sample quality of SmB_6 samples, we look at electrical resistivity. Fig. 4.12a shows the electrical resistivity as a function of temperature for one of our floating zone-grown single crystals compared to the electrical resistivity measured for the isotopic floating zone-grown sample from Ref. [123], and for samples grown by other growth methods or with magnetic impurities [43, 94, 123, 139]. The inverse residual resistivity ratio of our sample is 150000, whilst the isotopic sample from Ref. [123] reaches a value of 60000. The two floating zone-grown samples show iRRRs higher than for all other growth methods, indicating a high insulating bulk contribution at low temperatures, and the absence of any metallic inclusions that would act to reduce the maximum resistivity reached. Thus, we have found that our floating zone-grown single crystals satisfy or outperform quality checks employed by previous studies [41, 91, 94, 123], establishing their extremely low impurity content. As anticipated for floating zone-grown single crystals, we confirm that there are no measurable traces of magnetic or metallic impurities present, making comparisons with studies on samples with embedded impurities [41, 56, 121] ill-suited.

Whilst the material quality checks we have presented decidedly rule out the presence of any aluminium in our samples to within 0.01%at, we wish to go further with our discussion and present an exhaustive analysis of the observed quantum oscillations to preclude any suggestions that the observed quantum oscillations in our floating zone-grown single crystals could be caused by aluminium [121]. For this we performed magnetic torque measurements employing the same experimental technique on floating zone-grown SmB_6, LaB_6 and aluminium.

We examine the amplitude of the measured quantum oscillations to confirm their bulk nature in SmB_6 and LaB_6, and present a comparison of the complete angular dependences of the three materials to highlight the dissimilarities between SmB_6 and aluminium, and in turn reinforce the similarities between SmB_6 and LaB_6. Fig. 4.13 shows the observed quantum oscillations using the capacitive torque technique in the three materials, with corresponding Fourier transforms showing the frequency spectra. For SmB_6 the strongest frequency at low fields is 500 T, with faster frequencies, which are associated with larger Dingle temperatures, appearing with increasing field. The highest frequency is 15 kT, which appears above 30 T. We find a similar overall behaviour of the quantum oscillations for LaB_6 (Fig. 4.13d-f), a broad range of oscillation frequencies, with the high frequencies of 8 kT and 10 kT appearing at lower fields due to a lower Dingle temperature as compared to SmB_6. In contrast, the measured quantum oscillations of aluminium (Fig. 4.13g-i) are dominated by oscillation frequencies less than 1 kT. We also observe a rich harmonic content, which leads to square-wave shaped oscillations at higher magnetic fields, as opposed to SmB_6, which exhibits sinusoidal oscillations up to 40 T.

Our measurements of the magnetic torque in SmB_6 reveal oscillations with amplitudes comparable to the size of the paramagnetic torque background (Fig. 4.4), which indicates a bulk origin for the oscillations, as opposed to an origin from just a minute fraction of the sample [9]. We provide further evidence for this observation by comparing the absolute size of the measured quantum oscillations and the theoretical amplitude of bulk de Haas–van Alphen oscillations. We convert the measured capacitive torque to absolute units of magnetic moment by using the spring constant of the cantilever as detailed in Ref. [29]. We have cantilever length $L = 3.8$ mm, distance between cantilever and fixed Cu plate $d_0 = 0.1$ mm, spring constant $k = 30\ \mathrm{N \cdot m^{-1}}$, unit cell volume $V_{\mathrm{u.c.}} = a^3_{\mathrm{u.c.}} = 0.07\ \mathrm{nm}^3$, and crystal volume $s^3 = 0.49\ \mathrm{mm}^3$. We thus convert the measured torque magnetisation in terms of capacitance (C) to an absolute

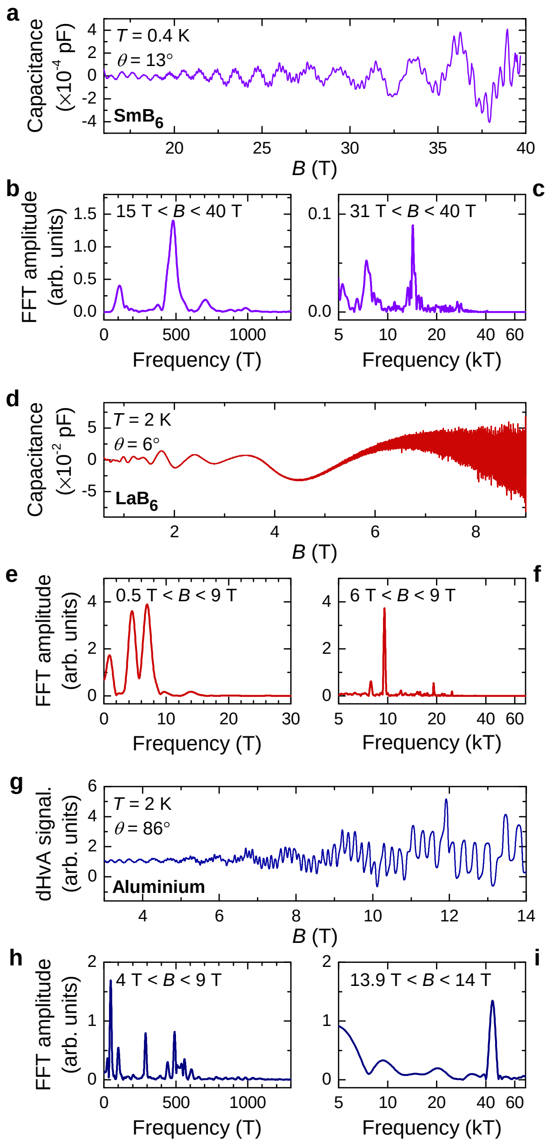

Fig. 4.13 (a) Measured oscillations in the magnetic torque of SmB$_6$ as a function of magnetic field for a floating zone-grown crystal. (b-c) Fourier transforms of the measured magnetic torque as a function of inverse magnetic field, revealing a multitude of quantum oscillation frequencies ranging from 300 T to 15 kT. A higher magnetic field window is used to reveal the high-frequency oscillations corresponding to the α, λ and ξ branches identified in Fig. 4.5a. (d) Measured oscillations in the magnetic torque of LaB$_6$ as a function of magnetic field exhibiting both low- and high-frequency oscillations similar to SmB$_6$. (e-f) Fourier transforms of the measured magnetic torque as a function of inverse magnetic field, revealing multiple quantum oscillation frequencies up to 10 T corresponding to the ρ branches, and between 8 and 10 kT corresponding to the α branches (see Fig. 4.5b). (g) Measured oscillations in the magnetic torque of aluminium as a function of magnetic field. (h-i) Fourier transforms of the measured magnetic torque as a function of inverse magnetic field, revealing multiple frequency peaks up to 500 T, and a very high-frequency peak of 40 kT, when taking a narrow field window, corresponding to the ψ branch (see Fig. 4.16c)).

magnetic moment p_s in units of Bohr magnetons per unit cell by the expression

$$\Delta p_s[\mathrm{3D}] = 0.175\ \mathrm{TpF}^{-1}\,\frac{\Delta C}{B}\quad \mu_\mathrm{B}\ \text{per unit cell.} \tag{4.4}$$

The measured quantum oscillatory magnetic moment converted to absolute units for a typical magnetic field sweep is shown in Fig. 4.14b. We estimate the theoretical amplitude of the intrinsic quantum oscillatory magnetic moment perpendicular to the applied magnetic field in units of Bohr magnetons per unit cell for a three-dimensional Fermi surface using the Lifshitz–Kosevich formula as detailed in Chapter 2

$$p_s[\mathrm{3D}] = D_\mathrm{3D}\cdot R_\mathrm{T}R_\mathrm{D}R_\mathrm{S}\cdot\sin(2\pi F/B+\phi)\cdot\sin\theta_M \tag{4.5}$$

where $\sin(2\pi F/B+\phi)$ is the oscillatory term, θ_M is the angle between the magnetic field B and the total magnetic moment, and R_T, R_D, and R_S are damping terms due to finite temperature, impurity scattering, and spin-splitting. The exponential damping term R_D is expressed as $R_\mathrm{D} = \exp(-B_0/B)$, with damping factor B_0 for each frequency. D_3D is the infinite field, zero spin-splitting amplitude given by

$$D_\mathrm{3D} = f(r)\frac{8m_e}{m^*}\left(\frac{k_\mathrm{F}}{k_\mathrm{BZ}}\right)^3\sqrt{\frac{B}{8F}} \tag{4.6}$$

where $f(r)$ is the anisotropy term, m^* is the effective mass, k_F is the Fermi wavevector, $k_\mathrm{BZ} = 2\pi/a_{\mathrm{u}.c.}$, and F is the oscillation frequency. For the $F = 452$ T frequency oscillations shown in Fig. 4.14a, we have $m^* = 0.18m_e$, $B_0 = 60$ T, a degeneracy of two and $f(r) = 0.5$ based on the ellipsoidal model we fit with in Fig. 4.5a, and we estimate $R_\mathrm{S} = 0.5$-1, $\sin\theta_M = 0.1$-1. The resulting estimate for the theoretical amplitude is $\approx 10^{-3}$–10^{-2} $\mu_\mathrm{B}\cdot$ T per unit cell at $B = 30$ T, whilst the measured amplitude is $\approx 10^{-3}$ $\mu_\mathrm{B}\cdot$ T per unit cell, showing consistency between the theoretical estimate and the measured size of the oscillations assuming a bulk origin.

Crucially, for an origin of quantum oscillations from impurity inclusions we would expect the measured amplitude of the oscillations to be much smaller than the theoretical estimate.

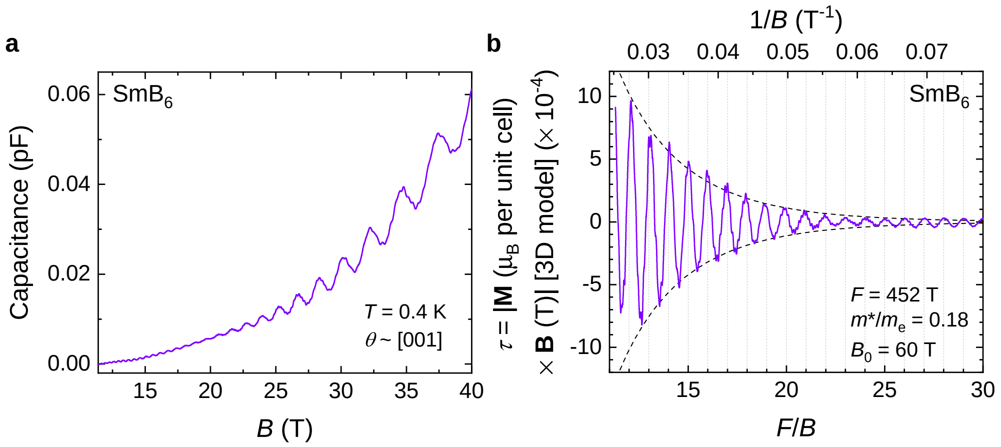

Fig. 4.14 (a) Measured quantum oscillations in the magnetic torque of SmB$_6$ as a function of magnetic field for a floating zone-grown crystal. The amplitude of the oscillations is comparable to the paramagnetic torque background, before any background subtraction. (b) De Haas–van Alphen oscillations in absolute units of magnetic moment corresponding to the $F = 452$ T oscillations. The dashed lines represent the magnetic field dependence of the quantum oscillation amplitude from the impurity scattering (Dingle) damping term for a damping factor B_0 of 60 T.

ICP measurements determined the concentration of aluminium impurities to be less than 10^{-4}, and therefore we would expect a discrepancy by at least four orders of magnitude, which we do not see. Similarly, a comparison with a two-dimensional Fermi surface model yields a measured value that is at least four orders of magnitude larger than the two-dimensional theoretical estimate as given by the formula (see Chapter 2)

$$p_s[2\mathrm{D}] = D_{2\mathrm{D}} \cdot R_{\mathrm{T}} R_{\mathrm{D}} R_{\mathrm{S}} \cdot \sin(2\pi F/B + \phi) \cdot \sin\theta_M \tag{4.7}$$

with

$$D_{2\mathrm{D}} = \frac{4m_e}{m^*}\left(\frac{k_{\mathrm{F}}}{k_{\mathrm{BZ}}}\right)^2 \tag{4.8}$$

The peak amplitude of the quantum oscillations is found to have a theoretical maximum value of $\approx 10^{-1}$ μ_{B} per surface unit cell in the infinite field limit prior to including any damping terms, which would reduce the theoretically predicted value to $\approx 10^{-3}$ μ_{B} per surface unit cell at 30 T. In contrast, we estimate the magnetic moment per surface unit cell for the measured quantum oscillations were they to arise from the surface, by multiplying by the ratio of the total number of unit cells to the number of unit cells on the surface, which is $\approx 10^6$. The measured amplitude of the quantum oscillations therefore corresponds to a magnetic moment per surface unit cell of $\approx 10^3$ $\mu_{\mathrm{B}}\cdot$ T per surface unit cell at 30 T, at least four orders of magnitude larger than the two-dimensional theoretical estimate. This rules out the scenario of oscillations originating from surface states. The same comparison for the high frequencies is hindered by the imprecise estimate of a much higher damping factor due to only accessing high Landau levels, and would require much higher magnetic fields. We find similarly large bulk oscillations for LaB$_6$ in correspondence with the Lifshitz–Kosevich theory [29], as expected for a metal.

We take a second look at the angular dependence of floating zone-grown SmB$_6$. This time we plot it on a linear frequency scale that highlights any differences in frequency when comparing similar frequency branches, and we also show a magnified view of the ρ branches to compare to that of LaB$_6$, and the branches with comparable frequencies observed for aluminium. We focus on the [001]-[111]-[110] rotation plane to avoid the overlap of higher ρ branches with harmonics that are present more densely in the [110]-[001] rotation plane. Earlier, we have discussed the similarities with the observed angular dependence for LaB$_6$, including the existence of the α branches in both materials that correspond to the main Fermi surface sheets, and the ε, λ, and ξ branches that only appear for the same specific angular ranges (seen again clearly for both materials in Fig. 4.15). It was these similarities with the metallic hexaborides that led us to conclude that the angular dependence of SmB$_6$ is best described by the same three-dimensional ellipsoidal Fermi surface model [10, 29]. We note the difference in the size and eccentricities of the ρ pockets, but these have been shown above to be highly variable across the hexaborides, very much dependent on the geometry of the main α ellipsoids, that constitute over 90% of the Fermi surface.

In contrast, comparison with the angular dependence of aluminium (Fig. 4.16) highlights many differences. The most prominent oscillations in our magnetic torque measurements of aluminium (Fig. 4.13g) correspond to the γ branches, originating from necklace-like Fermi surface sheets [142]. These elongated sheets lead to rapidly increasing frequencies as a function of angle, that diverge along the [111] and [001] directions, in direct contrast with the ρ frequencies found in SmB$_6$ that show a moderate angular dependence. The higher frequency

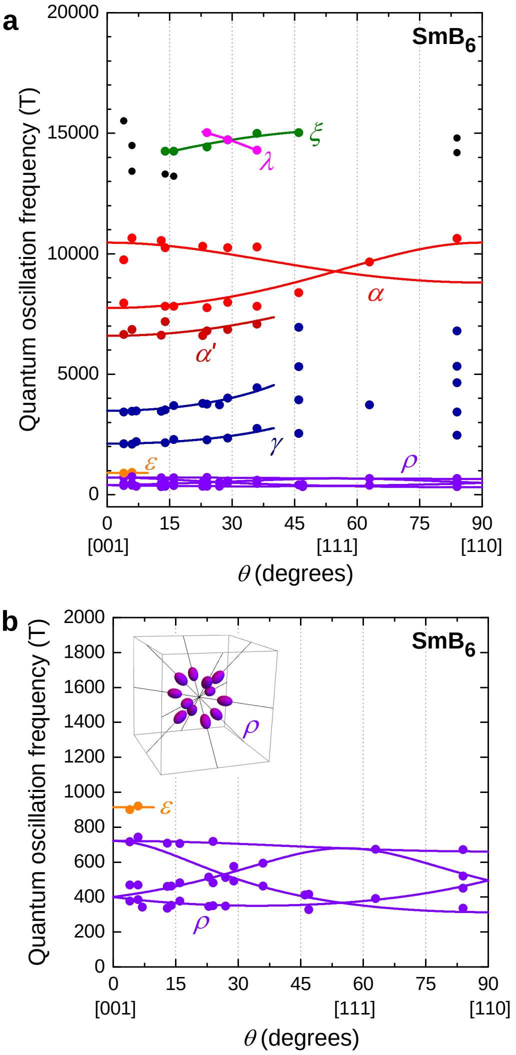

Fig. 4.15 Angular dependence of the quantum oscillation frequencies in the [001]-[111]-[110] rotation plane measured for (a-b) floating zone-grown SmB_6, and (c-d) LaB_6 [76, 74], both in good agreement with the angular dependence of a three-dimensional ellipsoidal Fermi surface characteristic of metallic hexaborides. (a) and (c) show the similarity of the higher frequency branches, particularly the main α branches, whilst (b) and (d) compare the lower frequency ρ branches, together with an illustration of the corresponding Fermi surface pockets.

range (2 kT to 15 kT), above the γ aluminium frequencies, is populated by many branches that span the entire angular range in the case of SmB_6, but there are no comparable frequency branches in aluminium. To find the second main frequency branch for aluminium, we have to consider an even higher frequency range (40 kT to 100 kT), corresponding to a large second-

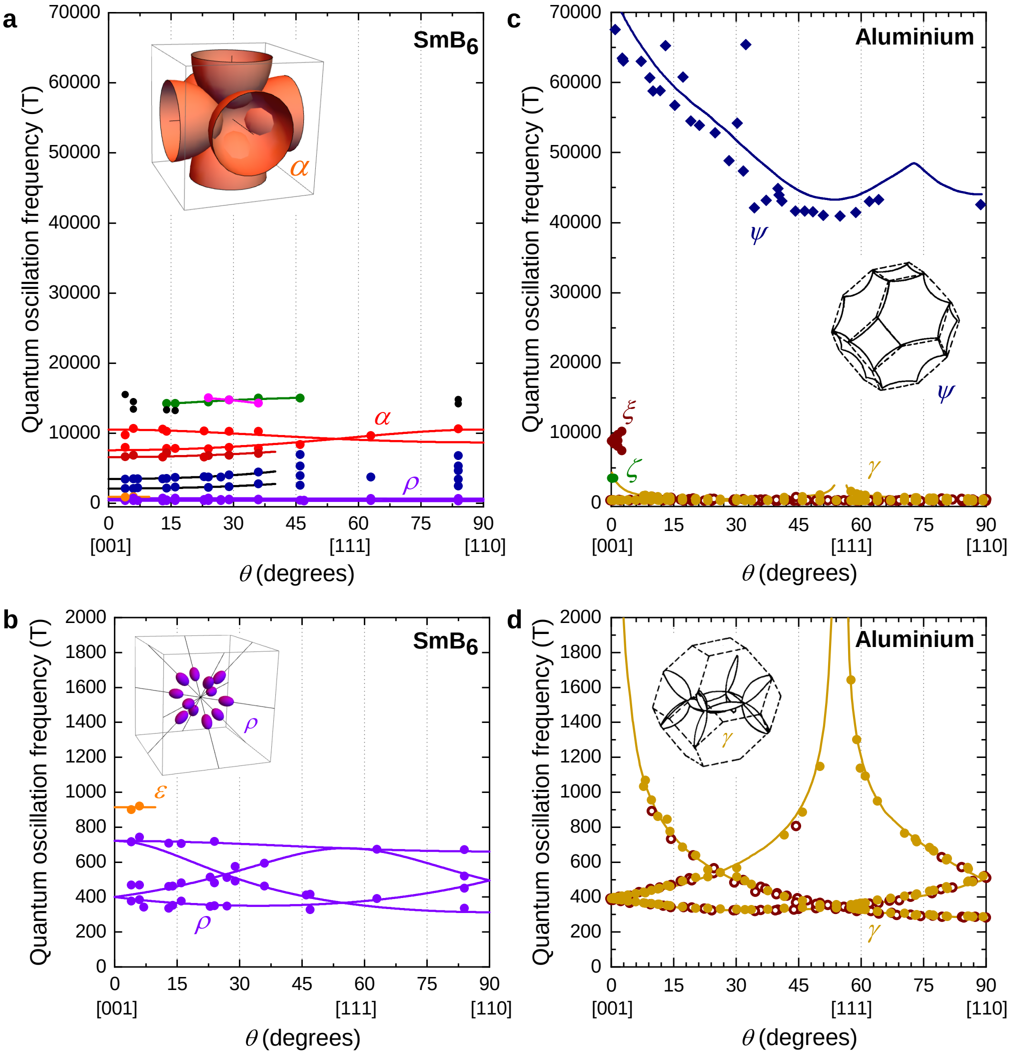

Fig. 4.16 Comparison of the measured angular dependence of the quantum oscillation frequencies in the [001]-[111]-[110] rotation plane of (a-b) floating zone-grown SmB$_6$, and (c-d) aluminium. The comparison of the high-frequency branches in (a) and (c) shows a multitude of branches between 2 kT and 15 kT spanning the entire angular range for SmB$_6$, but none for aluminium, which has a prominent high-frequency branch above 40 kT (circles are measured by this study, diamonds are from Ref. [141]). (b) ρ branches found for SmB$_6$ have a moderate angular dependence corresponding to a Fermi surface of twelve ellipsoids along <110>, as shown in the illustration. (d) The γ branches found in this study for aluminium show a diverging behaviour, consistent with previous measurements (show by brown circles) [142, 143], with frequencies as high as 1600 T, corresponding to a necklace-like Fermi surface of elongated arms as shown in the illustration (taken from Ref. [144]). Solid lines follow Ashcroft's model [144] and are from Ref. [142].

zone Fermi surface, that in turn has no parallels in SmB_6. We note the similar frequencies in the $300-400$ T range for the two materials. This coincidence could be a consequence of Luttinger's theorem, as SmB_6 and aluminium both have the same number of valence electrons, and cubic unit cells with comparable lattice constants ($a = 4.13$ Å for SmB_6, and $a = 4.05$ Å for aluminium). With these differences in mind, future measurements of SmB_6 should focus on measuring the [001]-[111]-[110] rotation plane (unlike the studies in Refs. [121, 145] that measured the other rotation plane), and collecting a complete data set to identify the flat angular dependence in the case of the four branches of the ρ frequencies, and doing a rigorous search for the high-frequency branches ($6-15$ kT) using slow magnetic field sweeps at the highest attainable fields, the experimental manifestations of the three-dimensional ellipsoidal Fermi surface.

Lower quality samples with measurable impurities have prompted studies that provide extrinsic explanations [121, 122], but here we have reinforced the commonality of the Fermi surface sections between SmB_6 and metallic hexaborides, and presented material studies of our floating zone-grown samples that clearly reflect the properties of SmB_6 without contributions from Al. Therefore, we conclude that any quantum oscillations observed in floating zone-grown SmB_6 have to be intrinsic and cannot be explained to originate from aluminium.

4.6 Theoretical proposals for a Fermi surface in an insulator

The weight of evidence challenges the classical understanding of quantum oscillations being exclusive to Fermi liquids, and requires new theoretical ideas that could explain the paradigm of a Fermi surface associated with a non-Fermi liquid. The chief experimental signatures to be addressed by a comprehensive theoretical model for SmB_6 include the exclusive observation of quantum oscillations in magnetic torque, but not in resistivity, and the manifestly periodic oscillations in inverse magnetic field, indicative of a Fermi surface, the finite value of the specific heat divided by temperature, and the finite value of the thermal conductivity divided by temperature in a magnetic field. Whilst a complete review of the many theoretical proposals [82, 83, 101–122, 146–161] is outside the scope of this work, we briefly discuss how these experimental signatures are addressed by some of the emerging theoretical frameworks. The studies under review almost universally predict periodic in inverse magnetic field oscillations with a few exceptions. Ref. [162] lacks an explanation of the observed oscillations, whilst two other studies predict unusual field dependences − Ref. [110] finds that the spinons from the spinon Fermi surface are coupled to an internal orbital magnetic field, and Ref. [83] finds the quantum oscillation frequency varying with the gap size, which are difficult to consolidate with our results. Contrary to our observations, some studies also predict large Shubnikov–de Haas (SdH) oscillations in resistivity [9, 94, 146, 148], whilst some predict Shubnikov–de Haas oscillations, but find that they might be too small to be measurable [120, 153, 158]. SmB_6 seems to differ from YbB_{12} in this case, where for the latter the observed resistivity oscillations [12] could be explained by the proximity of a metal-insulator transition around a magnetic field of 48 T [163], whereas for SmB_6 resistivity oscillations have not been observed, and the charge gap remains open up to at least 90 T [53]. The advantage of theories of neutral quasiparticles is that they provide a natural answer to the absence of Shubnikov–de Haas oscillations [101–119, 123]. More recent theories also address the observed metal-like specific heat and thermal transport results [106, 114, 117–119, 149, 159, 161], however estimates of the Fermi surface and the effective masses have been less concrete. On the other hand, theories that invoke a non-neutral Fermi surface have made more headway in this direction. They make the explicit prediction that the observed quantum oscillation frequencies are set by the unhybridised Fermi surface, akin to the Fermi surface of metallic hexaborides [82, 120, 146, 147, 155, 159, 158]. Finally, as new theoretical proposals struggle to address all the metal-like properties of SmB_6, another avenue could be that of Ref. [159] that proposes SmB_6 to be a failed metal with a few insulating properties at low temperatures, rather than an insulator with many metallic properties.

4.7 Conclusions

We have presented recent progress on Kondo insulating SmB_6, revealing a multitude of experimental signatures that are unexpected for an insulator including bulk quantum oscillations in magnetic torque, a sizeable linear specific heat coefficient, and the enhancement of the thermal conductivity in an applied magnetic field. Together, these experimental signatures are demonstrative of a Fermi surface unexpected for a bulk insulator. Whilst both extrinsic and intrinsic explanations have been brought forward, here we have reinforced that an intrinsic explanation must be sought as demonstrated by the central points of this work. As theoretical frameworks that could explain the entire suite of experimental signatures are still emerging, an obvious question is if there are other non-Fermi liquid systems that are host to a Fermi surface. Other Kondo insulators are obvious candidates, and motivated our work on a closely related Kondo insulator, YbB_{12}, which is the topic of the next chapter.

Chapter 5

Quantum oscillations in Kondo insulating YbB_{12}

5.1 Introduction

With the discovery of a Fermi surface in Kondo insulating SmB_6 and the pursuit to establish a theoretical framework behind it, the search for other insulators that are host to a Fermi surface became just as pertinent. YbB_{12}, another rare-earth boride Kondo insulator with many commonalities with SmB_6, became one of the earliest candidates, and soon was confirmed to show quantum oscillations in its insulating state [11]. In this chapter we will present our measurements of YbB_{12}, the first observation of quantum oscillations in this material, and discuss whether the multitude of shared material properties with SmB_6 also extend to a common Fermi surface origin.

In the same year as the discovery of an unusual insulating state at low temperatures in SmB_6 [3], there were early reports of YbB_{12} also showing a dramatic increase in resistivity with decreasing temperature, but conclusive results were hindered by the presence of YbB_6 phases in these crystals [164]. Early studies on single phase YbB_{12} were limited to polycrystalline samples [165–167], with the first floating zone-grown, and therefore high-quality single crystals of YbB_{12}, reported much later [168].

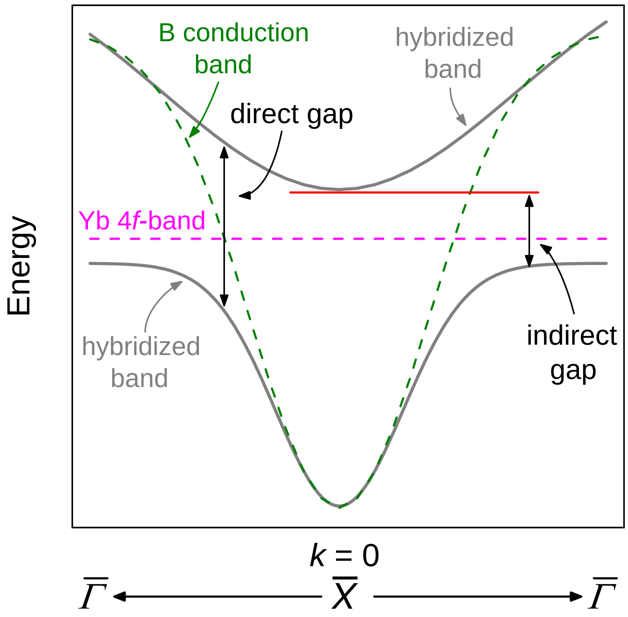

Fig. 5.1 Schematic picture of the band structure of the Kondo insulator YbB$_{12}$ showing the hybridisation that develops at low temperatures, leading to a Kondo gap between the boron conduction and ytterbium *f*-electron bands.

The main commonalities between the two Kondo systems include a cubic crystal structure with a boron cage around the rare-earth atoms [166], an activated resistivity behaviour at low temperatures typical of Kondo insulators [168], comparable activation gap sizes in the meV range [166], and finite linear heat capacity otherwise associated with metals [169]. Whilst both systems are referred to as f-electron Kondo insulators, in the case of SmB$_6$ the hybridisation happens between the $5d$ and $4f$ samarium electrons, and in the case of YbB$_{12}$ it is boron conduction bands hybridising with $4f$ ytterbium electrons (Fig. 5.1). Just as importantly, the Sm ion in SmB$_6$ is considered mixed-valent with a valence of +2.6 [50], whereas the Yb ion in YbB$_{12}$ is +2.9 [168, 170, 171], which still qualifies it as mixed-valent, but one might expect it to lead to more similarities with its metallic rare-earth dodecaboride neighbours, like LuB$_{12}$ and TmB$_{12}$, than with SmB$_6$.

The low-temperature resistivity plateau, persisting in all literature on SmB$_6$, has made the material a curious case for decades, eventually motivating proposals of the existence of topological surface states [44]. The resistivity plateau, however, proved to be less universal for samples of YbB$_{12}$, and was absent in all samples until very recently [12]. As experimental indications for surface states in SmB_6 emerged [45, 46, 57, 78, 172], with the most compelling signatures shown by transport properties [45, 46, 57], YbB_{12} entered the conversation as another potential candidate for a topological Kondo insulator [173] due to its similar properties. Whilst a breadth of 2D-like transport signatures have been identified in the case of SmB_6, providing a roadmap of fundamental checks for other candidate materials, no such reports have appeared for YbB_{12}. Experimental reports of 2D-like states have been limited to one ARPES study, but with limited energy resolution [174]. With the discovery of a Fermi surface in the insulating state of SmB_6, YbB_{12} was soon identified as another candidate material, with quantum oscillations measured soon after by our group [11], followed by further studies by a second group [12, 175]. This development was made possible by the availability of high-quality single crystals, sensitive measurement techniques at high magnetic fields, and the aspiration for such measurements after the SmB_6 results.

5.2 Key properties of YbB_{12}

We studied single crystals of YbB_{12} grown by the Warwick group using the floating zone-growth technique. Resistivity measurements are again the first port of call for sample characterisation. The samples used for our measurements had an inverse residual resistivity ratio (iRRR) of ≈ 500 [11] (Fig. 5.2a). The best sample in the literature has an iRRR of 100000 [12], which is from the first batch of samples to also show a low-temperature plateau. Comparing resistivity values, our samples are similarly metallic at room temperature, but do not reach as high resistivity values in the Kondo insulating state. Interestingly, studying the same high iRRR samples, Ref. [175] finds comparable iRRR divided by sample thickness (iRRR$/t$) values (≈ 250) for their best samples, whereas their sample from a different growth batch, which shows much weaker quantum oscillations, has an iRRR$/t$ half that value, suggesting that iRRR$/t$ could also be a relevant measure of sample quality in the case of YbB_{12}, similar to SmB_6 (see Chapter 4). Fitting to the resistivity, we find an activation gap of ≈ 5 meV for our samples [11]. This is comparable to the energy gap derived from the specific heat (70 K, equivalent to 6 meV) [176], whilst photoemission found a 10 meV direct, and 100 meV

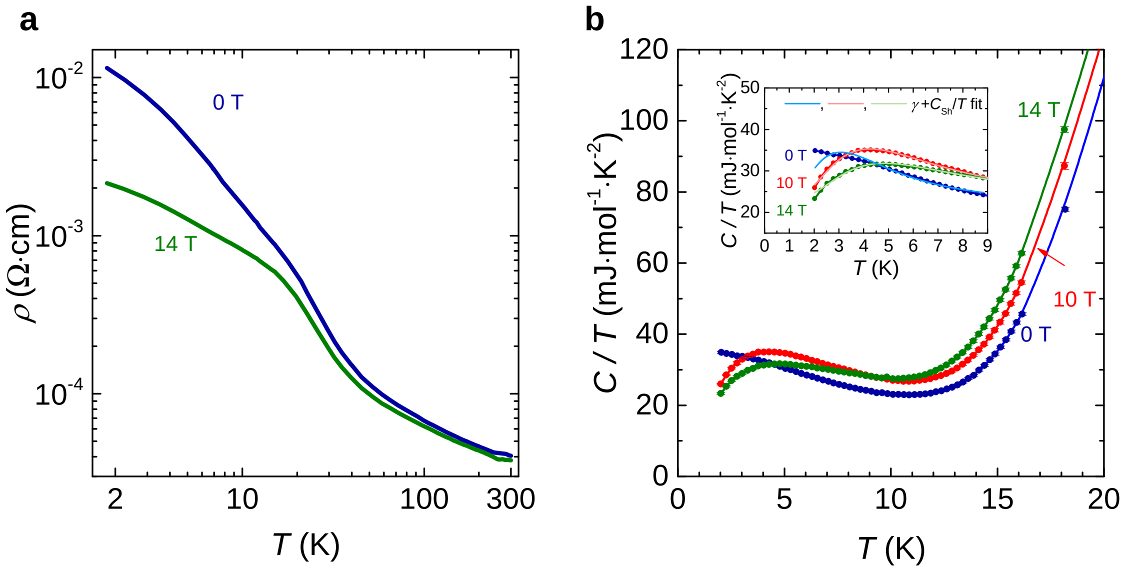

Fig. 5.2 (a) Resistivity as a function of temperature of a floating zone-grown YbB$_{12}$ sample in a magnetic field of 0 T (blue curve) and 14 T (green curve). The hybridisation-induced insulating behaviour is evident from the exponential increase in resistivity upon lowering of the temperature. The activation gap is found to be $\Delta \approx 5$ meV at 0 T [11]. (b) The measured specific heat of YbB$_{12}$ at different magnetic fields, revealing a finite specific heat divided by temperature, similar to what has been observed for SmB$_6$ [10, 29, 134, 178], normally associated with the contribution from electronic states. The inset shows the low temperature tail of the specific heat capacity divided by temperature, with the lines in light colours corresponding to fits based on an electronic and a Schottky specific heat term.

indirect gap [177]. In addition to resistivity, further sample screening was carried out by using a Laue diffractometer to screen out any samples that are not of a singular domain, and by susceptibility measurements to screen out samples with magnetic impurities, that lead to a non-linear magnetisation response with applied magnetic field at low temperatures.

We find a suppression of the resistivity with magnetic field at low temperatures (Fig. 5.2a), in stark contrast to SmB$_6$. Applying pulsed magnetic fields, Ref. [179] found a total suppression of the charge gap in YbB$_{12}$ with an insulator-metal transition at 46 T for a field direction along [001], and a transition at 55 T along [111] and [110]. Recent electrical transport measurements in pulsed magnetic fields [12] saw the resistivity drop by four orders of magnitude from its zero magnetic field value to a value of 0.3 mΩ·cm above 45 T, which is comparable to the zero-field resistivity at around 40 K, slightly below the characteristic temperature set by the gap size from resistivity and heat capacity measurements.

Fig. 5.2b shows the measured specific heat divided by temperature as a function of temperature in zero magnetic field and magnetic fields up to 14 T. At zero field a finite specific heat divided by temperature is revealed, unexpected for an insulator, and very similar to SmB_6 (Fig. 4.2). It was demonstrated in Chapter 4 in the case of SmB_6 that the value of the finite specific heat divided by temperature γ is sample dependent, with the lowest value realised in the highest quality samples. It is unclear if a similar variance in γ with sample quality also applies to YbB_{12}. We find that the local minimum of the specific heat divided by temperature C/T at $T \approx 10$ K to be slightly enhanced with magnetic field, potentially indicating a suppression of insulating behaviour with magnetic field. At the same time the low temperature upturn in zero magnetic field gets suppressed with increasing field, suggesting a magnetic impurity origin. We fit to the low temperature tail of the specific heat by assuming a finite specific heat divided by temperature contribution γ and a two-level Schottky contribution $C_{\mathrm{S}c}/T$. The inset to Fig. 5.2b shows the resulting fits with the peak of the Schottky anomaly pushed higher in temperature with increasing magnetic field, corresponding to an increase in the Schottky energy gap from a value of 10 K at 0 T to 23 K at 14 T. We find a γ of 22 mJ$\cdot$mol$^{-1}\cdot$K^{-2} at 0 T, increasing to 23 mJ$\cdot$mol$^{-1}\cdot$K^{-2} at 14 T. This is comparable to the value found by Ref. [169], but larger than the $\gamma = 4$ mJ$\cdot$mol$^{-1}\cdot$K^{-2} found for the samples exhibiting a low-temperature resistivity plateau [175]. The latter study is limited to magnetic fields of 12 T and lower, so it is possible that the linear specific heat coefficient might reach a higher value in the overlapping region between quantum oscillations and the insulating state. Indeed, a strong magnetic field dependence is expected based on Ref. [163], which found a dramatic increase in γ with magnetic field, going from 5 mJ$\cdot$mol$^{-1}\cdot$K^{-2} at 0 T to reaching a value of 60 mJ$\cdot$mol$^{-1}\cdot$K^{-2} at 49 T.

5.3 Quantum oscillations in the magnetic torque of YbB_{12}

The compendium of shared physical properties, together with a few particular differences between the two materials, made for an interesting case as to whether quantum oscillations

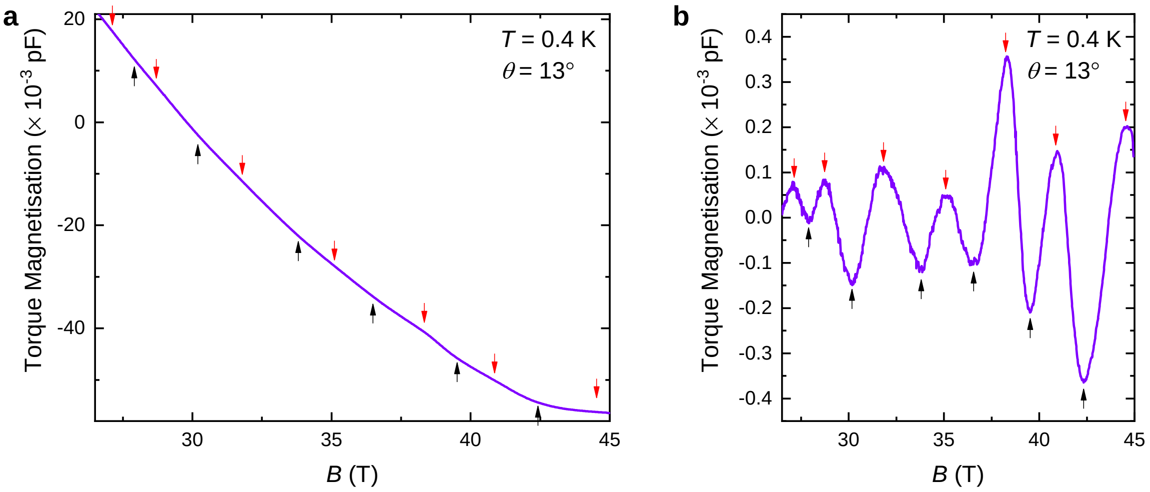

Fig. 5.3 (a) Measured magnetic torque of a YbB$_{12}$ crystal with the magnetic field applied 13° away from the [001] crystal direction in the [001]-[111]-[110] rotation plane, showing a non-polynomial background torque due to the proximity of the insulator-metal transition, with de Haas–van Alphen oscillations superimposed (each oscillation peak is marked by arrows). (b) The de Haas–van Alphen oscillations after subtracting out the background, revealing clear oscillations down to 26 T.

could also be observed in YbB$_{12}$. We carried out torque magnetometry measurements on floating zone-grown single crystals in DC high magnetic fields as described in Chapter 3. We find de Haas–van Alphen oscillations superimposed on a large torque background (Fig. 5.3a), that becomes non-polynomial towards higher fields due to the proximity of the insulator-metal transition. After subtraction we see a clear oscillation pattern down to lower fields (Fig. 5.3b). Fourier transform reveals two main frequency peaks of ≈ 300 T and ≈ 700 T (Fig. 5.4a). Plotting the temperature dependence of the amplitude of the oscillations and fitting with the Lifshitz–Kosevich equation yields an effective mass of $m^*/m_e = 3(1)$ for the lower frequency, and $m^*/m_e = 7(2)$ for the higher frequency (Fig. 5.4b). Such heavy effective masses are unexpected for YbB$_{12}$, as both SmB$_6$ [10, 29], the closest Kondo insulator analogue, and LuB$_{12}$ [11, 180, 181], a metallic dodecaboride, have large Fermi surfaces with light effective masses, and instead suggests the existence of a heavy Fermi surface consisting of small pockets.

Based on our measurements [11] and those of Ref. [12] the onset field of the oscillations appears to be angle dependent, with sizable oscillations visible from as low in magnetic field

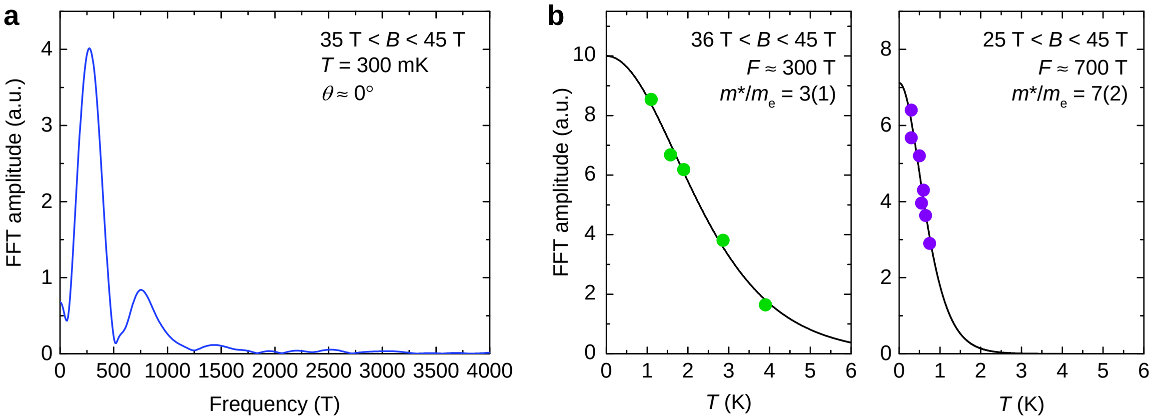

Fig. 5.4 (a) The Fourier transform of the measured magnetic torque near the [001] direction for a magnetic field window of 35 T and 45 T, revealing two oscillation frequencies at 300 T and 700 T. (b) The Lifshitz–Kosevich plot corresponding to each oscillation frequency, revealing heavy effective masses for both frequencies. The lines represent fits with the Lifshitz–Kosevich model.

as 37 T near the [001] direction, but pushed higher in field with increasing angle, with no oscillations visible below 45 T for angles past $\theta = 60^\circ$ (in the [001]-[111]-[110] rotation plane). Whilst we have identified two main oscillation frequencies, we are not able to construct an angular dependence plot, as we are limited in magnetic field at higher angles. The angular dependence of the onset field of the oscillations appears to be tracking the insulator-metal transition as a function of angle [179], but preceding it by $\approx$ 10 T, revealing a region in the phase diagram where quantum oscillations and the Kondo charge gap both prevail.

We next turn to the absolute amplitude of the oscillations. Due to the precise descriptive power of the Lifshitz–Kosevich equation, comparison of the measured amplitude of the torque oscillations to its theoretical value can give important insight into the origin of the oscillations (see similar discussion for SmB$_6$ in Chapter 4). Fig. 5.5 shows the magnetic torque in absolute units of μ_B per unit cell as a function of inverse magnetic field for YbB$_{12}$. The dashed envelopes represent the best fit for the exponential damping term due to impurity scattering ($R_D = \exp(-B_0/B)$). Based on Chapter 2, we estimate the theoretical amplitude of the intrinsic quantum oscillatory magnetic moment, taking into account the angular anisotropy term, Dingle and spin-splitting damping factors, taken to be between $1 - 4 \times 10^{-4}$ μ_B per unit cell at

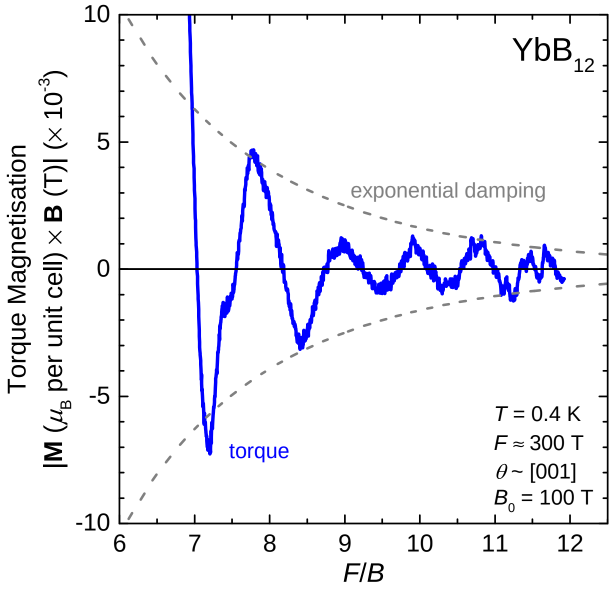

Fig. 5.5 The magnetic torque in absolute units of μ_B per unit cell as a function of inverse magnetic field for YbB$_{12}$. The dashed lines are the envelope of the quantum oscillations from the exponential damping due to impurity scattering ($R_D = \exp(-B_0/B)$), for a damping factor B_0 of $\approx$ 100 T. We find good order of magnitude agreement with the theoretical value predicted by the Lifshitz–Kosevich equation.

$F/B = 6.9$ ($B = 43.5$ T) for YbB$_{12}$. These values are in good order of magnitude agreement with the measured amplitude in Fig. 5.5, indicating that the oscillations observed arise from the bulk volume of the sample, rather than from impurity domains, or from surface states, both of which could only correspond to tiny volume fractions of the sample, and therefore would lead to orders of magnitude disagreement between theory and measurement. We note a marked increase in amplitude in this figure when approaching the insulator-metal transition. This again suggests an insulating bulk origin for the observed oscillations, rather than impurities or surface states, as such an enhancement due to the bulk becoming metallic would not be expected for an already conductive channel in the material. The case for two-dimensional surface states in YbB$_{12}$ is made even weaker by the lack of electrical transport evidence for such states, and in the case of our samples the lack of a low temperature plateau in resistivity.

Since our publication on de Haas–van Alphen oscillations in YbB$_{12}$ [11], Ref. [12] has reported Shubnikov–de Haas oscillations below the insulator-metal transition in the resistivity of YbB_{12}. From theoretical considerations, Shubnikov–de Haas oscillations should have higher sensitivity to potential conductive surface states than torque magnetisation measurements. However, the Shubnikov–de Haas oscillations in Ref. [12] are associated with the bulk insulating state on the basis of the flat angular dependence of the oscillation frequency, whereas the de Haas–van Alphen oscillations are associated with surface states based on limited angular dependence data. The report does not provide any further arguments why the bulk-sensitive torque magnetisation measurements would pick up oscillations from surface states, whereas transport measurements sensitive to conductive surface states pick up bulk oscillations, and the distinction appears to be only made to address the discrepancy between the oscillation frequencies identified by the two measurement techniques. Likely, further measurements are needed, which could consolidate whether the techniques see the same Fermi surface or two different ones.

5.4 A Fermi surface mirroring a heavy semimetal

We explore the origin of the unique heavy Fermi surface in YbB_{12} and contrast it with the light conduction electron Fermi surfaces found for Kondo insulating SmB_6 [29, 34] and the metallic dodecaboride analogue of YbB_{12}, LuB_{12} [11, 180, 181]. The application of band structure calculations to obtain the full picture for strongly correlated systems is often tricky, but can still give valuable intuition about the system.

Early band structure calculations struggled to capture the most crucial properties of YbB_{12} (either finding no band gap [182], or no mixed valency [183]). Techniques that are more suited for semiconductors and insulators, and usually give more accurate band gap values, have fared much better. Ref. [173] using the Gutzwiller approximation arrived at a valence of +2.9, and Ref. [11] (the calculation we will discuss presently), using the modified Becke-Johnson potential, finds a valence of +2.8 (Fig. 5.7a), close to experimentally observed values [168, 170, 171]. These band structure calculations reproduce the Kondo gap originating from the hybridisation between flat ytterbium f-bands and boron conduction bands. But how could there be a Fermi surface when there is no quasiparticle weight at the Fermi level?

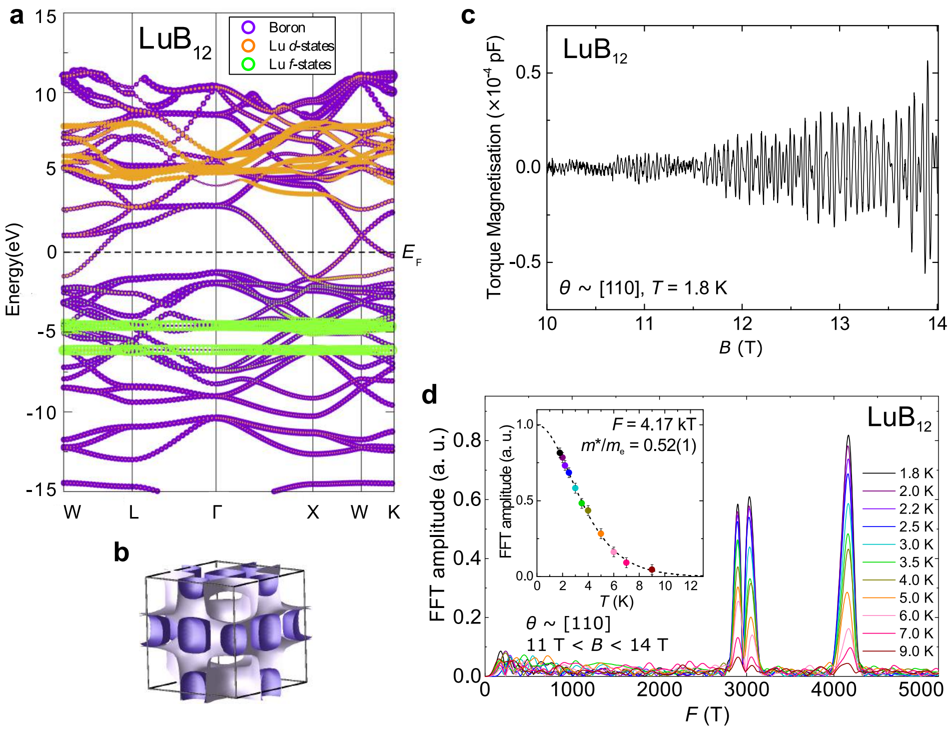

Fig. 5.6 (a) Band structure calculation of metallic LuB$_{12}$ from -15 eV to 15 eV. Green bands refer to the lutetium f-electron bands, orange bands are lutetium d-electron bands, while boron bands are in purple. (b) The Fermi surface sheets of LuB$_{12}$. (c) Magnetic torque measured at 1.8 K in LuB$_{12}$ along the [110] symmetry direction with quantum oscillations originating from several frequencies. (d) The temperature dependence of the quantum oscillation frequency Fourier peaks. The inset shows the size of the peak of the main 4.2 kT frequency as a function of temperature. Using a Lifshitz–Kosevich fit (dashed line in inset) we find the effective masses m^*/m_e to be 0.4, 0.5, and 0.5 for the frequencies 2.9 kT, 3.0 kT, and 4.2 kT, comparable to the expectation from band structure calculations. Such large frequencies and the corresponding light effective masses are unlike those found in YbB$_{12}$. Adapted from Ref. [11], with band structure calculations performed by Michelle D. Johannes.

For SmB$_6$, the important clue was the identification of a large Fermi surface of light masses, similar to the conduction electron Fermi surface of metallic hexaborides, particularly LaB$_6$ and PrB$_6$ [10]. This suggests a scenario where the hybridisation ceases, and allows quasiparticles to reside in the decoupled conduction bands. We explore whether a similar inference could be reached from the measured Fermi surface of YbB$_{12}$, by comparing it to the conduction Fermi surface of metallic dodecaborides, in this case LuB$_{12}$. Band structure calculation for LuB$_{12}$ shown in Fig. 5.6a reveals light boron bands crossing the Fermi level, with the lutetium d-bands and f-bands located well away from the Fermi level, in agreement

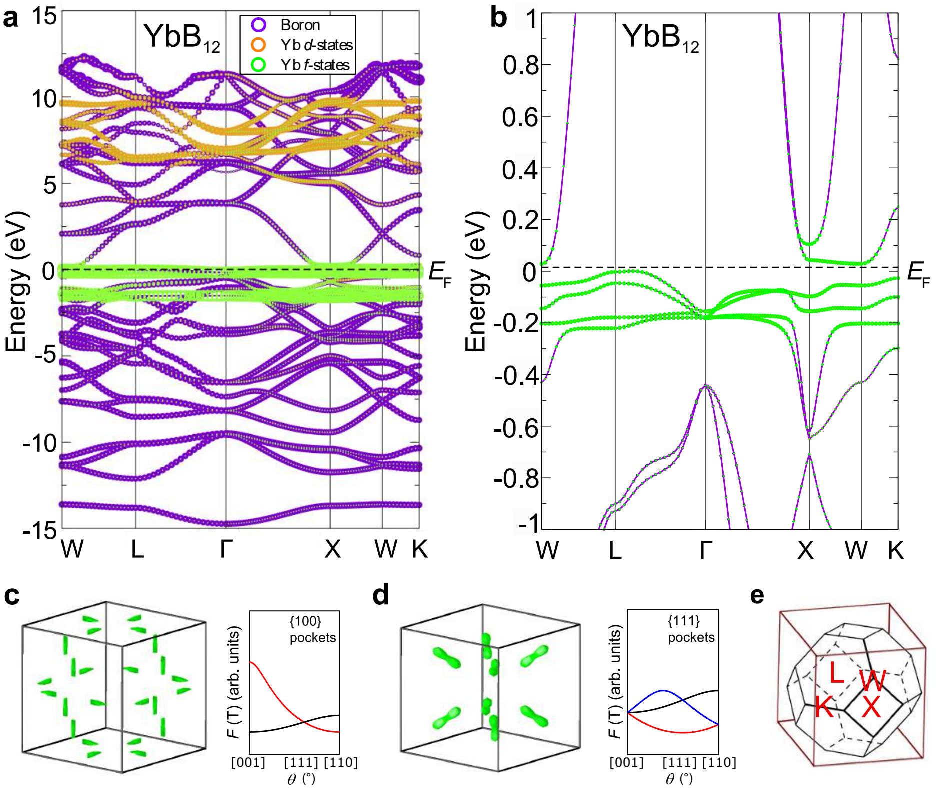

Fig. 5.7 (a) Band structure calculation of YbB_{12} from -15 eV to 15 eV, and for a narrower range near the Fermi energy E_F in (b). Green bands refer to the ytterbium f-electron bands, and orange bands are ytterbium d-electron bands, while boron bands are in purple. (c) The calculated electron Fermi surface for a small negative energy shift of the conduction bands, and the corresponding angular dependence of the quantum oscillation frequencies in the [001]-[111]-[110] rotation plane. (d) The calculated hole Fermi surface for a positive energy shift of the valence bands, and the corresponding angular dependence of the quantum oscillation frequencies in the same rotation plane. For both calculations we find small Fermi surface pockets with heavy masses ($\approx$ 6 electron masses for the electron pockets, and $\approx$ 9 electron masses for the hole pockets). (e) The first Brillouin zone of a face-centred cubic unit cell marking the special reciprocal lattice positions. Adapted from Ref. [11], with band structure calculations performed by Michelle D. Johannes.

with earlier calculations [180, 183, 184]. We find big Fermi pockets, as shown in Fig. 5.6b, with low effective masses. We also carried out torque magnetisation measurements on single crystals of LuB_{12} to see if quantum oscillation measurements on LuB_{12} single crystals grown by the same group as our YbB_{12} single crystals would reproduce this result. We identified quantum oscillation frequencies in the kT range with effective masses of around 0.5 bare electron masses (Fig. 5.6c-d), in good agreement with the band structure calculations and earlier quantum oscillation measurements [180, 181]. No commonalities are found with the small, heavy pockets identified by our YbB_{12} measurements. The analogy of a conduction electron Fermi surface that shows good resemblance to the measured Fermi surface of SmB_6 does not give the right Fermi surface for YbB_{12}, and we thus need to consider other scenarios.

We next consider what would be the resulting Fermi surface with a relative shift of the energy levels near the Fermi level. This could potentially be a Zeeman splitting, which could be brought about by the applied magnetic field. These bands are flat due to the localised f-electrons, and are expected to yield heavy effective masses. Fig. 5.7c shows the resulting Fermi surface consisting of twelve small ellipsoidal electron pockets for a small negative shift of the conduction bands, and Fig. 5.7d shows the resulting Fermi surface of eight peanut-shaped hole pockets for a small positive shift of the valence bands. For both calculations we find small Fermi surface pockets with heavy masses of around $\approx 6-9$ electron masses. This represents an effective scenario to yield a Fermi surface comparable to a heavy fermion semimetal picture with both electron and hole pockets.

5.5 Evolution in onset of quantum oscillations as a clue to the Fermi surface origin

Thermodynamic signatures in both YbB_{12} and SmB_6 suggest it is novel quasiparticles, which only couple to a magnetic field, that give rise to the observed Fermi surfaces. Yet, we find two very different Fermi surfaces, indicating that the two Kondo insulators represent two different avenues for realising this novel state. Uniquely for YbB_{12}, the applied magnetic field seems to be an important tuning parameter. The sensitivity to an applied magnetic field is manifested in the intrinsic quantum oscillations whose onset tracks the insulator-metal transition as a function of angle. We find a region in the phase diagram with strong intrinsic quantum oscillations that overlaps with the insulating phase. Its extent reaches lower magnetic fields along angles where the applied field is more potent at weakening the insulating state.

The tuning power of the magnetic field on YbB_{12} is further demonstrated by Fig. 5.8a, that shows the band gap as a function of applied magnetic field for YbB_{12}. We note that

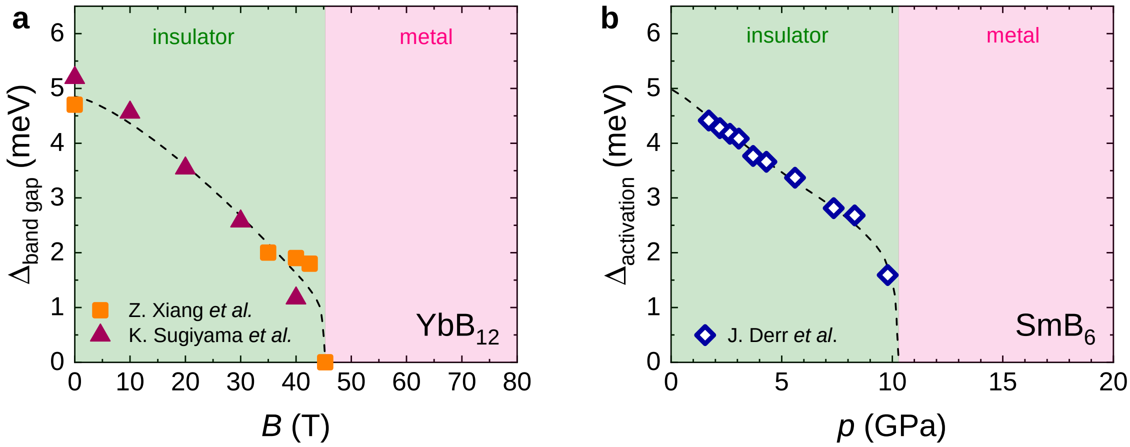

Fig. 5.8 (a) The hybridisation gap or band gap Δ_{bg} of YbB$_{12}$ as a function of magnetic field applied along the [001] direction [12, 166]. The dashed line is a guide to the eye. YbB$_{12}$ undergoes an insulator-to-metal transition at a magnetic field of ≈ 46 T [12, 166, 179]. (b) The activation gap Δ of SmB$_6$ as a function of applied pressure for a floating zone-grown sample [52]. The dashed line is a guide to the eye. SmB$_6$ undergoes an insulator-to-metal transition at an applied pressure of ≈ 10 GPa. We note that the Arrhenius fit can lead to different gap energies depending on the temperature range used, and care should be taken when gap values are compared between different reports. In (a) garnet triangles mark the band gap energies for a range of 5 K to 12 K [166], while orange squares are band gap energies for range of 4 K to 12 K [12], making the comparison between them apt. In (b), a temperature range of 10 K to 300 K is used.

in the case of YbB$_{12}$ the literature more commonly quotes the band gap or hybridisation energy [12, 166, 175], which is twice the value of the activation gap that appears in the Arrhenius equation, $1/\rho \propto \exp\left(-\Delta/k_{\mathrm{B}}T\right)$. In the case of SmB$_6$, the energy value quoted is usually the activation energy Δ, as it appears in the formula. In Fig. 5.8a we see the band gap of YbB$_{12}$ reduce from 5 meV at zero field to ≈ 1 meV before an insulator-metal transition at ≈ 46 T. We contrast this to the effect of applied pressure on SmB$_6$. Fig. 5.8b shows the activation gap of SmB$_6$, which reduces as a function of applied pressure, with the insulating gap terminating at ≈ 10 GPa. In effect, we find the same phase diagram for SmB$_6$ and YbB$_{12}$, but for different tuning parameters, namely SmB$_6$ is metallised with applied pressure, and YbB$_{12}$ is metallised with applied magnetic field. Interestingly, we see no transition to a metallic phase with pressure for YbB$_{12}$ up to 160 GPa [185], and no transition with magnetic field for SmB$_6$ up at at least 90 T [53].

The observed conduction electron Fermi surface in SmB_6 has been postulated to exist due to the system's proximity to a metallic phase, with a still finite charge gap but a closed gap for neutral quasiparticles, and a delicate dependence on the applied pressure or chemical pressure of the sample [29]. We highlight a similar scenario for YbB_{12}, where the proximity to a metallic phase exists in the magnetic phase diagram, and field tuning leads to a Fermi surface mirroring that of a heavy semimetal. Whilst the character of the Fermi surface is different from that of SmB_6, we identify a closely related origin from novel quasiparticles as ascertained by the thermodynamic signatures, and a finite band gap up to the insulator-metal transition. However, many aspects of our results are still unclear. We are still missing a complete angular dependence of the oscillation frequencies. Further measurements are also needed to discern whether the Shubnikov–de Haas and de Haas–van Alphen oscillations could be consolidated, and to see what happens to the Fermi surface at the insulator-metal transition. These future investigations could aid theoretical efforts to explain the heavy Fermi surface in YbB_{12}, and whether a common theoretical framework could also describe SmB_6.

Chapter 6

Superconductivity and quantum oscillations in $YBa_2Cu_3O_{6.55}$

6.1 Introduction

In this chapter, we study the nature of quantum oscillations within the high magnetic field pseudogap ground state. We find that quantum oscillations appear within a high magnetic field regime that in fact conceals a robust zero resistivity superconducting state with a large antinodal pairing gap. We identify these quantum oscillations (also presented in Ref. [186]) to arise from gapless nodal regions of the Brillouin zone, while the antinodal regions are strongly gapped, resembling the anisotropic pseudogap state at high temperatures [187, 188]. We thus return to the question of how quantum oscillations are to be interpreted within a non-Fermi liquid picture [189].

6.2 Previous explorations of the Brillouin zone of underdoped $YBa_2Cu_3O_{6+x}$

Spectroscopic techniques were first to examine the electronic structure of the cuprates. They found large Fermi-liquid-like hole pockets for overdoped $Bi_2Sr_2CaCu_2O_{8+x}$, but surprisingly

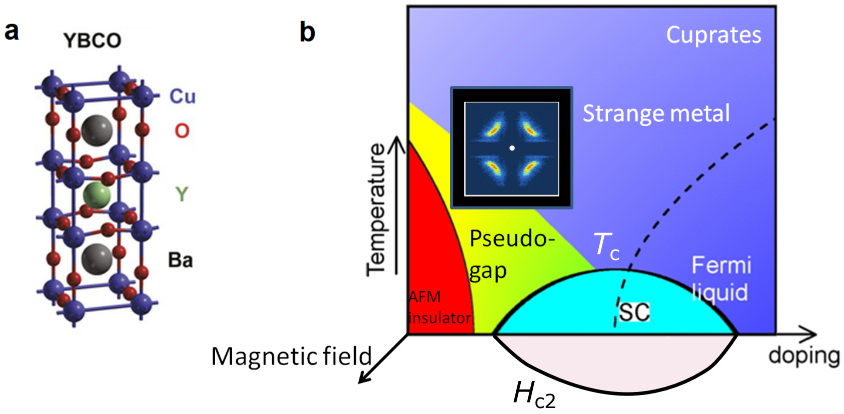

Fig. 6.1 (a) The orthorhombic unit cell of $YBa_2Cu_3O_{6+x}$ with two CuO_2 planes and one CuO chain per unit cell. Doping increases the oxygen content in the chains, in turn transferring holes to the superconducting CuO_2 planes. Adapted from Ref. [190]. (b) A schematic phase diagram of the cuprate superconductors as a function of doping highlighting the many orders that are at play. In this Chapter we focus on the high magnetic field ground state of the underdoped pseudogap regime that is host to quantum oscillations, as shown by an extension of the phase diagram along a third axis corresponding to applied magnetic field in the schematic.

found no evidence for a coherent Fermi surface in underdoped samples, and instead identified disconnected Fermi arcs located in the nodal regions [191, 192]. Spectroscopic measurements on $YBa_2Cu_3O_{6+x}$ proved to be more difficult, as the surface of cleaved samples self-dope to a very high oxygen content. Doping-dependent measurements were only realised by surface doping with with potassium, which revealed Fermi arcs similar to those observed for other cuprates (see Fig. 6.2a) [193]. The Fermi arcs highlight the nodal-antinodal dichotomy that characterises the pseudogap phase of the phase diagram. The pseudogap has a maximum in the antinodal regions of the Brillouin zone, but goes to zero at the nodes, presaging the analogous momentum-dependence of the superconducting gap below T_c. Oxygen doping seems to weaken the pseudogap, with the size of the ungapped Fermi arcs increasing with doping and leading to the closed Fermi surface observed on the overdoped side [194].

Quantum oscillations were observed for overdoped $Tl_2Ba_2CuO_{6+x}$, finding a large hole pocket [196], following the canon established by spectroscopic measurements. What came as a surprise was when quantum oscillations were discovered in underdoped $YBa_2Cu_3O_{6+x}$ [15], the side of the phase diagram without a coherent Fermi surface. Quantum oscillation mea-

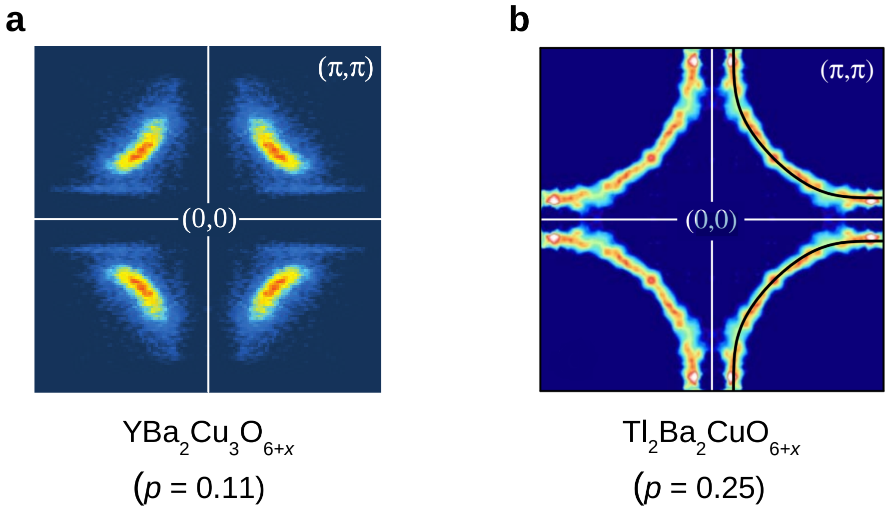

Fig. 6.2 The Fermi surface observed by ARPES for $T < T_c$ (a) in underdoped $YBa_2Cu_3O_{6+x}$ ($p = 0.11$, achieved by surface doping) [193], revealing a partially gapped Brillouin zone with nodal Fermi arcs, and (b) in overdoped $Tl_2Ba_2CuO_{6+x}$ ($p = 0.25$) [195], revealing large hole pockets.

surements revealed a small electron pocket, much smaller than the hole pockets found for the overdoped side (see Fig. 6.3). The same pocket was identified by magnetic torque [189] electrical transport [15], specific heat [197], thermal conductivity [18] and thermoelectricity measurements [198]. The oscillations were confirmed to originate from well-defined quasiparticles obeying Fermi-Dirac statistics [199]. A close connection with charge order was suggested by the comparable range of dopings where quantum oscillations were observed (hole dopings between $p = 0.08$ and 0.15 [31, 200]), and the range of dopings with charge density wave correlations (hole dopings between $p = 0.08$ and 0.16 [201]). Whilst the frequency of the oscillations was found to only modestly increase with doping, a much stronger dependence on doping was found for the effective mass, which diverges when approaching hole dopings $p = 0.08$ and 0.18 [31, 200]. The effective mass has a minimal value near $p = 0.11$, which coincides with the doping that has the lowest onset field of quantum oscillations.

One of the central questions became how Fermi arcs could be related to the coherent Fermi surface observed by quantum oscillations. Proposals identified the role of translational symmetry breaking in Fermi surface reconstruction schemes that could yield the observed

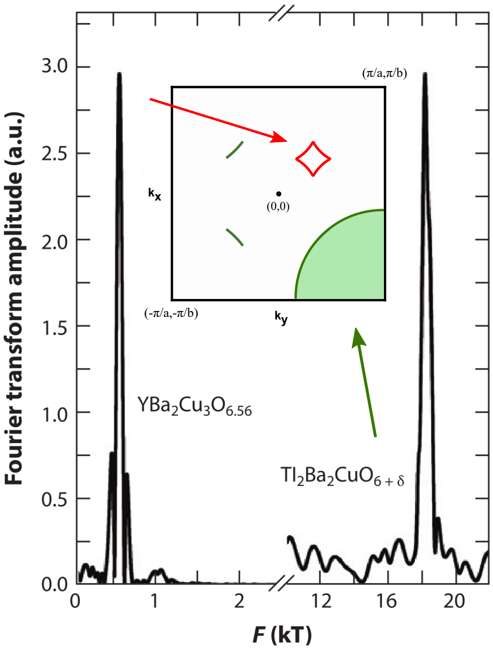

Fig. 6.3 The strikingly different quantum oscillation frequencies seen for underdoped and overdoped cuprates. Measurements on overdoped $Tl_2Ba_2CuO_{6+x}$ ($p \approx 0.26$) [196] find a large hole pocket centred at the corners of the Brillouin zone (green cylinder), in accordance with ARPES results. Surprisingly, quantum oscillations in underdoped $YBa_2Cu_3O_{6+x}$ ($p = 0.11$) reveal an electron pocket thirty times smaller (red diamond), which cannot be trivially reconciled with the disjointed Fermi arcs seen by ARPES. Adapted from Ref. [202].

electron pockets [203]. Experimental progress through detailed quantum oscillation measurements [204] confirmed that the measured Fermi surface originates from reconstruction by ordering wavevectors, that match the incommensurate wavevectors measured by X-ray [205, 206]. The Fermi surface geometry inferred from quantum oscillation measurements is compatible with a charge superlattice model that places the electron pocket near the nodal regions, answering another important question, the location of the pocket. A similar small electron pocket with staggered twofold warping was identified for $YBa_2Cu_4O_8$ [207], the stoichiometric analogue of $YBa_2Cu_3O_{6+x}$. Curiously, $YBa_2Cu_4O_8$ does not show charge density wave correlations in zero magnetic field [205], suggesting that the magnetic field plays an important role in enhancing charge order. Quantum oscillations in the pseudogap regime have only been observed for one other hole-doped cuprate, $HgBa_2CuO_{4+x}$ [32]. It has a simpler, tetragonal unit cell, with only one CuO_2 plane and no CuO chains. A similarly small electron

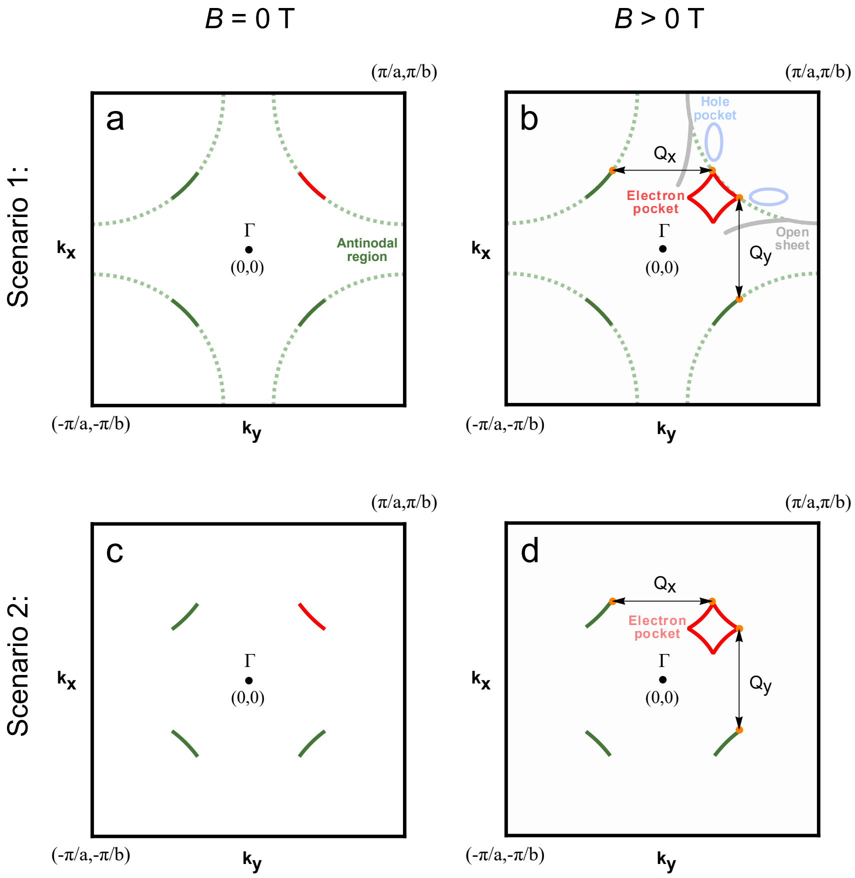

Fig. 6.4 Possible scenarios of the Fermi surface in underdoped $YBa_2Cu_3O_{6+x}$. The crucial difference concerns whether the Fermi arcs observed by ARPES are part of a larger Fermi surface, but the antinodal parts are not observed due to fluctuations (scenario 1), or the Fermi arcs are sharply defined objects with the complete gapping of the rest of the Brillouin zone (scenario 2). High magnetic field measurements are expected to reveal distinguishing features, as the Fermi surface in scenario 1 reconstructs into an electron pocket accompanied by two hole pockets and open Fermi surface sheets [209], whereas in scenario 2 it reconstructs into a single isolated nodal electron pocket. Proposed reconstruction schemes include biaxial [210] and uniaxial charge order [211, 212].

pocket was observed, but without any side-frequencies, and therefore no bilayer splitting, and was interpreted in terms of reconstruction by a biaxial charge density wave. In contrast, the nature of the charge order leading to the Fermi surface reconstruction in $YBa_2Cu_3O_{6+x}$ and the role of magnetic field remain open questions, with spectroscopic evidence for both biaxial and uniaxial charge density wave [208].

It is important to examine the nature of the pseudogap, and in turn its role on the observed Fermi surface. We distinguish between two scenarios. In one scenario the absence of antinodal quasiparticles measured at elevated temperatures arises due to thermal or classical fluctuations, and the Fermi arcs are constituents of a large hole pocket (Fig. 6.4a). In an alternative scenario the Fermi arcs are isolated features of the Brillouin zone with a complete gapping of antinodal quasiparticles (Fig. 6.4c). The former scenario is consistent with the pseudogap due to thermal or classical fluctuations, whereas the latter scenario would require an additional order parameter associated with the pseudogap [103, 213–216]. This also has implications on the Fermi surface that evolves under the effect of charge density wave order in high magnetic fields, particularly on the number of sections present in the Fermi surface. In the first scenario the nodal electron pocket is joined by two smaller hole pockets and open sheets near the antinodes (Fig. 6.4b), whereas in the second scenario the Fermi surface consists solely of an isolated nodal electron pocket (Fig. 6.4d). In the next section we present recent quantum oscillations measurements that probe the momentum space to establish which scenario manifests in high magnetic fields.

6.3 Isolated nodal Fermi surface in $YBa_2Cu_3O_{6.55}$

We distinguish between the two scenarios based on whether their respective signatures manifest in the measured quantum oscillations. One of the main constituents of the Fermi surface predicted by the first scenario are the small hole pockets. They would be expected to produce a second oscillation frequency, a fraction of the main frequency, and to appear in both de Haas–van Alphen and Shubnikov–de Haas oscillations. Ref. [217] presented *c*-axis resistivity data that indicated an $F \approx 90$ T oscillation frequency, that they could trace over 1.5 oscillation periods, and associated it with the small antinodal hole pockets. If they exist, these pockets should also lead to oscillations in the de Haas–van Alphen effect, with an amplitude that is comparable to that of the main frequency based on Lifshitz–Kosevich theory [13, 186]. However, in all de Haas–van Alphen studies so far [204, 218], and in our own measurements also, there has been no evidence for such a frequency. A possible explanation for the absence of this frequency in de Haas–van Alphen measurements could be quantum interference [219], which leads to a slow frequency, that does not correspond to any Fermi pockets, to appear solely in the Shubnikov–de Haas effect. A conclusive investigation of this frequency is made difficult by the high onset field of the quantum oscillations. This limits the number of oscillation periods that would occur between 20 T and 100 T to three, and makes it challenging to establish the periodicity of any minor oscillating features.

The Fermi surface predicted by the first scenario also comprises open sheets located in the antinodal regions. Whilst open sheets do not yield quantum oscillations, they are expected to alter the waveform of quantum oscillations produced by closed pockets. The shape of the waveform varies with the relative contribution from open sheets, as demonstrated by high magnetic field measurements of organic superconductors [220, 27]. Conversely, the absence of open sheets also leads to a particular waveform, giving us a quantitative method of assessing whether open sheets are present and contributing to the measured oscillations. Such studies on $YBa_2Cu_3O_{6+x}$ have been challenging, but here we present high-resolution quantum oscillation measurements on $YBa_2Cu_3O_{6.55}$ (hole doping of $p = 0.108$) as a result of improved sample quality and measurement sensitivity. This is demonstrated by a comparison to quantum oscillations measured on a previous generation of samples (Fig. 6.5a). We find the damping due to impurities for our present samples to be significantly lower than for the previous generation of samples, as demonstrated by the Fourier transform of the measured oscillations. We resolve five Fourier harmonics and a corresponding lower rate of exponential decay (shown by the dashed lines in Fig. 6.5b, quantified by the damping factor Γ', see Chapter 2), as opposed to only three Fourier harmonics resolved for the previous generation of samples and a higher rate of decay. We make a comparison of the amplitude of the quantum oscillations by rescaling them to match in the infinite magnetic field limit ($F/B \rightarrow 0$) using the extrapolation made in Fig. 6.5b. The Dingle damping factor of our present samples is found to be $\Gamma' = 83$ T, which is significantly lower than that of the previous generation of samples ($\Gamma' = 140$ T [204]).

For most measurement angles the quantum oscillations feature a beat pattern caused by additional frequencies that appear due to interlayer coupling and magnetic breakdown [204]. We avoid the complications this would cause with the waveform analysis by performing measurements with the magnetic field applied at $\theta = 36^\circ$ with respect to the crystalline c-axis,

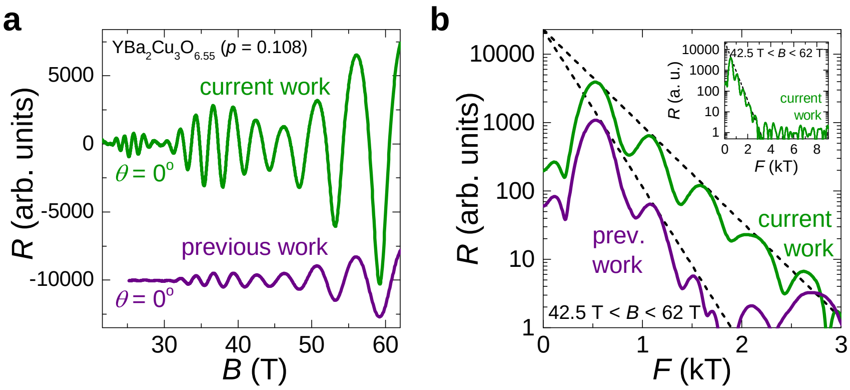

Fig. 6.5 (a) Comparison of the observed quantum oscillations in our current samples (green) with that of observed in a previous generation of samples (violet) [204]. We scale the amplitudes such that they match in the infinite-field limit, where all damping factors saturate to unity. The higher quality of our samples, and therefore a smaller impurity damping factor, leads to oscillations much larger in amplitude. (b) The Fourier transform reveals frequency peaks down to the fifth harmonic, whereas the larger impurity damping factor of samples from previous generations only makes the first three harmonics observable. Dashed lines denote the damping fits to the FFT peaks, which decay exponentially with harmonic number.

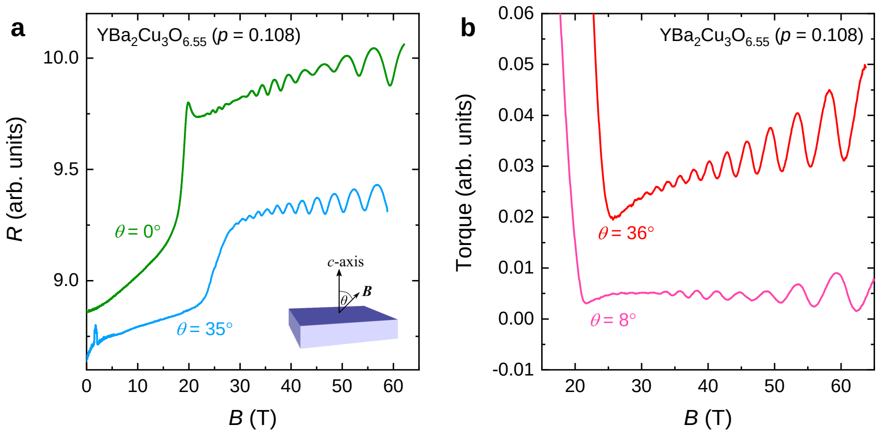

Fig. 6.6 Quantum oscillations observed for underdoped $YBa_2Cu_3O_{6.55}$ (hole doping of $p = 0.108$) at $T = 1.5$ K in (a) contactless resistivity, and (b) magnetic torque in pulsed magnetic fields. The oscillations exhibit a prominent beat pattern for small angles, necessitating measurements at angles near 36°, where there is only a single oscillation frequency, and therefore no beat pattern.

the angle where the waveform consists of only a single frequency as established by previous angle-resolved measurements [204]. Fig. 6.6a shows contactless resistivity measurements

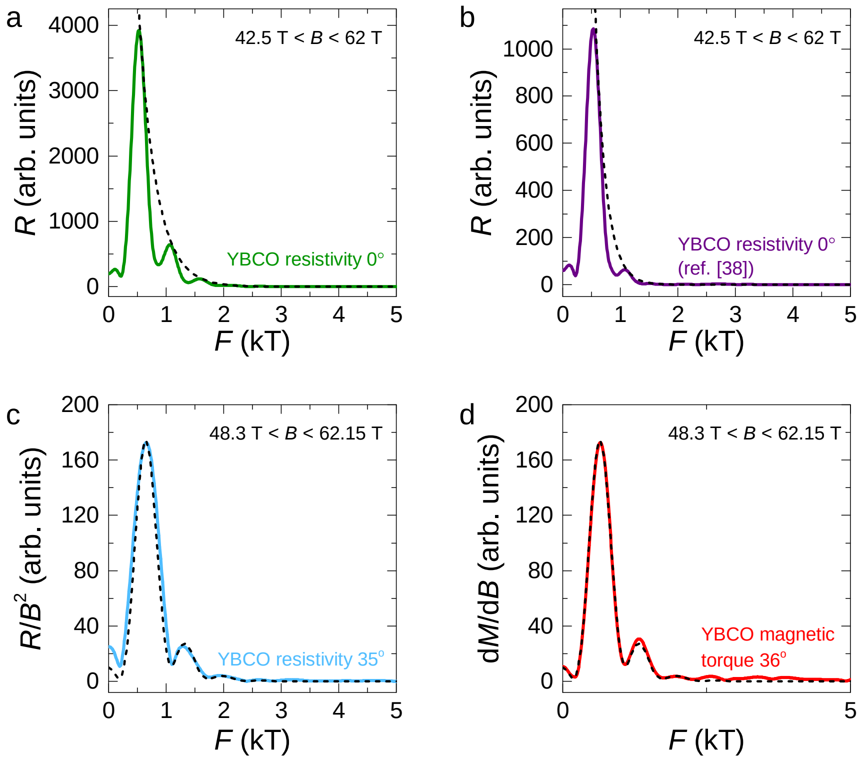

Fig. 6.7 The Fourier transforms of the field sweeps shown in Fig. 6.6. The second frequency peak near 1.2 kT corresponds to the second harmonic of the main frequency, with further harmonics also visible on a logarithmic plot. Dashed lines in panels (a) and (b) represent the exponential amplitude damping with increasing harmonic index, whilst in panels (c) and (d) they represent numerical simulations, which we also plot in Fig. 6.8.

performed at $\theta = 0^\circ$ and 35° with sizeable quantum oscillations with and without a beat pattern, and Fig. 6.6b shows comparable quantum oscillations measured in torque magnetisation at $\theta = 0^\circ$ and 36°. Even before background subtraction the oscillations appear asymmetric, caused by the rich harmonic content. We determine the sign of the quantum oscillations by measuring the sign of the magnetic hysteresis caused by vortex pinning during the up- and down-sweeps of the magnetic field. Fig. 6.7 shows the corresponding Fourier transforms for the oscillation periods at the highest magnetic fields, where the harmonics are best resolved.

In Chapter 2 we discussed the Lifshitz–Kosevich theory, that described quantum oscillations produced by an ideal two-dimensional Fermi surface with zero reservoir density of states at the

Fermi level (i.e. no open sheets, or additional sections of Fermi surface that are excessively damped). The chemical potential is constant and all the harmonics have the same sign, and contribute in a way that the de Haas–van Alphen waveform is a perfect forward-leaning sawtooth wave when all phase smearing terms saturate to unity ($T = 0$ K, zero impurity damping and no spin-splitting). With phase smearing the higher harmonics are exponentially suppressed, resulting in a sinusoidal waveform. The presence of one-dimensional open sheets, however, has been shown to lead to an altered waveform at high magnetic fields, where the chemical potential becomes pinned to the highest occupied Landau level and therefore oscillates with the magnetic field [27]. The relative amplitude and the sign of each harmonic component becomes dependent on the open sheets' contribution to the density of states at the Fermi level (the reservoir density of states denoted ζ_{res}), which leads to the waveform of the oscillations to becoming more backward-leaning with increasing reservoir density of states ζ_{res}. In the limit of only open sheets contributing to the density of states the waveform becomes a perfect inverted sawtooth [27]. Here, we analyse the shape of the observed quantum oscillations in both magnetisation and contactless resistivity. We determine the relative size and sign of each harmonic to quantify the size of the reservoir density of states ζ_{res} with respect to the two-dimensional Fermi surface density of states $\zeta_{\mathrm{2D},0}$.

In Fig. 6.8a we plot three periods of the measured quantum oscillations in magnetisation (first derivative of the chemical potential μ), and in magnetic susceptibility and contactless resistivity (second derivative of μ with respect to applied magnetic field). We find that the waveform shows striking similarities to the quantum oscillation waveform observed for GaAs, an ideal two-dimensional electron gas with zero reservoir density of states (Fig. 6.8c). The important features that are displayed by both materials are the forward-leaning sawtooth waveform in magnetisation, and the inverted U-shaped waveform in the magnetic susceptibility and contactless resistivity. We find a good match with a model simulation for a complete absence of reservoir density of states (black line). The simulations predict the amplitude of the harmonics to decay exponentially with harmonic number (upper panel of Fig. 6.8b) and to have the same sign as the main frequency (lower panel of Fig. 6.8b), mirroring the results for GaAs (Fig. 6.8d). We find the same behaviour for $YBa_2Cu_3O_{6.55}$, with the resistive oscillations

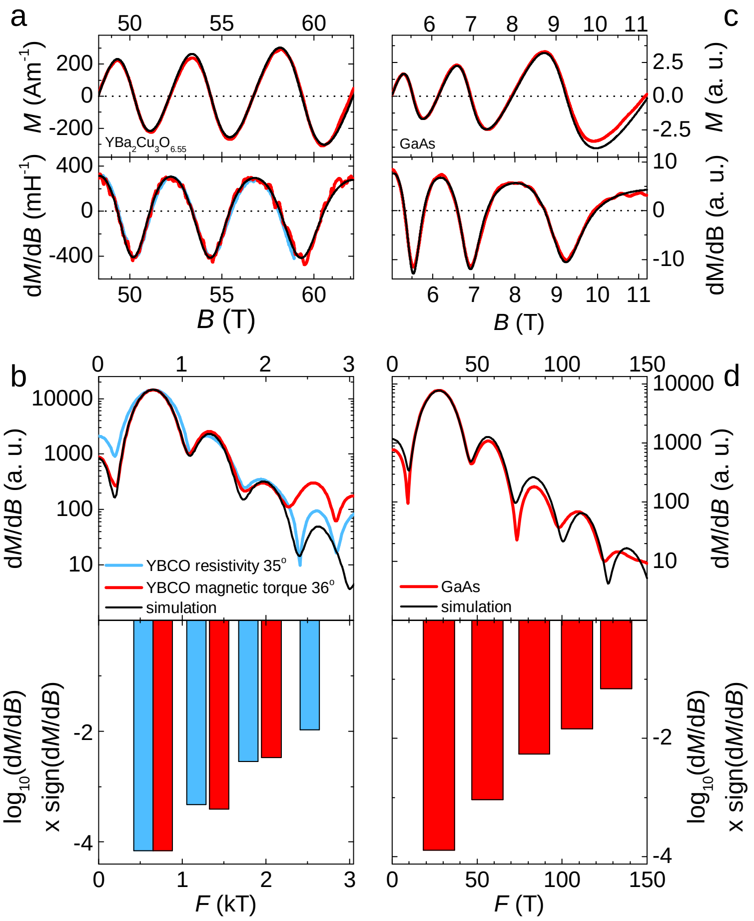

Fig. 6.8 Comparison of the shape of the quantum oscillation waveform of $YBa_2Cu_3O_{6.55}$ and GaAs [221], a two-dimensional electron gas with zero reservoir density of states. (a) The observed oscillations in magnetisation (red), magnetic susceptibility (red) and contactless resistivity (blue) overlayed with simulated quantum oscillations (black), reveal forward-leaning sawtooth oscillations, similar to what has been observed for GaAs. Corresponding Fourier transform of (b) $YBa_2Cu_3O_{6.55}$, and (d) GaAs showing the exponential decay of successive harmonics. The lower panels show the logarithm of the Fourier transform amplitude multiplied by the sign of each Fourier transform peak as inferred from their phase. The forward-leaning sawtooth waveform and linear decrease of the logarithmic amplitude of successive harmonics in both materials are consistent with the expectation for an isolated two-dimensional Fermi surface with no background reservoir density of states.

revealing four harmonics and the magnetic oscillations revealing three harmonics, with the amplitudes of the harmonics falling on an exponential curve.

Next, we explore the key signatures of quantum oscillations for materials with one-dimensional open sheets. Fig. 6.9 shows the de Haas–van Alphen oscillations of $YBa_2Cu_3O_{6.55}$

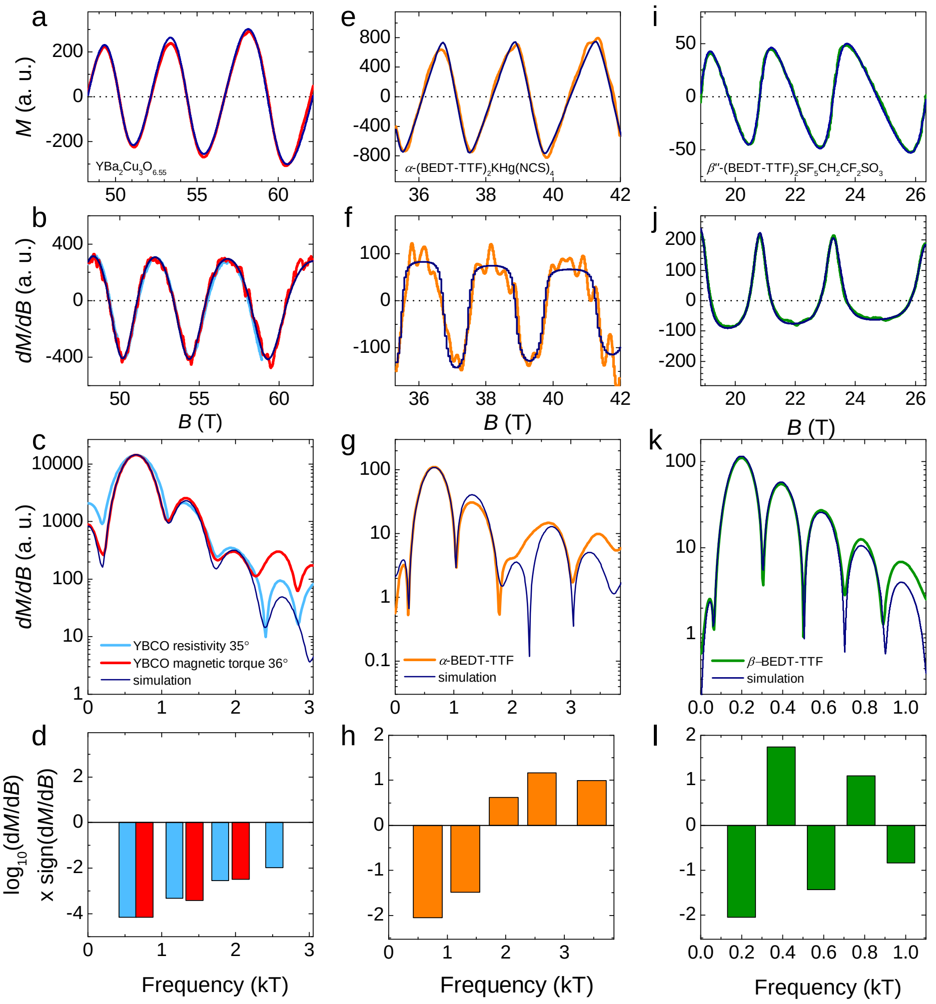

Fig. 6.9 Comparing the de Haas–van Alphen oscillations observed for (a-d) $YBa_2Cu_3O_{6.55}$ ($\zeta_{\rm res}/\zeta_{\rm 2D,0} \approx 0$) to (e-h) that of an organic metal with reservoir density of states comparable in size to the main two-dimensional Fermi surface density of states ($\zeta_{\rm res}/\zeta_{\rm 2D,0} = 0.4$) [27, 222], and (i-l) an organic metal with a very large reservoir density of states ($\zeta_{\rm res}/\zeta_{\rm 2D,0} = 5$) [220]. The waveforms display noticeable differences, arising from the amplitude and sign of the harmonics that are dependent on the size of the reservoir density of states (see panels (d), (h) and (l)).

with forward-leaning oscillations, contrasted with α-(BEDT-TTF)$_2$KHg(NCS)$_4$, an organic metal with reservoir density of states comparable in size to the main two-dimensional Fermi surface density of states ($\zeta_{\rm res}/\zeta_{\rm 2D,0} = 0.4$) [27, 222], and β''-(BEDT-TTF)$_2$SF$_5$CH$_2$CF$_2$SO$_3$, an organic metal with a very large reservoir density of states ($\zeta_{\rm res}/\zeta_{\rm 2D,0} = 5$) [220]. For the latter, the quantum oscillations in magnetisation display a clear inverted sawtooth waveform, with the derivative displaying a U-shaped waveform, the opposite of what we observed for $YBa_2Cu_3O_{6.55}$. We find the amplitude of the harmonics to decay exponentially with harmonic number (upper panel of Fig. 6.8b) and to have an alternating sign with increasing harmonic number. For α-(BEDT-TTF)$_2$KHg(NCS)$_4$ ($\zeta_{\mathrm{res}}/\zeta_{\mathrm{2D},0} = 0.4$), we find forward-leaning sawtooth oscillations in the magnetisation (theory predicts the waveform to become inverted for $\zeta_{\mathrm{res}}/\zeta_{\mathrm{2D},0} > 1$ [27]), and the derivative to display flat top peaks, which are caused by the negligible third harmonic, and lower harmonics that have opposite signs to the main harmonic.

For a quantitative analysis on whether the quantum oscillations of $YBa_2Cu_3O_{6.55}$ have any contributions from a reservoir density of states, we treat the reservoir size as a variable and look for the simulated waveform that gives the best agreement with the measured waveform. We plot the simulated amplitude of each harmonic relative to the amplitude of the fundamental frequency as a function of reservoir size (marked by solid lines in Fig. 6.10). We make a comparison to the measured relative amplitudes of the harmonics, which are marked by horizontal dotted lines. The best agreement is determined based on where they cross the simulated lines. By aggregating all the harmonics we determine that the best agreement is for a reservoir size of $\zeta_{\mathrm{res}}/\zeta_{\mathrm{2D},0} = 0.01 \pm 0.03$. This is a robust conclusion based on the results of two measurement techniques, and quantum oscillations with and without a beat pattern.

Thus, we confirm the absence of reservoir density of states at the Fermi level in $YBa_2Cu_3O_{6.55}$ with an upper bound of $0.03 \times \zeta_{\mathrm{2D},0}$. This is demonstrated by the forward-leaning sawtooth waveform resembling that of GaAs, the exponential decrease of successive harmonic amplitudes, and the quantitative comparison with simulations. Combined with the missing slower frequency oscillations in the de Haas–van Alphen effect [186], that would be expected for the antinodal hole pockets, we confirm that the Fermi surface is comprised of a single isolated Fermi surface pocket, as put forward by the second scenario. This is consistent with the low value of the finite linear specific heat coefficient [197], and the lack of any quasiparticle spectral weight in the antinodal regions as found by spectroscopy measurements [223]. Our results constrain future models of the pseudogap phase to those characterised by sharply truncated Fermi arcs with a hard antinodal gap.

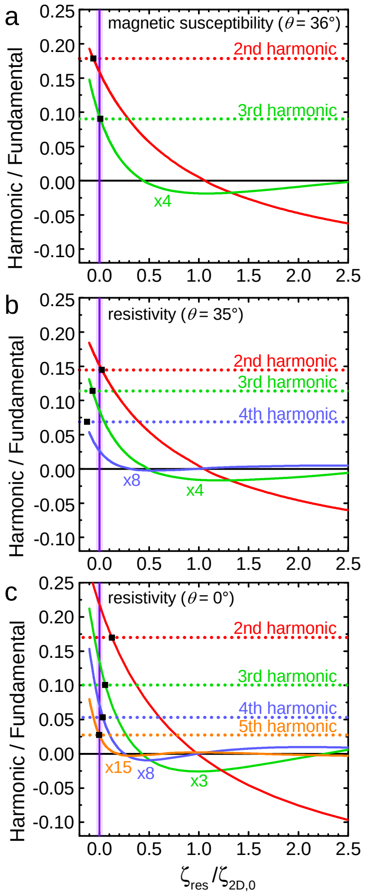

Fig. 6.10 The relative amplitude of the harmonics to the amplitude of the fundamental frequency as a function of the size of the reservoir density of states, simulated for magnetic susceptibility (panel (a)) and resistivity (panels (b) and (c)), as shown by solid curves. The measured relative amplitude of the harmonics are marked by dashed horizontal lines. The best agreement with the simulations is determined based on where they cross the simulated lines (marked by black squares). The arithmetic mean of the harmonics results in the size of the reservoir density of states ζ_{res} to be 1% of the main Fermi surface density of states $\zeta_{\text{2D},0}$ with a standard error of 3%.

6.4 Magnetic field resilient low-temperature superconductivity

Intriguingly, the similarities that we find between the pseudogap state and the nodal Fermi surface are at odds with the previously held view, that the quantum oscillations are the property of a conventional metallic state. This would require the superconducting order parameter to

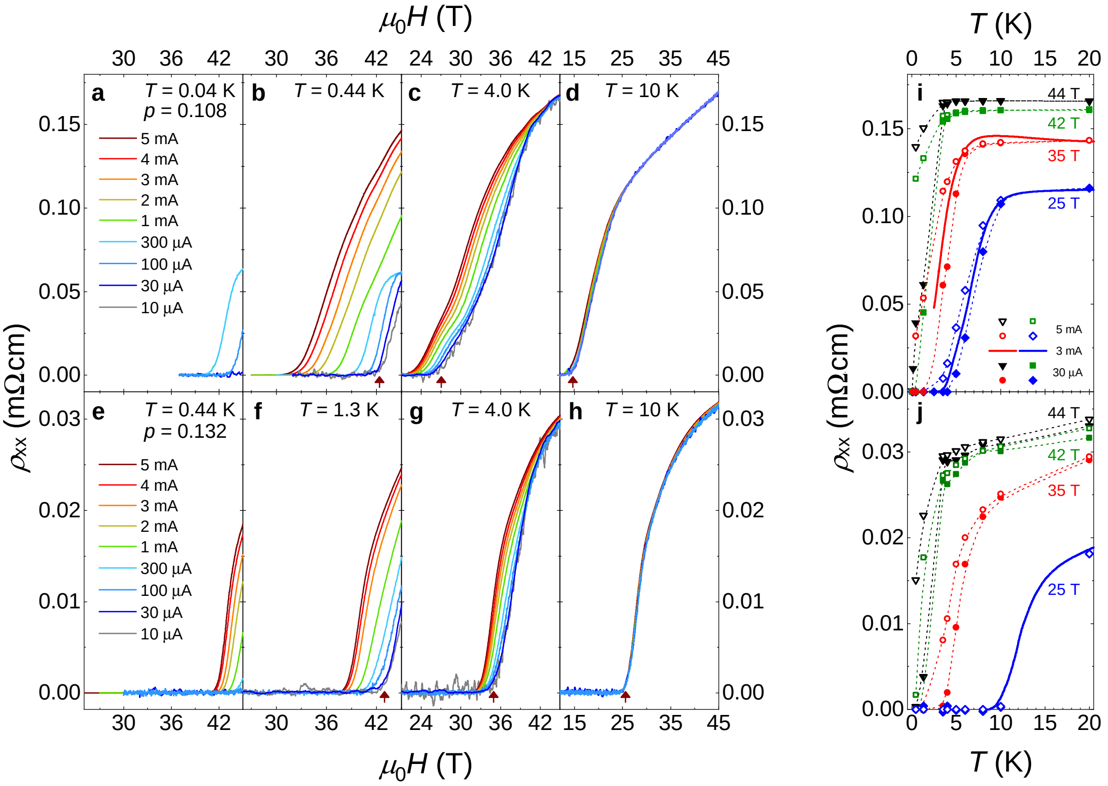

Fig. 6.11 Magnetic field sweeps of the in-plane electrical resistivity of $YBa_2Cu_3O_{6.55}$ (hole doping $p = 0.108$, panels (a-d)) and $YBa_2Cu_3O_{6.75}$ (hole doping $p = 0.132$, panels (e-h)) for different temperatures and measurement currents. We denote the onset field of finite electrical resistivity $\mu_0 H_r$ as the field above which the measured resistivity reaches 10^{-3} mΩcm. A measurement current of $I = 1$ mA converts to a current density of $j \approx 5$ Acm^{-2}. We see a current-dependence of the resistivity that becomes more striking at lower temperatures, specifically the fanning of the resistivity curves and the increase of $\mu_0 H_r$ as a function of applied current. We see the persistence of superconductivity up to the highest magnetic fields at the lowest temperatures (panels (a) and (e)). (i-j) Temperature sweeps of the in-plane electrical resistivity for different applied magnetic fields and measurement currents, revealing narrow transition widths for all applied magnetic fields and measurement currents.

be destroyed by a magnetic field of 20 T, as purported by pulsed field electrical transport experiments [18]. However, with these studies being limited to temperatures above 4 K, and conducted in rapidly changing pulsed magnetic fields that generate large eddy currents (of the order of $\approx 10^3$ Acm^{-2}), it prompts us for a closer inspection of the true extent of superconductivity.

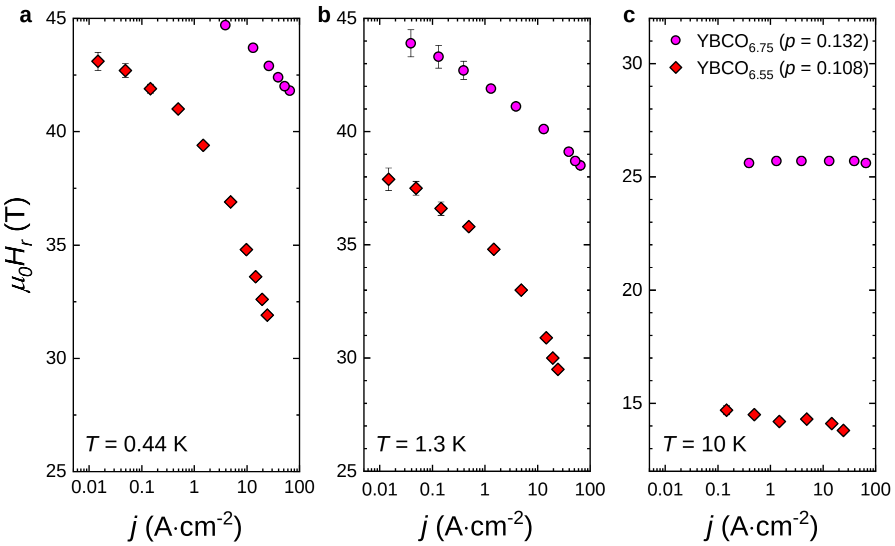

Fig. 6.12 The onset field of finite electrical resistivity $\mu_0 H_r$ as a function of measurement current density for two dopings at three different temperatures. With decreasing temperature, the current-dependence becomes more significant, with no saturation seen for the current ranges we employed.

We employed DC fields up to 45 T and a wide range of measurement currents (spanning three orders of magnitude, with $j = 0.05 - 25$ Acm^{-2}). We studied two dopings, $YBa_2Cu_3O_{6.55}$ (hole doping $p = 0.108$) and $YBa_2Cu_3O_{6.75}$ (hole doping $p = 0.132$), which Ref. [18] found to enter the normal state at 24 T and 30 T, respectively. We performed magnetic field sweeps at fixed temperatures, which we repeated for several measurement currents, allowing us to identify the onset magnetic field of finite resistivity $\mu_0 H_r$ as a function of both temperature and measurement current. Fig. 6.11a-h shows such magnetic field sweeps performed at different temperatures and measurement currents for $YBa_2Cu_3O_{6.55}$ and $YBa_2Cu_3O_{6.75}$. We find an increasing current-dependence with decreasing temperature, with temperatures below 4 K showing marked non-ohmic I-V dependence. Surprisingly, we also find the onset magnetic field of finite resistivity $\mu_0 H_r$ to become current-dependent at low temperatures, with $\mu_0 H_r(T = 0.44\text{ K})$ for $YBa_2Cu_3O_{6.55}$ varying by more than 10 T with measurement current (Fig. 6.11b). Even more importantly, when using low measurement currents (30 µA and below) we find no suppression of superconductivity up to 45 T at $T = 0.04$ K in the case of $YBa_2Cu_3O_{6.55}$, and at

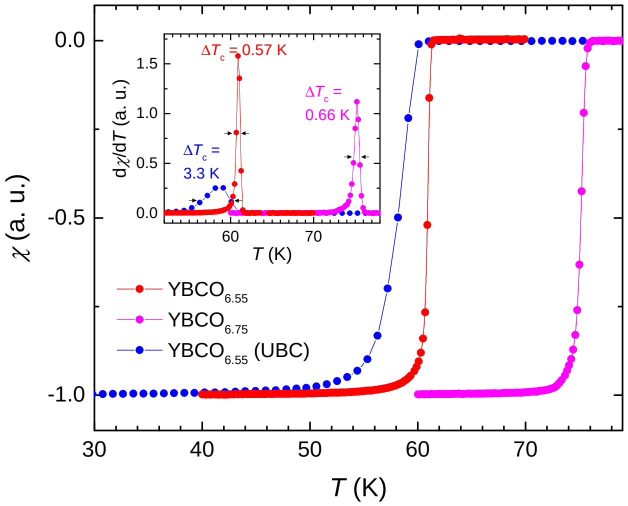

Fig. 6.13 Magnetic susceptibility measurements (zero field cooled) at an applied magnetic field of 0.2 mT applied along the *c*-axis on the same crystals we employed for the electrical transport measurements, revealing sharp transition widths, at least five times narrower than observed for the previous generation of samples, indicative of high sample quality.

$T = 0.44$ K in the case of $YBa_2Cu_3O_{6.75}$, in direct contrast with pulsed field measurements [18]. In Fig. 6.12 we plot $\mu_0 H_r$ as a function of current for different temperatures. The increase in the onset field with decreasing current becomes more significant at lower temperatures. This figure also shows the expected increase of $\mu_0 H_r$ with doping. It displays no saturation in the value of $\mu_0 H_r$ for the measurement currents employed.

We find no evidence for surface or filamentary superconductivity, with sharp superconducting transitions in the temperature sweeps measured at different magnetic fields and measurement currents (Fig. 6.11i-j). Homogeneity of the measured samples is also evidenced by the narrow transition widths found by SQUID magnetic susceptibility measurements performed at low magnetic fields (Fig. 6.13). We find the transition width to be five times narrower than for the previous generation of samples with comparable doping.

A plot of the measured values of the onset field $\mu_0 H_r$ as a function of temperature for different currents is shown in Fig. 6.14. The magnetic phase diagram revealed by our measurements shows a sharp upturn in $\mu_0 H_r$ below 15 K, and corresponds to a low-temperature magnetic field resilient superconducting phase, that remains unsuppressed up to at least 45 T. A similar upturn

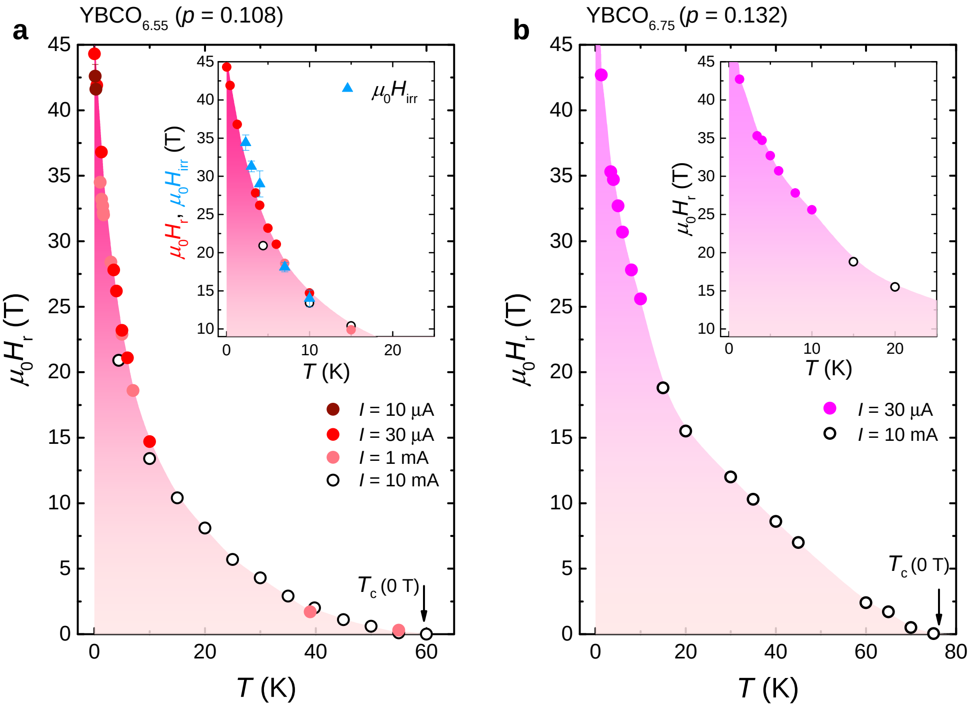

Fig. 6.14 The magnetic phase diagram of (a) $YBa_2Cu_3O_{6.55}$ and (b) $YBa_2Cu_3O_{6.75}$ based on electrical transport measurements performed in DC magnetic fields. We find that superconductivity persists up to the highest magnetic fields upon applying low measurement currents. The insets show a magnified view of the low-temperature region, with the irreversibility field values $\mu_0 H_{irr}$ obtained from magnetic torque measurements of $YBa_2Cu_3O_{6.55}$ (see Fig. 6.15), displaying a facsimile of the phase boundary formed by the finite resistive onset field $\mu_0 H_r$.

in the onset field of finite resistivity was observed for $Tl_2Ba_2CuO_{6+x}$ ($p \approx 0.26$) [225], another cuprate that exhibits quantum oscillations [196]. In the same study, they also found magnetic torque hysteresis due to vortex pinning up to at least 20 T in pulsed magnetic fields, even though T_c is only 10 K for this doping. Magnetic torque is a measurement technique that is sensitive to bulk superconductivity, for this reason we use it as a complementary technique to confirm the true extent of superconductivity in the magnetic phase diagram. Fig. 6.15a-b show up and down sweeps of the magnetic torque for $YBa_2Cu_3O_{6.55}$ at different temperatures. We see a hysteretic behaviour caused by vortex pinning, that extends to increasing magnetic fields with decreasing temperature, with hysteresis persisting up to at least 45 T at 0.04 K, in agreement with our electrical transport result. We denote the irresistibility field, the extent of the torque hysteresis in magnetic field, $\mu_0 H_{irr}$, and compare it to the onset field $\mu_0 H_r$ determined by

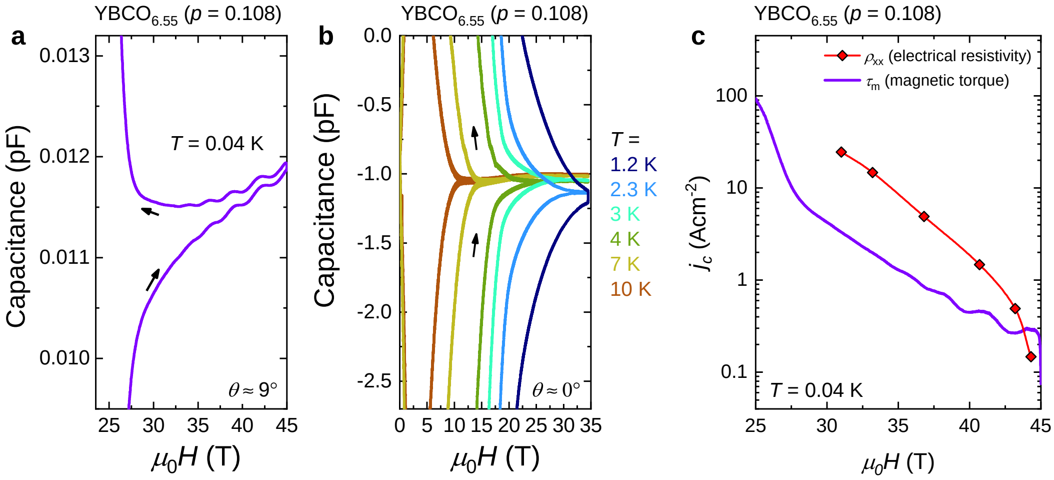

Fig. 6.15 (a-b) Capacitive torque magnetisation measurements of $YBa_2Cu_3O_{6.55}$ when the magnetic field is swept up and down at 0.04 K (panel (a)), and at higher temperatures (panel (b)), revealing the characteristic superconducting hysteresis caused by bulk vortex pinning. The field where the hysteresis terminates marks the irreversibility field $\mu_0 H_{irr}$, with its extent at the lowest temperature surpassing 45 T. This agrees with our inference based on electrical transport measurements of magnetic field resilient bulk superconductivity in $YBa_2Cu_3O_{6.55}$ and $YBa_2Cu_3O_{6.75}$. (c) The critical current density identified by electrical transport measurements (from Fig. 6.11), and the critical current density obtained from the absolute size of the torque hysteresis seen in magnetic torque measurements performed on the same sample. We see a good order of magnitude agreement. The conversion of the absolute size of the torque hysteresis is based on the Bean model [224].

electrical transport measurements, as shown in the inset to Fig. 6.14a. We find that $\mu_0 H_{irr}$ is in good agreement with $\mu_0 H_r$, tracing the extent of the low current onset field up to the highest magnetic fields, and thus confirming the existence of a low-temperature magnetic field resilient superconducting phase by a second measurement technique.

When the magnetic field is swept up/down, vortices leave/enter the sample through its boundary. This causes a non-uniform flux density profile, and therefore a torque hysteresis, and can be translated into a lossless critical current that is created to balance out the forces pinning vortices to defects. It leads to a negative magnetisation when the magnetic field is swept up, and a positive magnetisation when it is swept down. This is the basic behaviour proposed by the Bean model of the critical state and applies to the bulk of the sample [224]. With this in mind, we consider how the critical current from the Bean model compares to the applied current we identify from electrical transport measurements that causes vortex depinning and therefore finite resistance. The Bean critical current is proportional to the absolute size of the magnetic hysteresis, which we convert into a critical current density. The prefactors vary with sample geometry, but for a slab the critical current can be approximated to be [226]

$$j_c = 6\frac{\Delta M}{\pi r}$$

where ΔM is the size of the hysteresis loop in magnetisation (in units of A/m), and r is the effective sample radius. We plot the critical current obtained this way as a function of magnetic field in Fig. 6.15c, together with the critical current identified by electrical transport measurements. We find a good order of magnitude agreement, which represents further confirmation that our electrical transport measurements probe bulk behaviour.

In light of our findings that superconductivity survives up to at least 45 T in underdoped $YBa_2Cu_3O_{6+x}$, confirmed by both electrical transport and magnetic torque measurements, we consider past measurements that explored the magnetic phase diagram of $YBa_2Cu_3O_{6+x}$. Our measurements performed in DC magnetic fields, down to millikelvin temperatures and for a wide range of measurement currents supersede electrical transport measurements performed in pulsed magnetic fields [18], which argued to show a transition in modest magnetic fields to a normal metallic, and would have made these materials surprisingly conventional. Other measurements that argued for the suppression of superconductivity and the emergence of the normal state at modest magnetic fields include thermal transport and specific heat measurements. A closer inspection of the thermal transport results [18] reveals that the features identified are unlike the features associated with the suppression of superconductivity in type-II superconductors and Fermi-liquid-like Tl-2201 [227]. For these the residual linear term of the thermal conductivity is found to go from a large finite value above H_{c2}, the magnetic field where it saturates, to zero or small non-zero value at 0 T, corresponding to a robust transition that can be tracked across the entire measured field range. There are no measurements for $YBa_2Cu_3O_{6+x}$ that are low enough in temperature to determine the magnetic field dependence of the residual linear term of the thermal conductivity. Instead, Ref. [18] considered the thermal conductivity as a function of magnetic field. They proposed that the boundary between the normal state and the vortex state is indicated by a small step-like feature in the magnetic field dependence of the thermal conductivity, a drop less than 9% in value [18]. The same step-like feature was observed by Ref. [218], but associated it with charge order due to its temperature-independent position in magnetic field, that intersects the vortex boundary at a modest magnetic field, reminiscent of charge order signatures identified by NMR [228], X-ray [229], and differential susceptibility [218]. The anomaly observed in specific heat [230, 231] shows a similar temperature-independent behaviour above 7 K, with an upturn at low temperatures, that terminates at 24 T. This is much too low to be associated with the onset field $\mu_0 H_r$ and irresistibility field $\mu_0 H_{\mathrm{i}rr}$ values found by our electrical transport and magnetic torque measurements, and its temperature-independent behaviour for $T > 7$ K makes a charge order origin more likely. At the same time, evidence for the vortex state extending to much higher magnetic fields than ≈ 20 T, in line with our results presented in this section, has been provided by previous magnetic torque measurements [189, 218], Nernst effect measurements [232], and specific heat measurements, that found the linear specific heat coefficient to increase continually as the square of the magnetic field up to at least 45 T [197].

6.5 Superconductivity and non-ohmic resistivity

We examine the possible foundations of the observed superconducting state with its amplified sensitivity to the measurement current. In the low temperature–high magnetic field regime $YBa_2Cu_3O_{6.55}$ displays a non-linear voltage-current dependence (see Fig. 6.16), with a strongly field-dependent onset field of finite electrical resistivity $\mu_0 H_r$ (see Fig. 6.12). This behaviour is unusual and cannot be described by a conventional vortex melting transition between a vortex solid and a vortex liquid phase. Here we discuss theories that provide interpretations for a non-linear voltage-current dependence in the context of a superconducting phase transition.

For conventional type-II superconductors the boundary between true superconductivity (with zero resistivity) and finite resistivity is defined by the first order phase transition between the vortex solid phase and normal phase. Life is not so simple in the case of high-T_c type-II superconductors, where thermal fluctuations lead to an altered phase diagram with no well-defined H_{c2} transition line to the normal phase, and the boundary between superconductivity and finite resistivity is shifted to the boundary between the vortex solid and vortex liquid phases. For real materials one also has to consider disorder, which acts against the long-range order of the vortex solid. Finding a description of the vortex solid phase with true superconductivity (with zero resistivity) becomes challenging when disorder and the resulting vortex pinning are incorporated. For a long time the oft-cited model for vortex motion was the Kim-Anderson flux creep model [233], which incorporates pinning, but neglects interactions between vortices. It fails to be a complete description, however, as it finds that the resistivity is described by an Arrhenius equation, with zero resistivity only at $T = 0$ K, which would limit true superconductivity to just the Meissner phase.

A model that integrates thermal fluctuations, disorder and interactions between vortices and with pinning sites was provided by Fisher, Fisher, and Huse (FFH) [16, 17]. They describe a phase of immobile vortices frozen in a random pattern, which is the superconducting analogue of the magnetic spin glass phase. This equilibrium is reached through the competition between thermal fluctuations and the interactions between vortices and with disorder. The vortices do not form a vortex lattice, but still maintain phase-correlated long-range order. The evolution from vortex liquid to vortex glass is described via a critical scaling behaviour, predicting a continuous phase transition with a divergent characteristic length scale, in this case the phase-correlation length of the electron pair wavefunction. This represents a compelling parallel with our experimental observation of a phase boundary that evolves with the measurement current. The question becomes whether it could also account for the observed non-ohmic transport behaviour, and mark the boundary of the true, zero resistivity superconducting phase.

We consider the analytical description of the vortex glass phase provided by the FFH model. In contrast with the Kim-Anderson model, the scaling behaviour of the correlation length leads to the vanishing of the linear resistivity at a finite temperature, the critical temperature T_g as

$$\rho_{\text{lin.}} \propto (T - T_g)^s \tag{6.1}$$

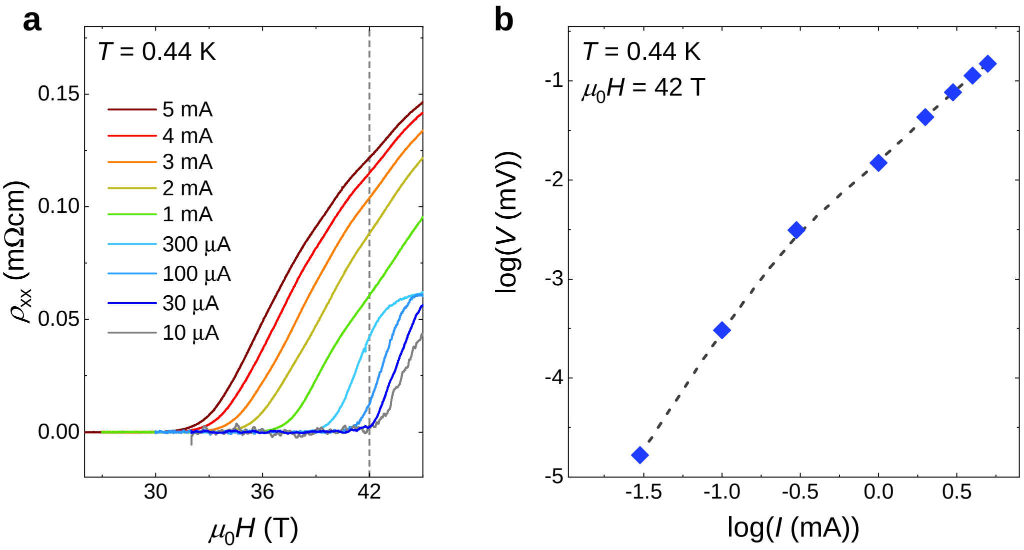

Fig. 6.16 (a) Magnetic field sweeps of the in-plane electrical resistivity of $YBa_2Cu_3O_{6.55}$ (hole doping $p = 0.108$) at $T = 0.44$ K for different measurement currents. We take cuts at fixed magnetic field values to obtain the I-V curve for different T and B. (b) As an example we plot the voltage-current dependence for $T = 0.44$ K and $\mu_0 H = 42$ T, which reveals a non-ohmic behaviour.

(where $\rho_{\text{lin.}}$ is the linear resistivity defined as $\rho_{\text{lin.}} = dE/dj|_{j\to 0}$). Another important result of the FFH model is that the energy cost of vortex loop creation goes as $U \propto j^{-\mu}$, where j is the current density, which leads to a power-law relation with the same exponent μ describing current decay. An even more pertinent result of the current-dependent U is a current-dependent nonlinear resistivity ($\rho_{\text{nonl.}} = E/j$). We obtain this by considering the Boltzmann probability of vortex loop creation due to spontaneous thermal fluctuations, given by exp[-$U/k_B T$], which in turn is proportional to the dissipation rate and therefore also to the nonlinear resistivity [16]. Hence, according to the FFH model, the voltage-current dependence in the vortex glass phase is given by

$$V \propto j \exp[-(j_T/j)^{\mu}] \tag{6.2}$$

where j_T is a characteristic current density with the temperature dependence $j_T \propto (1/T)^{1/\mu}$, and $0 \leq \mu \leq 1$, with $\mu = 1$ in the Meissner phase. We note that according to this equation any finite current leads to dissipation, even in the Meissner phase. In principle, this also makes it hard to define a critical current j_c, as the onset of dissipation is more gradual, although experimental tests of this behaviour are difficult due to the resistivity vanishing exponentially with current density j.

Extensive theoretical work was also done by Giamarchi *et al.*, developing a description of the statics. In their phase diagram they distinguish a low magnetic field quasi-ordered vortex lattice phase (Bragg glass phase) and a high magnetic field disordered vortex glass phase [234]. Whilst their theory does not portray the dynamics, through dimensional considerations they arrive at the same voltage-current dependence as FFH [235]. An experimental test for the Bragg glass phase that their theory offers is the power-law decay of the crystalline order as a function of magnetic field. Such a signature was later found by neutron diffraction for the BCS superconductor (K,Ba)BiO_3 [236].

Another theoretical treatment of a transition to finite resistivity, that has been applied to the cuprates before [237–240], is provided by the Berezinskii–Kosterlitz–Thouless (BKT) model. While the BKT model is only for two-dimensional systems, and YBCO has a sizeable coupling in the out-of-plane direction, the form of the BKT transition appears to be relevant to YBCO. The BKT transition is understood in the context of vortex generation through unbinding of vortex-antivortex pairs, with the vortex generation having a power law correlation with temperature. We note some further limitations, namely that it does not take disorder into account, and most of its results only apply in the zero current limit. These makes the FFH theory the more appropriate theory for the cuprates. It is still useful to apply the results of the BKT theory to our data, so that we can draw comparisons with earlier papers on the cuprates employing BKT, and enables us to explore the connections between the two theories.

For a BKT transition the $j \to 0$ limit a non-linear voltage-current dependence is found [241] to be of the form

$$V \propto j^{\alpha(T)} \tag{6.3}$$

with the exponent $\alpha(T)$ decreasing with increasing temperature, reaching a value of 3 at the BKT transition at T_{BKT}, and then dropping to a value of 1 for higher temperatures. T_{BKT} corresponds to the critical temperature where the correlation length is meant to diverge to infinity [242], similar to the FFH model, but its connection to $\alpha(T) = 3$ is only empirical. The

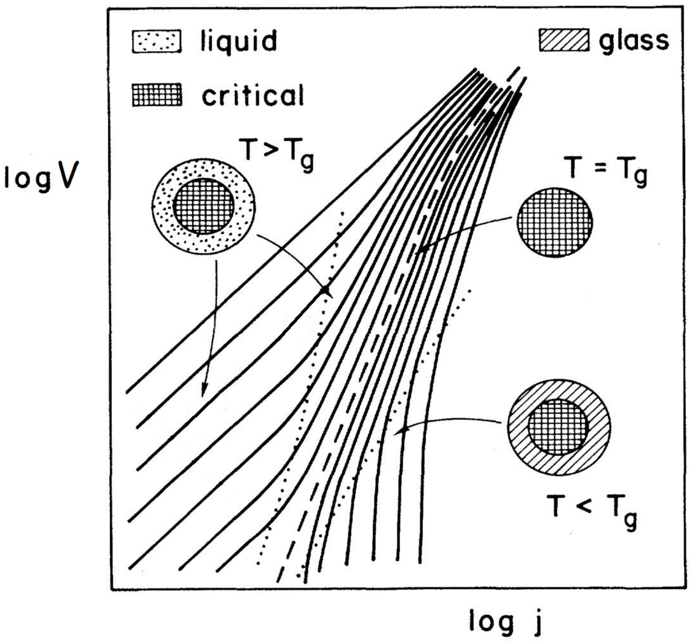

Fig. 6.17 Schematic voltage-current dependence of a superconductor in the mixed state with each line corresponding to different isotherms. The high-current, high-voltage regime is characterised by linear I-V due to superfluid breakdown. For lower voltages we see two regimes emerge. At low temperatures and intermediate currents the I-V curves show negative curvature that are well-described by Fisher-Fisher-Huse (FFH) scaling of the form $V \propto j\exp[-(j_T/j)^{\mu}]$, and at higher temperatures and low currents the I-V curves show positive curvature, with an initially steeper than linear dependence, and a linear I-V tail at the lowest currents. The two regimes are separated by the dashed line that corresponds to a phase transition at a characteristic temperature T_g, where $V \propto j^{\alpha(T)}$ (with $\alpha(T_{\mathrm{BKT}}) = 3$ in the case of the BKT model). The critical region refers to regions in the critical state with $j = j_c$. Adapted from Ref. [246].

linear resistivity obtained from the correlation length is [243–245]

$$\rho \propto \exp[-z\sqrt{b/(T/T_{\mathrm{BKT}}-1)}] \tag{6.4}$$

where z is a critical exponent related to $\alpha(T_{\mathrm{BKT}})$ and b is a fitting parameter. This equation predicts zero resistivity below the characteristic temperature due to the divergent correlation length, in a similar fashion to Eq. 6.1. We note that the BKT model does not take disorder into account.

As a first port of call, we employ the FFH model to interpret our transport measurements, as it offers the most complete description of the voltage-current dependence in the mixed state.

A schematic of the log-log voltage-current dependence for different isotherms is shown in Fig. 6.17. T_g marks the characteristic temperature below which true superconductivity (with zero resistivity) is predicted to appear. We highlight several I-V regimes. For all isotherms, high currents lead to superfluid breakdown, and therefore linear I-V (top-right region). As the temperature is lowered the I-V curves become steeper, which corresponds to an increase in the exponent μ in the FFH I-V equation (Eq. 6.2). For temperatures above T_g the curves retain a positive curvature due to the ohmic region at low voltages (bottom-left region), which could be explained by plastic barriers as detailed for thermally assisted flux flow [246], or by finite-size effects as lower currents probe larger length scales (which can become comparable to the large penetration depth of cuprates [242]). For temperatures below T_g the curves show a negative curvature for all currents, with the voltage becoming exponentially small with decreasing current.

The criterion for identifying the critical temperature from the voltage-current dependence is not yet conclusively established. One proposed criterion is of the concavity of the I-V curves, with the characteristic temperature defined for the isotherm where the curvature of the I-V curves goes from positive to negative [242]. This is an obvious definition, as it seeks the temperature for which exponential decay of the voltage is realised, unhampered by flux flow or finite-size effects. This also makes it difficult to apply with certainty, as it requires high voltage resolution.

Here, we propose a criterion that applies the FFH equation $V \propto j\exp[-(j_T/j)^{\mu}]$ to determine the characteristic temperature for a set of I-V isotherms. Fig. 6.18 shows such sets of isotherms for $YBa_2Cu_3O_{6.55}$ (hole doping of $p = 0.108$), measured at very high magnetic fields and low temperatures. Previous I-V measurements were limited to a magnetic field of 6 T or lower [247]. At 45 T most of the isotherms show linear I-V with a non-ohmic dependence seen only for 0.04 K. As we go lower in field we see an increased fanning of the isotherms, with non-ohmic isotherms constituting the majority. We do not see any signatures of finite-size effects. We fit to these isotherms using the FFH equation (fits shown in the insets by solid lines) to determine the exponent μ as a function of temperature at different magnetic fields. We plot the results in Fig. 6.18f. We define the characteristic temperature T_{FFH} as the temperature when

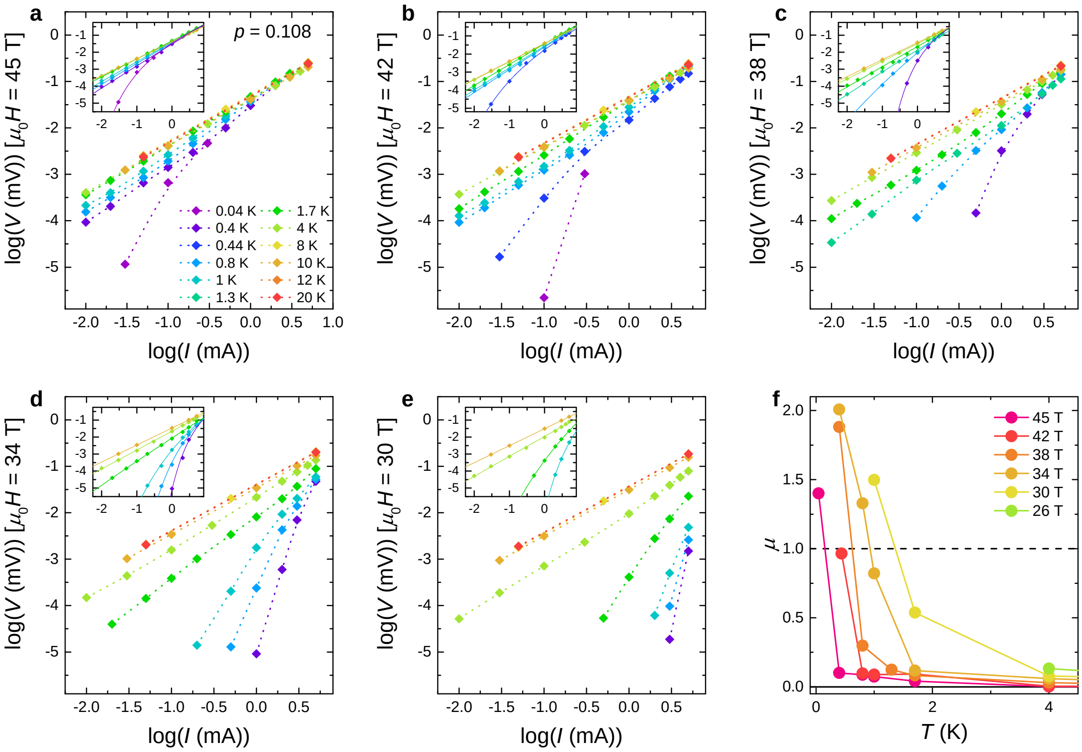

Fig. 6.18 Fitting with the FFH model. (a-e) Non-ohmic voltage-current dependence of $YBa_2Cu_3O_{6.55}$ (hole doping of $p = 0.108$) at five different magnetic fields between temperatures of 0.04 and 20 K. We see an increase in the gradient of the logarithmic I-V curves with decreasing temperature at all magnetic fields, with the behaviour becoming more dramatic at lower magnetic fields. We perform fits as shown in the insets based on the FFH model [16], which describes the non-ohmic voltage-current dependence to follow $V \propto j\exp[-(j_T/j)^{\mu}]$, where j is the current density, and j_T and μ are fitting parameters. (f) The exponent μ as a function of temperature for different magnetic fields. We define the characteristic temperature T_{FFH} as the temperature when $\mu = 1$.

$\mu = 1$. We note that we find μ to be greater than 1 for the lowest temperature curves, even though the FFH model limits $\mu \leq 1$, with $\mu = 1$ in the Meissner phase. We clearly find that our lower temperature isotherms decay even more dramatically than as is expected in the Meissner phase, but it is not clear how this could be interpreted within the frameworks of the theory. We identify studies performed at low magnetic fields on $YBa_2Cu_3O_{6+x}$ thin films [248] and LBCO single crystals [240] that also have isotherms with μ greater than one.

There is also a criterion associated with the BKT theory with T_{BKT} defined as the temperature where the exponent $\alpha(T_{\mathrm{BKT}}) = 3$. Theoretically, α should jump from a value of 1 to

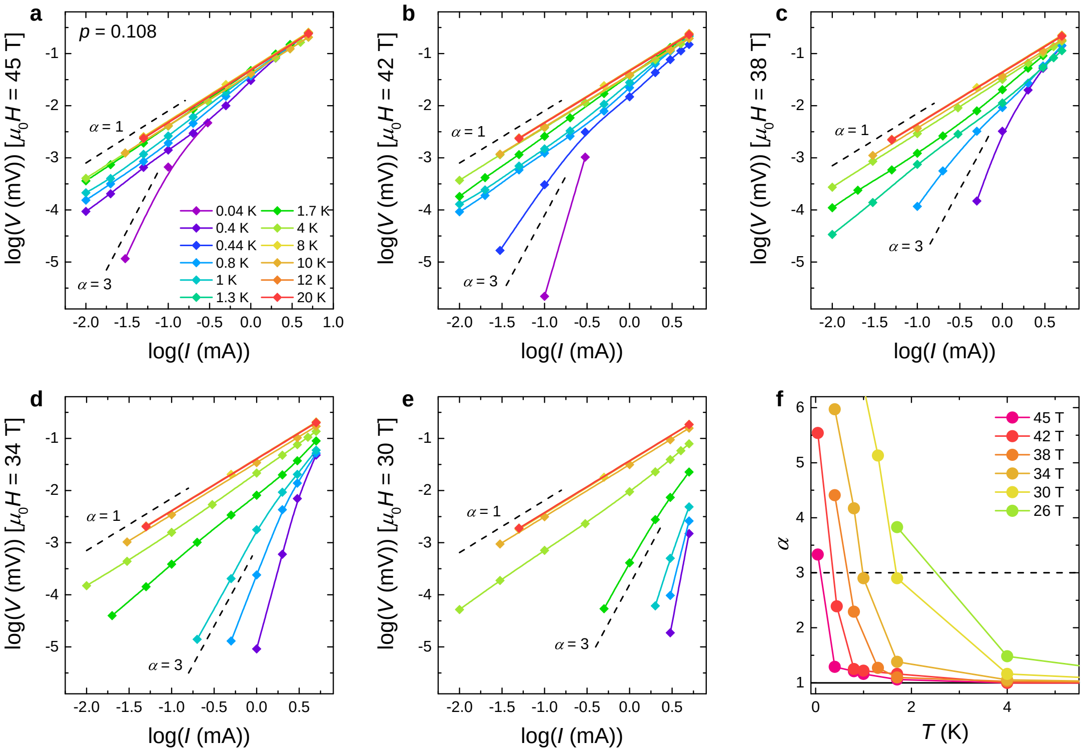

Fig. 6.19 Fitting with the BKT model. (a-e) Non-ohmic voltage-current dependence of $YBa_2Cu_3O_{6.55}$ (hole doping of $p = 0.108$) at five different magnetic fields between temperatures of 0.04 and 20 K. We see an increase in the I-V curve gradients with decreasing temperature, that corresponds to an increase in the exponent α in the power law equation $V \propto I^{\alpha(T)}$. (f) The exponent α as a function of temperature for different magnetic fields. The characteristic temperature T_{BKT} is defined such that $\alpha(T_{\mathrm{BKT}}) = 3$.

3 at T_{BKT}, coinciding with a jump in the superconducting electron density, but most experiments previously found broad transitions [242, 244, 245, 249–251, 240, 252–254], making their acceptance as being BKT transitions not universal [249, 250]. It is important to stress here that the BKT power law only applies in the $j \to 0$ limit, and therefore broadening of the transition is expected for finite current densities. This can be seen in Fig. 6.17, showing that the increase in gradient with decreasing temperature is more gradual for higher voltages. It raises an important point, in that the BKT power law can only be fitted to a small section of each I-V curve, and the analysis again benefits from datasets with high voltage resolution. However, it is has been raised that the presence of finite-size effects could distort the true characteristic

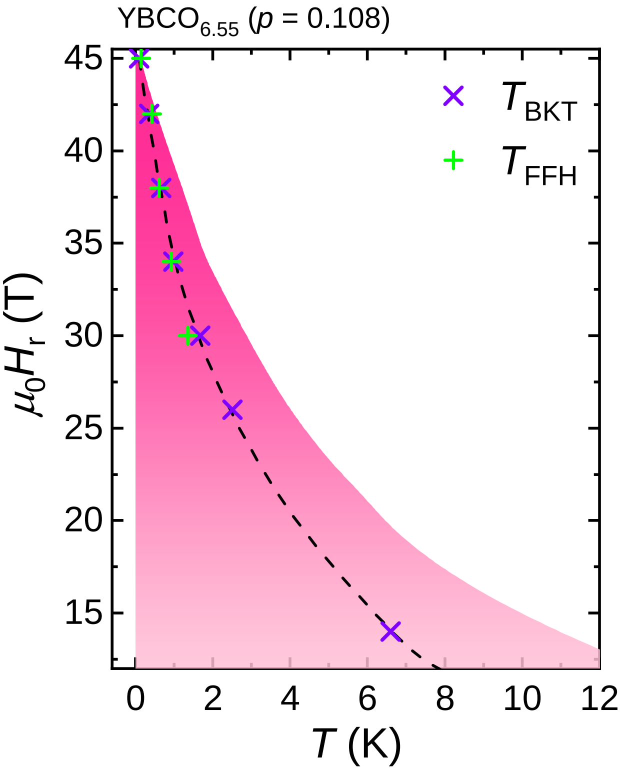

Fig. 6.20 The characteristic temperatures T_{BKT} and T_{FFH} (highlighted by the dashed line) obtained from the voltage-current dependence presented in Figs. 6.19, 6.18 and 6.21, overlayed with the onset field of finite electrical resistivity (red outline). We find good correspondence between the characteristic temperatures obtained from the BKT and FFH analyses.

temperature [242, 249], and therefore it might be better to fit to the steepest part of the curve, as opposed to the lowest current section, even if it leads to a broader transition.

To put our results in context, we fit with the BKT power law on the same dataset (Fig. 6.19) as the FFH equation. We find the exponent α for the steepest part of each I-V curve (which also corresponds to the lowest currents), and plot it as a function of temperature for each magnetic field in Fig. 6.19f. We find that α increases sharply with decreasing temperature, reaching a value of 3 and higher for most magnetic fields. We use this plot to find the value of T_{BKT} (where $\alpha = 3$) for each field value. We plot these together with the values found for T_{FFH} on the same phase diagram (see Fig. 6.20). We find a good agreement between the two characteristic temperatures, with a sharp upturn with increasing magnetic field at

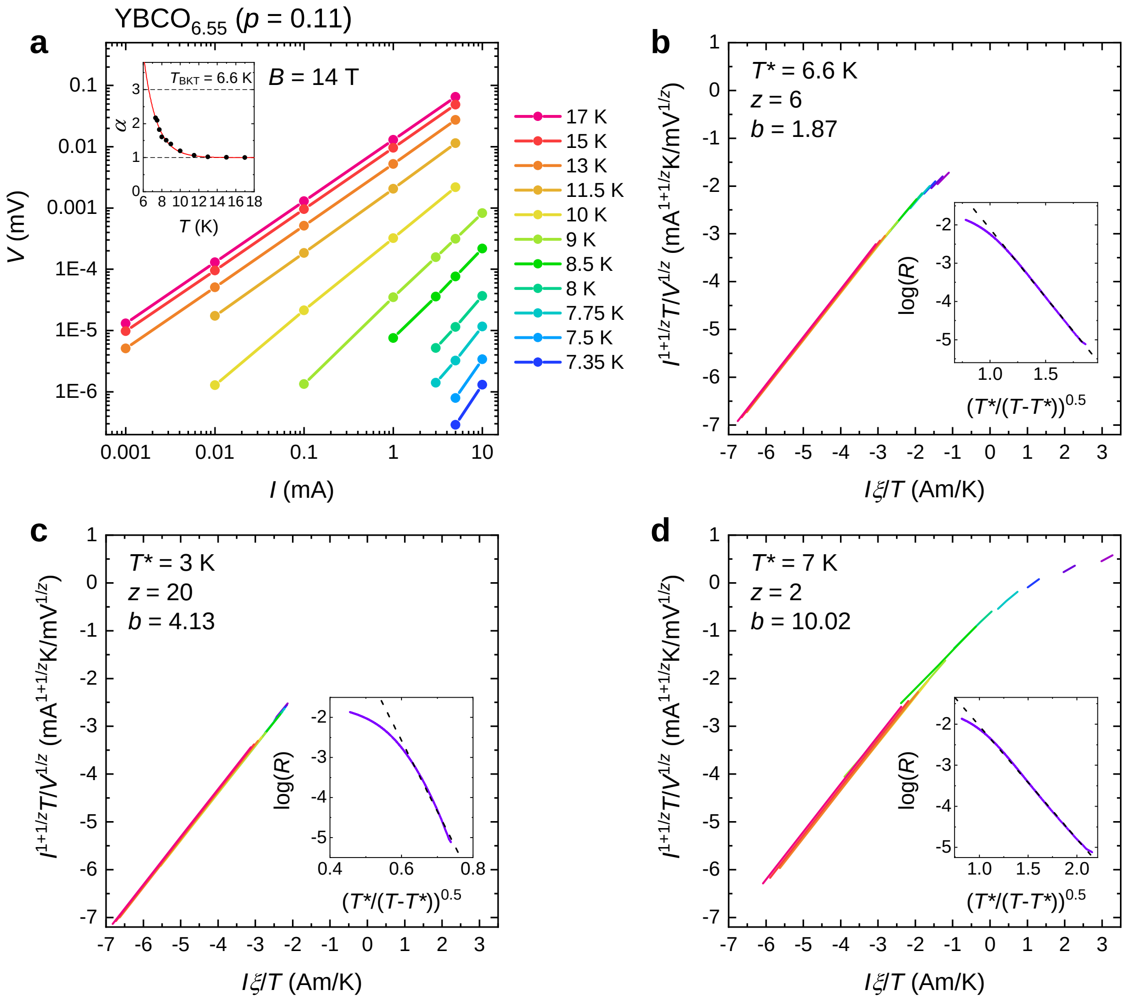

Fig. 6.21 (a) The voltage-current dependence of $YBa_2Cu_3O_{6.55}$ as a function of temperature at an applied magnetic field of 14 T. (b-d) The same voltage-current isotherms after scaling collapses using dynamic scaling [17, 249, 242] for various T^* values. The insets show temperature sweeps of the resistivity ($I = 1$ mA) with gradient fitting to determine b, one of the scaling parameters. The third scaling parameter z is chosen so that the best collapse is achieved. A good collapse is found for all three T^* values, resulting in different z values.

low temperature, similar to the onset field of finite electrical resistivity, but lying within the boundary defined by $I = 10$ μA. Our analyses of the voltage-current dependence demonstrates the existence of a true superconducting phase (with zero resistivity) that persists up to at least 45 T in $YBa_2Cu_3O_{6.55}$.

With the agreement we identify between the characteristic temperatures, it becomes interesting to explore the connections between the BKT and FFH models. Ref. [242] showed that the two theories are analytically incompatible; namely, the BKT model results in an exponent that is only a function of temperature ($\alpha(T)$), whereas the FFH model finds that it is also a function of current ($\alpha(j,T)$). This point is also demonstrated by experiments, as the FFH equation is able to describe the voltage-current dependence for a wide range of currents and voltages, whereas the BKT power law only applies to a limited regime. A more obvious connection is present in the dynamic scaling analysis [17, 242, 249], which has been applied to investigate critical transitions of superconductors, superfluids and Josephson junction arrays [249]. It relies on results of the FFH theory, which relate a specific ratio of the current and voltage to the correlation length ξ for all I-V curves. It is the BKT correlation length which is then substituted in, combining the results of the two theories. The final relation [249]

$$\frac{I}{T}\left(\frac{I}{V}\right)^{1/z} = \frac{I\xi/T}{\chi_{\pm}^{1/z}(I\xi/T)} \tag{6.5}$$

where $\chi_{+(-)}(x)$ is the scaling function for temperatures above (below) the critical temperature T^*, allows us to plot $I^{1+1/z}/TV^{1/z}$ vs. $I\xi/T$. This relation should make all isotherms lie on the same curve for suitable values of T^* and z (related to the critical exponent $\alpha(T^*)$). The dynamic scaling analysis has been an alternative to the BKT power law fit for finding T^* and z, as it should hold for finite currents, and not just in the $j \to 0$ limit [242, 249].

We perform the dynamic scaling analysis for a set of I-V curves at 14 T, a magnetic field at which we also measured temperature sweeps. Using the BKT analysis, we find $T_{\mathrm{BKT}} = 6.6$ K (Fig. 6.21a). With this value we fit to the temperature sweep of the resistivity ($I = 1$ mA) using the BKT temperature dependence (Eq. 6.4, with the fit shown in the inset of Fig. 6.21b) to find a value for b as a function of z, which are two of the inputs for the scaling analysis. The other variable is T^*, which we set to 6.6 K in the first instance, and we vary z until we arrive at the best collapse for all the isotherms. Finally, for a characteristic temperature of 6.6 K we find $z = 6$. The success of this scaling analysis indicates the applicability of one of the main results of the FFH theory to describe the observed non-ohmic voltage-current dependence.

Extensive discussion exists in the literature about the value of z [242, 249]. The expectation for a 2D system is $z = 2$, but measurements on the cuprates yielded values of around 5-

6 [245, 249], which would be characteristic of a 3D system. Our value for z is in line with these results. Ref. [242] argued that dynamic scaling is too flexible, and can produce a good collapse for a range of values of T^* and z. We find this to be true if one allows T_{BKT} to be variable when performing the analysis. We find good collapses for our data when setting $T^* = 3$ K and $z = 20$ (Fig. 6.21c), and also for $T^* = 7$ K and $z = 2$ (Fig. 6.21d). However, we believe this is not proof that dynamic scaling is too flexible, but rather highlights that the analysis should be applied for known values of T^*, obtained by other methods, such as the criteria we detailed above.

Lastly, we examine the applicability of the expressions for the linear resistivity as obtained by the FFH and BKT theories (Eqs. 6.1 and 6.4 detailed earlier). Both expressions are derived from the correlation length that is predicted to diverge at the characteristic temperature, and in turn results in zero linear resistivity below the transition. In an ideal scenario, we could apply these expressions of the measured resistivity in the zero current limit, however experimentally we are limited to finite currents. We perform our analysis on the temperature sweep performed at 14 T and a measurement current of $I = 5$ mA, as it tracks the transition in resistivity over 6 orders of magnitude. Fig. 6.22a shows the fit with the FFH equation, following the analysis presented in Ref. [247] (and was cited as an experimental validation of their theory in Huse, Fisher, & Fisher [16]). We find that the fit describes the measured resistivity near the characteristic temperature well. We find an exponent of $s = 7.3$, comparable to $s = 6.5$ found in Ref. [247], and would correspond to $z = 4.7$. This is somewhat lower than our dynamical scaling result, and is likely due to the finite current. For lower currents we would expect a steeper transition, and therefore a larger exponent. Fig. 6.22b shows the fit with the BKT equation. We find good agreement with the measured curve over five orders of magnitude in resistivity. The characteristic temperatures we obtain from the two fits are somewhat lower ($T_{\mathrm{g}} = 6.3$ K and $T_{\mathrm{BKT}} = 6.0$ K) than we found from the I-V dependence ($T_{\mathrm{BKT}} = 6.6$ K). This is again likely to be due to the finite current. Importantly, we find that the results of both the FFH and BKT theories provide an appropriate description of the measured temperature dependence of the resistivity, predicting the exponential decay near the characteristic temperature, and the vanishing of the resistivity. This is in addition to their applicability to the measured voltage-

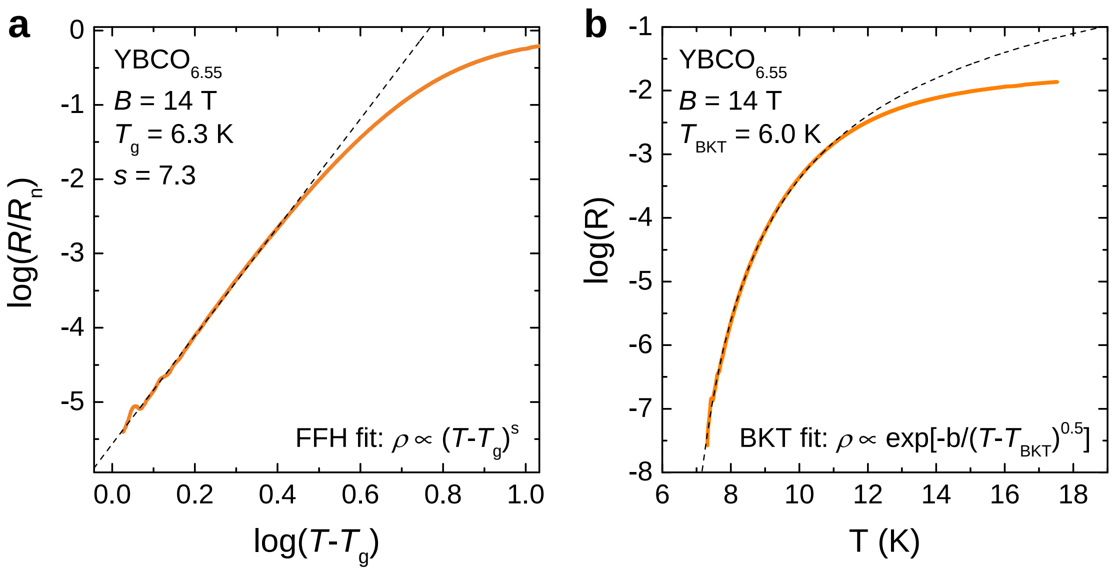

Fig. 6.22 The measured resistivity ($I = 5$ mA) as a function of temperature (orange line), compared to the predicted resistivity (a) by the FFH model [16, 247] (dashed lines), (b) and the BKT model [242]. We find good agreement in both cases, and characteristic temperatures comparable to that was identified from the voltage-current dependence.

current dependence. We note that the Kim-Anderson model, that predicts zero resistivity only at zero temperature, fails to describe our data.

The theories considered here are limited to classical fluctuations, but for a complete description theoretical frameworks that account for quantum fluctuations should be sought. One such theory is presented by Ref. [255], proposing the emergence of a new kind of vortex phase at high magnetic fields (dubbed supersolid quantum vortex crystal or gauge glass phase), which would be expected to be bounded by a vortex glass transition. Its relevance to our system is further indicated by the intermediate value of the predicted supersolid crossover field, which we estimate to be $B_x \approx 15$ T (using an anisotropy of $\gamma \approx 1/20$ [256, 257]).

In this section we set out to determine the extent of true superconductivity (with zero resistivity). With our investigation of the measured I-V curves, we were able to identify a line of characteristic temperatures, which is current-independent, and satisfies the criteria for zero resistivity superconductivity as set out by Fisher, Fisher, and Huse's theory for vortex matter. Whilst a complete theoretical understanding of the ground state of underdoped cuprates is still out of reach, the complex state we find does negate any conventional Fermi liquid picture. Our measurements reveal exciting new findings that shed light on the pseudogap ground state, including a high-field superconducting region of the phase diagram, where the effects of vortex dynamics and fluctuations are enhanced, and is also host to quantum oscillations.

6.6 Superconductivity, the pseudogap, and quantum oscillations

We focus our attention on the unexpected aspect of our results that quantum oscillations are found to occur well within the superconducting regime. This could not be more apparent than in our magnetic torque measurements, that show a bulk hysteresis due to vortex pinning up to at least 45 T, with quantum oscillations visible on top of the hysteretic torque background (Fig. 6.23a). Our resistivity measurements revealed a phase boundary at low temperatures and high magnetic fields, where the vortex liquid state terminates and leads to a state with pinned vortices. We call this state, in the high-magnetic field/low-temperature limit that has not been accessed before, the quantum vortex matter state [258]. This is to highlight the relevance of quantum fluctuations to this state, which was pointed out by Ref. [17]. We present measurements of quantum oscillations on either side of this phase boundary (Fig. 6.23b). We find the amplitude of the quantum oscillations to be the same in both regimes ($T = 0.04$ and 1.0 K), with no additional damping in the pinned vortex state (quantum vortex matter state), contrary to what is predicted by models of spatially uniform superconductivity. We also find quantum oscillations in the electrical resistivity on applying larger currents that lead to vortex dissipation, occurring for the same field range where lower currents lead to zero resistivity (Fig. 6.23c). Indeed, we find Shubnikov–de Haas oscillations are also exhibited in our contactless resistivity measurements, persisting down to at least 20 T (Fig. 6.23b), the same magnetic field where de Haas–van Alphen oscillations emerge (Fig. 6.23d). These results confirm that the observed quantum oscillations are a fundamental feature of the high magnetic field/low-temperature regime, and are found to coexist with superconductivity. Our results are contrary to the previously held view that quantum oscillations are a property of the normal state, and necessitate a new description within the framework of the superconducting vortex state. The unconventional nature of the quantum oscillations is further highlighted when we consider that the typical condition for quantum oscillations to be viable in a type-II superconductor is that $\hbar\omega_c/\Delta \gtrsim 1$ [26] (where $\omega_c = e\mu_0 H/m^*$ is the cyclotron frequency, and Δ is the superconducting gap). With $\Delta = 20 - 30$ meV [259–262], $m^* = 1.6\ m_e$ [203], and $\mu_0 H = 20$ T, the lowest field with quantum oscillations, we find the ratio to be $0.05 - 0.08$, much smaller than unity. In other words, what we find is that for such a large superconducting gap in $YBa_2Cu_3O_{6.55}$ the quantum oscillations appear at an inexplicably low magnetic field.

We look for clues of a new description by considering the absolute size of the measured quantum oscillations, and whether any deviations from the Lifshitz–Kosevich theory are revealed. First, we show that the amplitude of the de Haas–van Alphen oscillations is consistent with the assumption that the entire bulk of the sample contributes to the observed quantum oscillations. We do this by performing the conversion of the quantum oscillations' amplitude into absolute units and then compare to the Lifshitz–Kosevich estimate, similar to the analysis we applied in the case of SmB_6 and YbB_{12} in earlier chapters. The inset to Fig. 6.24 shows the measured magnetic torque in units of capacitance. The magnitude of the magnetic torque is given by $\tau = |\mathbf{m} \times \mu_0 \mathbf{H}| \equiv m\mu_0 H \sin\theta$, where $m \equiv |\mathbf{m}|$ is the magnitude of the magnetic moment, $\mu_0 H = |\mu_0 \mathbf{H}|$ is the magnitude of the magnetic field and $\theta \approx 9^\circ$ is the angle of inclination relative to the c-axis. Such an inclination away from the c-axis leads to an increase in H_{irr} of only 1%, as H_{irr} transforms as $H_{\text{irr}}(\theta) = H_{\text{irr}}(\theta = 0^\circ)/\cos\theta$ for small angles. We convert the measured capacitive torque to absolute units of magnetic moment per unit cell by using the spring constant of the cantilever as detailed in Ref. [29]. We have cantilever length $L = 3.8$ mm, distance between cantilever and fixed Cu plate $d_0 = 0.1$ mm, spring constant $k = 5\ \text{N} \cdot \text{m}^{-1}$, unit cell volume $V_{\text{u.c.}} = 0.383 \cdot 0.387 \cdot 1.174\ \text{nm}^3$, and crystal volume $s^3 = 0.15\ \text{mm}^3$. Thus, we convert the measured torque magnetisation in terms of capacitance (C) to an absolute magnetic moment $m_\perp$ in units of Bohr magnetons per unit cell by the expression:

$$\Delta m_\perp = 0.24\ \text{TpF}^{-1}\ \frac{\Delta C}{\mu_0 H} \quad \mu_B \text{ per unit cell.} \tag{6.6}$$

The measured quantum oscillatory magnetic moment in absolute units is shown in Fig. 6.24.

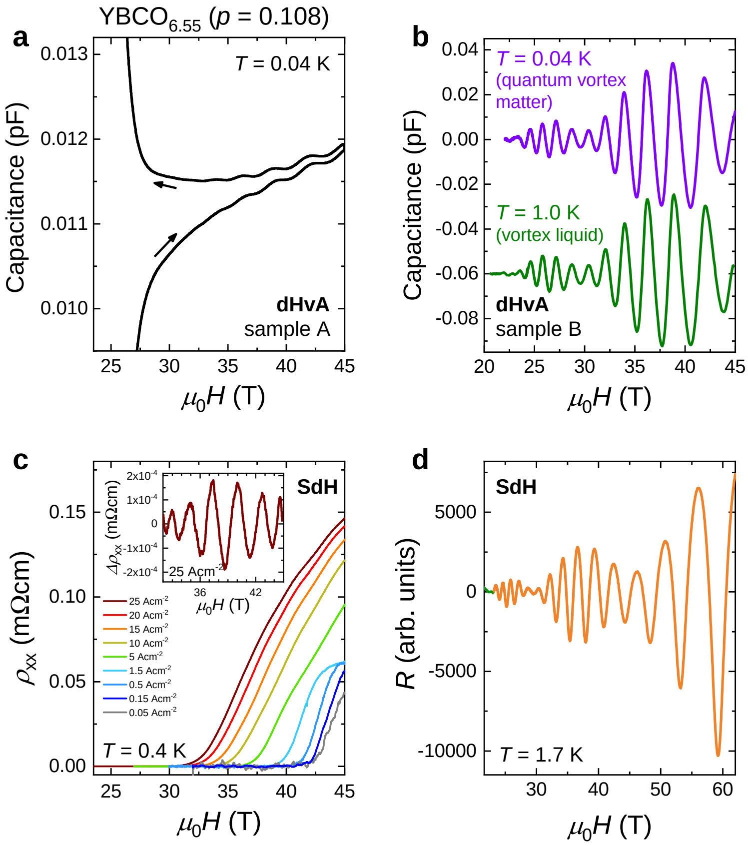

Fig. 6.23 Bulk superconductivity as established by bulk torque hysteresis (Fig. 6.15) and synonymous zero electrical resistivity up to the highest magnetic fields (Fig. 6.11), is found to coexist with quantum oscillations observed in both magnetic torque and electrical resistivity down to magnetic fields as low as 20 T. (a) Torque hysteresis persisting up to at least 45 T, with concurrent de Haas–van Alphen oscillations visible on top of the background. (b) De Haas–van Alphen oscillations observable from magnetic fields as low as 20 T, both below the vortex liquid–vortex solid transition ($T = 0.04$ K), and above ($T = 1.0$ K). No additional damping is observed inside the quantum vortex matter state. (c) The electrical resistivity for different measurement currents reveals Shubnikov–de Haas oscillations in the same region of magnetic fields, where zero electrical resistivity is observed for smaller measurement currents that do not cause vortex dissipation. (d) Shubnikov–de Haas oscillations were also observed in contactless resistivity from magnetic fields as low as 20 T. At a temperature of 1.7 K the onset magnetic field of finite resistivity was found to be 34 T.

We estimate the theoretical amplitude of the intrinsic quantum oscillatory magnetic moment using the formula for a two-dimensional Fermi surface as detailed in Chapter 2:

$$D_{2\mathrm{D}} = \frac{4m_e}{m^*}\left(\frac{k_\mathrm{F}}{k_\mathrm{BZ}}\right)^2 \sin\theta, \tag{6.7}$$

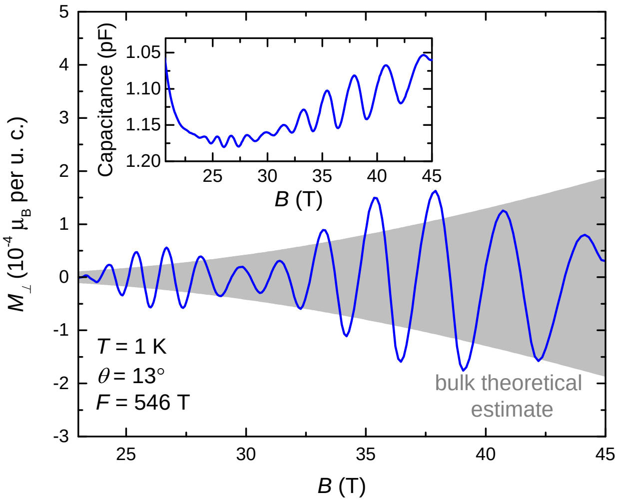

Fig. 6.24 De Haas–van Alphen oscillations in absolute units of magnetic moment (μ_B per unit cell) corresponding to the $F = 546$ T oscillations in $YBa_2Cu_3O_{6.55}$. The shaded region represents the theoretical Lifshitz–Kosevich estimate of the magnetic moment corresponding to the measured oscillations assuming a bulk origin, showing a good order-of-magnitude agreement with the absolute amplitude of the measured quantum oscillations.

where $k_{BZ} = 2\pi/a_{u.c.}$, $a_{u.c.}$ is the lattice constant, k_F is the Fermi wavevector, m^* is the effective mass, and θ is the angle between the applied magnetic field and the c-axis of the sample. We also take into account the impurity damping term $R_D = \exp(-B_0/B)$, where B_0 is the damping factor. The resulting estimate for the theoretical amplitude, using the values $m^* = 1.6m_e$, $k_F = 1.29 \cdot 10^9$ m^{-1}, $\theta = 9°$, $B_0 = 130$ T, is shown by the shaded envelope in Fig. 6.24. With these results, we find a good order of magnitude agreement between the absolute amplitude of quantum oscillations and the theoretical Lifshitz-Kosevich expectation, indicating the bulk nature of the observed quantum oscillations. We also note that quantum oscillations have been observed up to 100 T [263, 204], with no dramatic enhancement in quantum oscillation amplitude as a function of magnetic field, which suggests that the regime accessed by DC fields extends as high as 100 T, with no evidence for a transition into a conventional metallic normal state.

Next, we look for any deviation from the Lifshitz–Kosevich theory. We consider our measurements performed at $\theta = 36°$, where the quantum oscillations are composed of a single

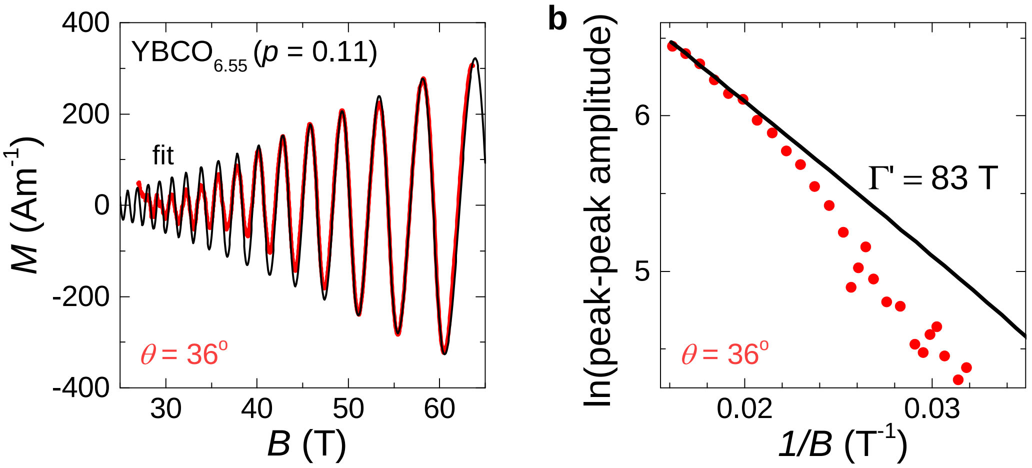

Fig. 6.25 (a) De Haas–van Alphen oscillations inferred from torque magnetisation measurements performed in pulsed magnetic fields at a field orientation with a single oscillation frequency and no beat pattern. The red line denotes the measured oscillations, whereas the black represents a fit to the 50 to 60 T field range. We see that the measured oscillations are damped more than expected based on the Lifshitz–Kosevich fit. (b) The plot of the peak-to-peak amplitude of the oscillations as a function of inverse magnetic field. The black line denotes the expected damping for a damping factor of $\Gamma' = 83$ T, but we find the measured amplitude to increasingly deviate from the expected damping with decreasing magnetic field.

frequency. We fit with the Lifshitz–Kosevich equation (see Chapter 2) using a damping factor of $\Gamma' = 83$ T (shown by the black line in Fig. 6.25a). There is a good agreement in the higher magnetic field range, but there appears to be additional damping below 50 T, where the amplitude of the measured quantum oscillations is smaller than that of the fit. We highlight this additional damping by plotting the peak-to-peak amplitude as a function of the inverse magnetic field together with the damping expected for a damping factor of $\Gamma' = 83$ T. By 30 T the additional attenuation of the amplitude would correspond to an increase in the damping factor of ≈ 70 T. This behaviour is reminiscent of quantum oscillations that were observed deep in the vortex state of various type-II superconductors, that exhibit extra attenuation, but no change in the frequency of the oscillations [26]. For some of the materials quantum oscillations were observed down to magnetic fields as low as 20% of the upper critical field $\mu_0 H_{c2}$ [264–266]. The central idea of microscopic theories applied to vortex state quantum oscillations in more conventional superconductors is relating the attenuation of quantum oscillations to the superconducting gap, which opens up at the upper critical field $\mu_0 H_{c2}$ and grows with decreasing magnetic field [26, 264]. With anisotropic superconducting gaps, this also provides an explanation for why frequencies originating from different parts of the Brillouin zone characterised by different gap sizes can exhibit varying amounts of attenuation [265, 266]. Models that have been shown to effectively describe the measured attenuation inside the vortex state include the Maki [267], Miyake [268], and Yasui-Kita [269] models, with the main difference in their predicted form of the magnetic field dependence of the attenuation. They have also been used to estimate the superconducting gap [264–266, 269]. Without any experimental indication of $\mu_0 H_{c2}$ it is uncertain what would be the right description and if any of these theories could be be applied to $YBa_2Cu_3O_{6+x}$.

Nevertheless, we explore what the ratio $\hbar\omega_c/\Delta$ is for type-II superconductors that exhibit quantum oscillations in the vortex state. A summary of the ratios and values used for these estimates is shown in Table 6.1 for ten different superconductors and $YBa_2Cu_3O_{6.55}$. Note that the superconducting gap values are much smaller for the type-II superconductors than for $YBa_2Cu_3O_{6.55}$, which also coincides with quantum oscillations observed at relatively modest magnetic fields in these materials. For most of them we find the ratio $\hbar\omega_c/\Delta$ to be ≈ 0.5, which is not that much lower than the criterion of ≥ 1 for conventional quantum oscillations. The exceptions are the unconventional superconductors: $YBa_2Cu_3O_{6.55}$, the organic layered superconductor κ-(BEDT-TTF)$_2$Cu(NCS)$_2$ and the two heavy-fermion uranium systems, with the corresponding ratios found to be significantly smaller than unity. Thus, a strong link between the anisotropic Fermi surface of $YBa_2Cu_3O_{6.55}$ and the anisotropic gapping of its Brillouin zone is indicated, which again highlights the influence of the pseudogap on the ground state. With strong gapping in the antinodal regions, quantum oscillations originating from any corresponding Fermi surface sheets are not expected to survive into the vortex state, whereas the nodal region is found to be characterised by no gapping, which allows quantum oscillations to persist deep into the vortex state. Our findings suggest theoretical descriptions that can yield a partially gapped Fermi surface and lines of gapless excitations. Pertinent theories involve the interplay of superconductivity and charge order, such as biaxial charge density wave [203] or pair density wave [216, 270, 271]. The pair density wave description has also been proposed to yield a steep slope of the superconducting magnetic field–temperature phase boundary [272], as observed in our experiments.

Compound	T_c (K)	$\mu_0 H_{50\%}$ (T)	$\mu_0 H_{c2}$ (T)	m^* (m_e)	Δ (meV)	$\hbar\omega_c/\Delta$
$NbSe_2$ [264, 273]	7.2	2.3	8.0	0.61	1.2	0.4
V_3Si [264, 274, 275]	17	17.2	18.5	1.3	2.6	0.6
Nb_3Sn [274, 275]	18.3	14.4	19.7	1.1	3.2	0.5
YNi_2B_2C [265, 276]	15.6	3.9	8.8	0.35	2.7	0.5
$LuNi_2B_2C$ [266, 277]	16.5	3.6	7.5	0.3	2.2	0.6
MgB_2 [278]	38.5	9.0	9.6	0.46	2.5	0.9
$CeRu_2$ [279, 280]	6.2	3.6	5.2	0.55	1.3	0.6
UPd_2Al_3 [281–283]	2	3.6	3.8	5.7	0.24	0.3
URu_2Si_2 (*ab*-plane) [284–286]	1.5	7.2	10.4	9.5	0.7	0.13
URu_2Si_2 (*c*-axis) [284–286]	1.5	2.8	2.9	13	0.3	0.08
κ-(BEDT-TTF) [287–289]	10.4	4.5	6.0	3.5	3	0.05
$YBa_2Cu_3O_{6.55}$ [203, 259–262]	61	20^*	> 100 T	1.6	$20 - 30$	$0.05 - 0.08$

Table 6.1 Different parameters for superconductors that display quantum oscillations in the superconducting regime, including the critical temperature T_c, magnetic field where superconducting damping reduces the quantum oscillation amplitude by half $\mu_0 H_{50\%}$, the upper critical field $\mu_0 H_{c2}$, the effective mass m^*, and the superconducting gap Δ at zero magnetic field. These values are used to determine the ratio of the Landau level spacing to the superconducting gap. For all materials, with the exception of $NbSe_2$ and MgB_2, the quantum oscillations were measured for the field orientation with the lowest upper critical field. In the case of $YBa_2Cu_3O_{6.55}$ * represents the lowest magnetic field value at which oscillations are observed, giving an upper bound estimate for the Landau level to superconducting gap ratio. The absence of any dramatic enhancement of the quantum oscillation amplitude up to 100 T indicates an upper critical field beyond what has been experimentally accessible.

Chapter 7

Conclusion

This thesis studied the magnetic, electrical and thermal properties of Kondo insulators SmB_6 and YbB_{12} and high-T_c superconductor $YBa_2Cu_3O_{6+x}$ in high magnetic fields. We demonstrated that both classes of materials display quantum oscillations in the absence of a Fermi liquid state, going against the long-held association of quantum oscillations exclusively with metals. Previous descriptions proved to be ineffective in accounting for the breadth of experimental results we presented, highlighting the need for new theoretical paradigms, some of which we indicated. In this chapter, we review these results, and suggest directions for future work.

7.1 Bulk Fermi surfaces in Kondo insulators

Quantum oscillations have been the hallmark signature of metals ever since they were observed in copper, which is why the discovery of a Fermi surface in Kondo insulating SmB_6 [10] was so puzzling. The quantum oscillations in SmB_6 revealed frequencies ranging up to 15 kT with light effective masses, similar to what has been observed for metallic hexaborides [74] and indicative of a large ellipsoidal Fermi surface (see Fig. 7.1) [10]. There were proposals that the quantum oscillations could be from topological surface states [9], or have an extrinsic origin [121]. The quantum oscillation measurements presented here, however, represent strong evidence for their bulk origin. Through careful experimental control and calibration, in addition to comparative measurements of metallic LaB_6, we established that the absolute size of the oscillations in

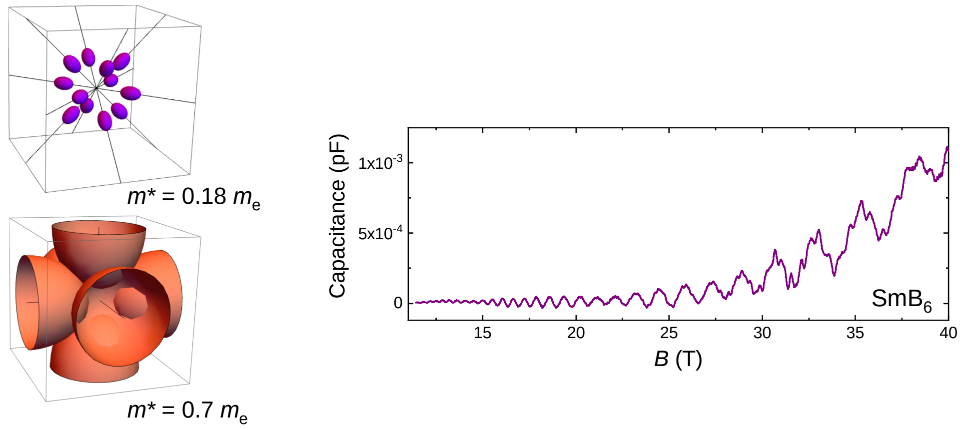

Fig. 7.1 The metal-like Fermi surface inferred from quantum oscillation measurements of SmB_6.

SmB_6 is the same as for metallic LaB_6, and in good agreement with the Lifshitz–Kosevich model. This result is in direct conflict with what would be expected if only the surface or conducting patches of the material contributed. Equally important, we performed a study of the dependence on magnetic field tilt angle, which revealed a flat angular dependence of the quantum oscillation frequencies, and therefore the Fermi surface cross-sections, establishing the bulk three-dimensional nature of the Fermi surface. Our thermal measurements further demonstrated experimental signatures unexpected for an insulator, including a sizeable linear specific heat coefficient, and the enhancement of the thermal conductivity in an applied magnetic field. The agreement between the density of states at the Fermi energy inferred from specific heat and quantum oscillations measurements, and the comparable mean free path identified in the case of thermal transport and the oscillatory cyclotron orbits suggest a common origin for the quantum oscillations and the low temperature thermal properties. Lastly, we presented an extensive suite of measurements to evaluate the sample quality of our single crystals, confirming their high purity, with material properties consistent with an impurity concentration of less than 0.05%, and therefore further establishing the intrinsic character of the observed quantum oscillations.

Just as significant has been the discovery of quantum oscillations in YbB_{12} [11], another Kondo insulator. The observation of bulk quantum oscillations in a second material, as revealed by our results, has set the foundation for a new class of correlated insulators that exhibit quantum

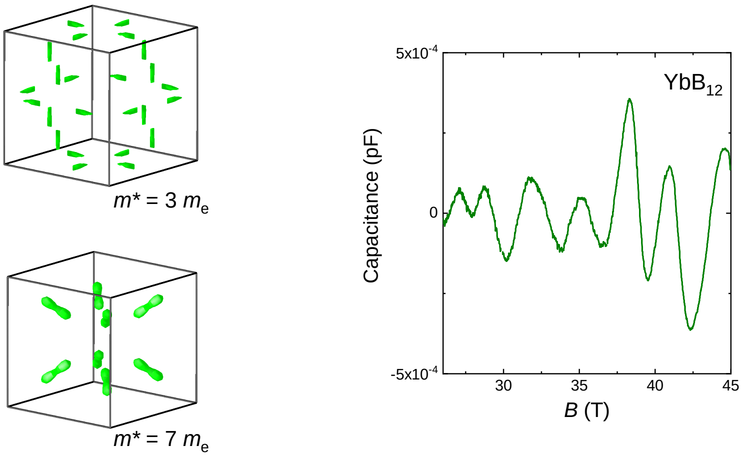

Fig. 7.2 The heavy semimetal Fermi surface inferred from quantum oscillation measurements of YbB_{12}.

oscillations. We highlighted the many similarities between YbB_{12} and SmB_6. Interestingly, the quantum oscillations revealed heavy effective masses, and a small Fermi surface unlike that of SmB_6 or metallic dodecaborides (see Fig. 7.2). The heavy semimetal Fermi surface, indicated by the comparison of our measurements with band structure calculations, and the proximity to an insulator-metal transition in magnetic field represent some key differences compared to SmB_6.

Many questions still remain. For YbB_{12} we presented a Fermi surface model based on a shifted Fermi level, which yields small Fermi pockets and high effective masses, but the complete angular dependence of the quantum oscillations is still to be measured, which is required to confirm the shape of the Fermi pockets. Also to be determined is whether the de Haas–van Alphen and Shubnikov–de Haas results could be consolidated around the same Fermi surface model. Another question pertains whether quantum oscillations could be measured above the insulator-metal transition. This should be possible in pulsed magnetic fields that go above 45 T. In contrast with YbB_{12}, the relevant tuning parameter for SmB_6 is pressure. We highlight the potential of pressure studies in exploring the Fermi surface as the material is tuned across the insulator-metal transition. Still, one the most pertinent tasks remains high magnetic field studies of other families of insulators. Identifying further materials that exhibit quantum oscillations would aid theoretical efforts to develop a model to capture the unconventional ground state of this new class of correlated insulators that exhibit quantum oscillations.

7.2 Quantum oscillations and the vortex matter state of underdoped $YBa_2Cu_3O_{6+x}$

The high-T_c cuprates represent a completely new class of superconductors, that differ greatly from conventional BCS superconductors. In this thesis we investigated the high magnetic field pseudogap ground state of the underdoped cuprates, which, distinct from the Fermi liquid-like overdoped regime, is characterised by a small electron pocket. We accessed the previously unexplored regime of millikelvin temperatures and DC high magnetic fields, unaffected by eddy currents present in pulsed magnetic fields. Remarkably, upon applying low measurement currents we found superconductivity to persist beyond the highest available static magnetic fields. Through the extensive study of the current-voltage dependence, we identified a low temperature–high magnetic field quantum vortex phase, characterised by true zero resistivity superconductivity, bounded by a critical transition, that extends up to at least 45 T. We found this to be in accord with the extent of vortex pinning hysteresis identified by magnetic torque measurements. Our findings, therefore, revealed a new phase diagram for the underdoped cuprates (Fig. 7.3c), that extends the previously proposed extent of superconductivity to much higher fields, encompassing the regime of quantum oscillations previously associated with the normal state (Fig. 7.3a).

We presented quantum oscillations with substantially higher resolution than previous measurements, enabling a harmonic analysis of the waveform of the quantum oscillations, that confirmed the absence of any reservoir density of states. The measured signatures conform with a Fermi surface picture consisting of only a single isolated nodal electron pocket, indicating that the anisotropy of the pseudogap phase survives down to low temperatures. In the same region of the phase diagram we found vanishing electrical resistivity, magnetic hysteresis, and non-ohmic electrical transport characteristics. These further confirmed the coexistence of quantum oscillations with superconductivity, indicating the need for a description outside the

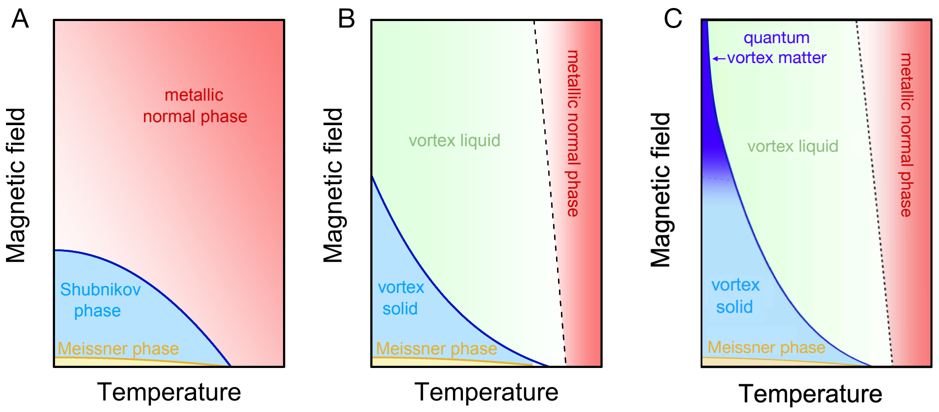

Fig. 7.3 Contrasting different magnetic field–temperature phase diagrams for underdoped $YBa_2Cu_3O_{6+x}$. Adapted from Ref. [246]. (a) Phase diagram for a BCS-like type-II superconductor [18]. In the Meissner phase all flux lines are expelled from the sample, whereas the Shubnikov phase is characterised by field penetration of the sample that leads to pinned vortices. The superconducting order parameter is destroyed above modest magnetic fields, and the metallic normal phase can be accessed down to the lowest temperatures. (b) Phase diagram for a strongly interacting superconductor [232], that is also host to a broad vortex liquid phase of finite resistivity due to vortex dissipation. (c) Phase diagram of a superconductor with strong fluctuations, that is host to a quantum vortex matter phase exhibiting resilient superconductivity at low temperatures and high magnetic fields, in agreement with our results on underdoped $YBa_2Cu_3O_{6+x}$, with quantum oscillations persisting well into the superconducting regime.

scope of conventional band theory, but something that incorporates both the pseudogap and superconductivity and addresses the nodal-antinodal dichotomy. Theories that consider the interplay of superconducting pairing and density wave order parameters seem to be of particular relevance, such as the recently proposed pair density wave (PDW) models [216, 270, 271].

Plenty of open questions remain for experimentalists. Some are likely to be addressed by future measurements, but others seem more challenging. One of the more elusive questions concerns the upper critical field and the extent of the vortex matter state. It is likely that it does not manifest in a clear first-order phase transition, and could prove to be just as ambiguous as the extent of superconducting pairing above T_c. Assuming this crossover region lies at a magnetic field that will become accessible by future magnets, a central task would be to see whether the small Fermi surface pocket survives, or whether it reconstructs into a large hole-like Fermi surface similar to overdoped $Tl_2Ba_2CuO_{6+\delta}$. Our measurements revealed field-resilient superconductivity and strong non-ohmic current-voltage dependence. It is unclear if these signatures are universal across the phase diagram, or limited to just the charge-ordered underdopings. It would also be worthwhile to perform high-sensitivity I-V measurements at low magnetic fields near T_c to see how the behaviour differs from the low temperature–high field regime. Both of these proposal are feasible with current experimental setups. Another important avenue for future experiments would be to look for quantum oscillations in the vortex state of other dopings. With $YBa_2Cu_3O_{6.55}$ we demonstrated that quantum oscillations are observable down to 20 T for a material with a significantly higher upper critical field. Dopings closer to optimal doping or overdoped could be investigated. The vortex state's resilience to magnetic field appears to increase considerably with oxygen doping [18, 81], but the superconducting gap size, which plays the more crucial role in determining the viability of vortex matter quantum oscillations, only increases modestly with oxygen doping [259]. It is just as pertinent to investigate the Fermi surface without CDW in the more underdoped region of the phase diagram. Important questions concern whether these dopings also feature a Fermi surface that reflects the pseudogap, and if they still show quantum oscillations. Much of the progress in the field of high-T_c superconductivity has been driven by experiments, and realising these proposals could bring us closer to a better understanding of the underlying physics.

References

[1] Anderson, P. W. Plasmons, gauge invariance, and mass, *Physical Review* **130**(1), 439 (1963).

[2] Bardeen, J. and Brattain, W. H. The transistor, a semi-conductor triode, *Physical Review* **74**(2), 230 (1948).

[3] Menth, A., Buehler, E., and Geballe, T. H. Magnetic and Semiconducting Properties of SmB_6, *Phys. Rev. Lett.* **22**(7), 295 (1969).

[4] Bednorz, J. G. and Müller, K. A. Possible high T_c superconductivity in the Ba–La–Cu–O system, *Zeitschrift für Physik B Condensed Matter* **64**(2), 189–193 (1986).

[5] Landau, L. Diamagnetismus der Metalle, *Zeitschrift für Physik* **64**(9-10), 629–637 (1930).

[6] Bucher, E., Maita, J., Hull, G., Fulton, R., and Cooper, A. Electronic properties of beryllides of the rare earth and some actinides, *Phys. Rev. B* **11**(1), 440 (1975).

[7] Steglich, F., Aarts, J., Bredl, C., Lieke, W., Meschede, D., Franz, W., and Schäfer, H. Superconductivity in the Presence of Strong Pauli Paramagnetism: $CeCu_2Si_2$, *Phys. Rev. Lett.* **43**(25), 1892 (1979).

[8] Simon, S. H. *The Oxford solid state basics*. Oxford University Press, Oxford, UK, (2013).

[9] Li, G., Xiang, Z., Yu, F., Asaba, T., Lawson, B., Cai, P., Tinsman, C., Berkley, A., Wolgast, S., Eo, Y. S., et al. Two-dimensional Fermi surfaces in Kondo insulator SmB_6, *Science* **346**(6214), 1208–1212 (2014).

[10] Tan, B. S., Hsu, Y.-T., Zeng, B., Ciomaga Hatnean, M., Harrison, N., Zhu, Z., Hartstein, M., Kiourlappou, M., Srivastava, A., Johannes, M. D., Murphy, T. P., Park, J.-H., Balicas, L., Lonzarich, G. G., Balakrishnan, G., and Sebastian, S. E. Unconventional Fermi surface in an insulating state, *Science* **349**(6245), 287–290 (2015).

[11] Liu, H., Hartstein, M., Wallace, G. J., Davies, A. J., Hatnean, M. C., Johannes, M. D., Shitsevalova, N., Balakrishnan, G., and Sebastian, S. E. Fermi surfaces in Kondo insulators, *Journal of Physics: Condensed Matter* **30**(16), 16LT01 (2018).

[12] Xiang, Z., Kasahara, Y., Asaba, T., Lawson, B., Tinsman, C., Chen, L., Sugimoto, K., Kawaguchi, S., Sato, Y., Li, G., Yao, S., Chen, Y. L., Iga, F., Singleton, J., Matsuda, Y., and Li, L. Quantum oscillations of electrical resistivity in an insulator, *Science* **362**(6410), 65–69 (2018).

[13] Shoenberg, D. *Magnetic Oscillations in Metals*. Cambridge University Press, Cambridge, UK, (1984).

[14] Wu, M.-K., Ashburn, J. R., Torng, C., Hor, P. H., Meng, R. L., Gao, L., Huang, Z. J., Wang, Y., and Chu, a. Superconductivity at 93 K in a new mixed-phase Y–Ba–Cu–O compound system at ambient pressure, *Phys. Rev. Lett.* **58**(9), 908 (1987).

[15] Doiron-Leyraud, N., Proust, C., LeBoeuf, D., Levallois, J., Bonnemaison, J.-B., Liang, R., Bonn, D., Hardy, W., and Taillefer, L. Quantum oscillations and the Fermi surface in an underdoped high-T_c superconductor, *Nature* **447**(7144), 565 (2007).

[16] Huse, D. A., Fisher, M. P., and Fisher, D. S. Are superconductors really superconducting?, *Nature* **358**(6387), 553 (1992).

[17] Fisher, D. S., Fisher, M. P., and Huse, D. A. Thermal fluctuations, quenched disorder, phase transitions, and transport in type-ii superconductors, *Phys. Rev. B* **43**(1), 130 (1991).

[18] Grissonnanche, G., Cyr-Choinière, O., Laliberté, F., De Cotret, S. R., Juneau-Fecteau, A., Dufour-Beauséjour, S., Delage, M.-E., LeBoeuf, D., Chang, J., Ramshaw, B., et al. Direct measurement of the upper critical field in cuprate superconductors, *Nature communications* **5**, 3280 (2014).

[19] Doniach, S. The kondo lattice and weak antiferromagnetism, *Physica B* **91**, 231–234 (1977).

[20] Kondo, J. Anomalous Hall effect and magnetoresistance of ferromagnetic metals, *Progress of Theoretical Physics* **27**(4), 772–792 (1962).

[21] Kondo, J. Resistance minimum in dilute magnetic alloys, *Progress of theoretical physics* **32**(1), 37–49 (1964).

[22] Steglich, F., Arndt, J., Stockert, O., Friedemann, S., Brando, M., Klingner, C., Krellner, C., Geibel, C., Wirth, S., Kirchner, S., and Si, Q. Magnetism, f-electron localization and superconductivity in 122-type heavy-fermion metals, *Journal of Physics: Condensed Matter* **24**(29), 294201 (2012).

[23] Suhl, H. Dispersion Theory of the Kondo Effect, *Physical Review* **138**, A515–A523 Apr (1965).

[24] Gold, A. V. The de Haas-van Alphen Effect. In *Solid State Physics (vol. 1 Electrons in Metals),* Cochran, J. F. and Haering, R. R., editors, 39–126. Gordon and Breach, New York (1968).

[25] Abrikosov, A. *Fundamentals of the Theory of Metals*.

[26] Maniv, T., Zhuravlev, V., Vagner, I., and Wyder, P. Vortex states and quantum magnetic oscillations in conventional type-II superconductors, *Reviews of Modern Physics* **73**(4), 867 (2001).

[27] Harrison, N., Bogaerts, R., Reinders, P., Singleton, J., Blundell, S., and Herlach, F. Numerical model of quantum oscillations in quasi-two-dimensional organic metals in high magnetic fields, *Phys. Rev. B* **54**(14), 9977 (1996).

[28] Harrison, N., Meeson, P., Probst, P.-A., and Springford, M. Quasiparticle and thermodynamic mass in the heavy-fermion system CeB_6, *Journal of Physics: Condensed Matter* **5**(40), 7435 (1993).

[29] Hartstein, M., Toews, W. H., Hsu, Y.-T., Zeng, B., Chen, X., Ciomaga Hatnean, M., Zhang, Q. R., Nakamura, S., Padgett, A. S., Rodway-Gant, G., Berk, J., Kingston, M. K., Zhang, G. H., Chan, M. K., Yamashita, S., Sakakibara, T., Takano, Y., Park, J.-H., Balicas, L., Harrison, N., Shitsevalova, N., Balakrishnan, G., Lonzarich, G. G., Hill, R. W., Sutherland, M., and Sebastian, S. E. Fermi surface in the absence of a Fermi liquid in the Kondo insulator SmB_6, *Nature Physics* **14**, 166–172 (2018).

[30] Altarawneh, M., Mielke, C., and Brooks, J. Proximity detector circuits: An alternative to tunnel diode oscillators for contactless measurements in pulsed magnetic field environments, *Review of Scientific Instruments* **80**(6), 066104 (2009).

[31] Sebastian, S. E., Harrison, N., Altarawneh, M., Mielke, C., Liang, R., Bonn, D., and Lonzarich, G. Metal-insulator quantum critical point beneath the high T_c superconducting dome, *Proceedings of the National Academy of Sciences* **107**(14), 6175–6179 (2010).

[32] Chan, M. K., Harrison, N., McDonald, R. D., Ramshaw, B., Modic, K. A., Barišić, N., and Greven, M. Single reconstructed Fermi surface pocket in an underdoped single-layer cuprate superconductor, *Nature communications* **7**(1), 1–9 (2016).

[33] Griessen, R. A capacitance torquemeter for de Haas-van Alphen measurements, *Cryogenics* **13**(6), 375–377 (1973).

[34] Tan, B. S. *High magnetic field study of strongly correlated electron systems (Doctoral thesis)*. University of Cambridge, (2019).

[35] Qvarford, M., Heeck, K., Lensink, J., Wijngaarden, R., and Griessen, R. Microtorquemeter for magnetization measurements on small superconducting samples, *Review of scientific instruments* **63**(12), 5726–5732 (1992).

[36] Kasuya, T., Takegahara, K., Fujita, T., Tanaka, T., and Bannai, E. Valence fluctuating state in SmB_6, *J. Phys. Colloques* **40**(C5), 308–313 (1979).

[37] Peña, O., Lysak, M., MacLaughlin, D., and Fisk, Z. Nuclear spin relaxation, hybridization, and low-temperature 4f spin fluctuations in intermediate-valent SmB_6, *Solid State Communications* **40**(5), 539–541 (1981).

[38] Frankowski, I. and Wachter, P. Point-contact spectroscopy on SmB_6, TmSe, LaB_6 and LaSe, *Solid State Communications* **41**(8), 577–580 (1982).

[39] Travaglini, G. and Wachter, P. Intermediate-valent SmB_6 and the hybridization model: An optical study, *Phys. Rev. B* **29**(2), 893 (1984).

[40] Amsler, B., Fisk, Z., Sarrao, J., Von Molnar, S., Meisel, M., and Sharifi, F. Electron-tunneling studies of the hexaboride materials SmB_6, EuB_6, CeB_6, and SrB_6, *Phys. Rev. B* **57**(15), 8747 (1998).

[41] Phelan, W., Koohpayeh, S., Cottingham, P., Freeland, J., Leiner, J., Broholm, C., and McQueen, T. Correlation between bulk thermodynamic measurements and the low-temperature-resistance plateau in SmB_6, *Phys. Rev. X* **4**(3), 031012 (2014).

[42] Gabáni, S., Orendáč, M., Pristáš, G., Gažo, E., Diko, P., Piovarči, S., Glushkov, V., Sluchanko, N., Levchenko, A., Shitsevalova, N., et al. Transport properties of variously doped SmB_6, *Philosophical Magazine* **96**(31), 3274–3283 (2016).

[43] Nickerson, J., White, R., Lee, K., Bachmann, R., Geballe, T., and Hull Jr, G. Physical Properties of SmB_6, *Phys. Rev. B* **3**(6), 2030–2042 (1971).

[44] Dzero, M., Sun, K., Galitski, V., and Coleman, P. Topological Kondo Insulators, *Phys. Rev. Lett.* **104**, 106408 (2010).

[45] Kim, D. J., Thomas, S., Grant, T., P., Botimer, J., Fisk, Z., and Xia, J. Surface Hall Effect and Nonlocal Transport in SmB_6: Evidence for Surface Conduction, *Scientific Reports* **3**, 3150 (2013).

[46] Wolgast, S., Kurdak, Cagliyan, K., Sun, K., Allen, J. W., Kim, D.-J., and Fisk, Z. Low-temperature surface conduction in the Kondo insulator SmB_6, *Phys. Rev. B* **88**, 180405 (2013).

[47] Herzig, P., Fojud, Z., Żogał, O., Pietraszko, A., Dukhnenko, A., Jurga, S., and Shitsevalova, N. Electric-field-gradient tensor and charge densities in LaB_6: B^{11} nuclear-magnetic-resonance single-crystal investigations and first-principles calculations, *Journal of Applied Physics* **103**(8), 083534 (2008).

[48] Hatnean, M. C., Lees, M. R., Paul, D. M., and Balakrishnan, G. Large, high quality single-crystals of the new Topological Kondo Insulator, SmB_6, *Scientific Reports* **3**, 3071 (2013).

[49] Vainshtein, E. E., B. S. M. and Paderno, Y. B. X-ray spectral investigation of samarium hexaboride, *Sov. Phys. Solid State* **6**(10), 2909–2912 (1964).

[50] Utsumi, Y., Kasinathan, D., Ko, K.-T., Agrestini, S., Haverkort, M., Wirth, S., Wu, Y., Tsuei, K., Kim, D., Fisk, Z., et al. Bulk and surface electronic properties of SmB_6: A hard x-ray photoelectron spectroscopy study, *Phys. Rev. B* **96**(15), 155130 (2017).

[51] Degiorgi, L. The electrodynamic response of heavy-electron compounds, *Reviews of Modern Physics* **71**(3), 687 (1999).

[52] Derr, J., Knebel, G., Braithwaite, D., Salce, B., Flouquet, J., Flachbart, K., Gabáni, S., and Shitsevalova, N. From unconventional insulating behavior towards conventional magnetism in the intermediate-valence compound SmB_6, *Phys. Rev. B* **77**(19), 193107 (2008).

[53] Wolgast, S., Eo, Y., Sun, K., Kurdak, C., Balakirev, F., Jaime, M., Kim, D.-J., and Fisk, Z. Reduction of the low-temperature bulk gap in samarium hexaboride under high magnetic fields, *Phys. Rev. B* **95**(24), 245112 (2017).

[54] Stankiewicz, J., Evangelisti, M., and Fisk, Z. Specific heat of $Nd_{1-x}Ca_xB_6$ single crystals, *Phys. Rev. B* **83**, 113108 (2011).

[55] Hlawenka, P., Siemensmeyer, K., Weschke, E., Varykhalov, A., Sánchez-Barriga, J., Shitsevalova, N. Y., Dukhnenko, A., Filipov, V., Gabáni, S., Flachbart, K., et al. Samarium hexaboride is a trivial surface conductor, *Nature communications* **9**(1), 517 (2018).

[56] Phelan, W., Koohpayeh, S., Cottingham, P., Tutmaher, J., Leiner, J., Lumsden, M., Lavelle, C., Wang, X., Hoffmann, C., Siegler, M., et al. On the chemistry and physical properties of flux and floating zone grown SmB_6 single crystals, *Scientific Reports* **6**, 20860 (2016).

[57] Kim, D.-J., Xia, J., and Fisk, Z. Topological surface state in the Kondo insulator samarium hexaboride, *Nature Materials* **13**(5), 466 (2014).

[58] Toews, William Henry. *An investigation of low energy quasiparticle excitations via thermal transport measurements (Doctoral thesis).* University of Waterloo, (2017).

[59] Gabáni, S., Flachbart, K., Pavlik, V., Konovalova, E., Paderno, Y., and Herrmannsdörfer, T. Low Temperature Transport and Magnetic Properties of SmB_6, *Acta Physica Polonica A* **97**(3), 419–422 (2000).

[60] Hung, C. and Gliessman, J. Resistivity and hall effect of germanium at low temperatures, *Physical Review* **96**(5), 1226 (1954).

[61] Tanaka, T., Akahane, T., Bannai, E., Kawai, S., Tsuda, N., and Ishizawa, Y. Role of polar optical phonon scattering in electrical resistivities of LaB_6 and ReO_3 (metallic conduction), *Journal of Physics C: Solid State Physics* **9**(7), 1235 (1976).

[62] Takigawa, M., Yasuoka, H., Kitaoka, Y., Tanaka, T., Nozaki, H., and Ishizawa, Y. NMR study of a valence fluctuating compound SmB_6, *Journal of the Physical Society of Japan* **50**(8), 2525–2532 (1981).

[63] Al'tshuler, T., Khaliullin, G., and Khomskii, D. Investigation of the energy gap in SmB_6 by the ESR technique, *Journal of Experimental and Theoretical Physics* **90**(6), 2104–2110 (1986).

[64] Lee, W. and Shelton, R. CePtSi: A new heavy-fermion compound, *Phys. Rev. B* **35**(10), 5369 (1987).

[65] Flouquet, J. and Harima, H. Heavy fermion material: Ce versus Yb case, *arXiv preprint arXiv:0910.3110* (2009).

[66] Caldwell, T., Reyes, A. P., Moulton, W. G., Kuhns, P. L., Hoch, M. J. R., Schlottmann, P., and Fisk, Z. High-field suppression of in-gap states in the Kondo insulator SmB_6, *Phys. Rev. B* **75**, 075106 (2007).

[67] Laurita, N. J., Morris, C. M., Koohpayeh, S. M., Rosa, P. F. S., Phelan, W. A., Fisk, Z., McQueen, T. M., and Armitage, N. P. Anomalous three-dimensional bulk AC conduction within the Kondo gap of SmB_6 single crystals, *Phys. Rev. B* **94**, 165154 (2016).

[68] Glushkov, V., Kuznetsov, A., Churkin, O., Demishev, S., Paderno, Y. B., Shitsevalova, N. Y., and Sluchanko, N. Spin gap formation in SmB_6, *Physica B: Condensed Matter* **378**, 614–615 (2006).

[69] Coleman, P. Heavy fermions: Electrons at the edge of magnetism, *Handbook of magnetism and advanced magnetic materials* (2007).

[70] Müller, K. and Narozhnyi, V. Interaction of superconductivity and magnetism in borocarbide superconductors, *Reports on Progress in Physics* **64**(8), 943 (2001).

[71] Opagiste, C., Barbier, C., Haettel, R., and Galéra, R.-M. Physical properties of the $R_3Pt_{23}Si_{11}$ compounds with volatile rare earth: Sm, Eu, Tm and Yb, *Journal of Magnetism and Magnetic Materials* **378**, 402–408 (2015).

[72] Langford, H., Temmerman, W., and Gehring, G. Enhancements and Fermi surfaces of rare-earth hexaborides, *Journal of Physics: Condensed Matter* **2**(3), 559 (1990).

[73] Onuki, Y., Umezawa, A., Kwok, W., Crabtree, G., Nishihara, M., Yamazaki, T., Omi, T., and Komatsubara, T. High-field magnetoresistance and de Haas–van Alphen effect in antiferromagnetic PrB_6 and NdB_6, *Phys. Rev. B* **40**(16), 11195 (1989).

[74] Ōnuki, Y., Komatsubara, T., H P Reinders, P., and Springford, M. Fermi surface and cyclotron mass of CeB_6, *Journal of the Physical Society of Japan* **58**(10), 3698–3704 (1989).

[75] Arko, A., Crabtree, G., Karim, D., Mueller, F., Windmiller, L., Ketterson, J. B., and Fisk, Z. de Haas-van Alphen effect and the Fermi surface of LaB_6, *Phys. Rev. B* **13**(12), 5240 (1976).

[76] Ishizawa, Y., Tanaka, T., Bannai, E., and Kawai, S. de Haas-van Alphen effect and Fermi surface of LaB_6, *Journal of the Physical Society of Japan* **42**(1), 112–118 (1977).

[77] Ishizawa, Y., Nozaki, H., Tanaka, T., and Nakajima, T. Low-Field de Haas-van Alphen Effect in LaB_6, *Journal of the Physical Society of Japan* **48**(5), 1439–1442 (1980).

[78] Neupane, M., Alidoust, N., Xu, S., Kondo, T., Ishida, Y., Kim, D.-J., Liu, C., Belopolski, I., Jo, Y., Chang, T.-R., et al. Surface electronic structure of the topological Kondo-insulator candidate correlated electron system SmB_6, *Nature communications* **4**, 2991 (2013).

[79] Behler, S. and Winzer, K. De Haas-van Alphen effect in rare-earth hexaborides (RE= Pr, Nd, Gd), *Zeitschrift für Physik B Condensed Matter* **82**(3), 355–361 (1991).

[80] Ōnuki, Y., Nishihara, M., Sato, M., and Komatsubara, T. Fermi surface and cyclotron mass of PrB_6, *Journal of Magnetism and Magnetic Materials* **52**(1-4), 317–319 (1985).

[81] Hsu, Y.-T. *Unconventional Fermi surface in insulating* SmB_6 *and superconducting* $YBa_2Cu_3O_{6+x}$ *probed by high magnetic fields (Doctoral thesis)*. University of Cambridge, (2018).

[82] Riseborough, P. S. and Fisk, Z. Critical examination of quantum oscillations in SmB_6, *Phys. Rev. B* **96**, 195122 (2017).

[83] Knolle, J. and Cooper, N. R. Quantum Oscillations without a Fermi Surface and the Anomalous de Haas–van Alphen Effect, *Phys. Rev. Lett.* **115**(14), 146401 (2015).

[84] Blount, E. Bloch electrons in a magnetic field, *Physical Review* **126**(5), 1636 (1962).

[85] Suzuki, T., Goto, T., Sakatsume, S., Tamaki, A., Kunii, S., Kasuya, T., and Fujimura, T. Acoustic de Haas-van Alphen Effect of CeB_6 and LaB_6, *Japanese Journal of Applied Physics* **26**(S3-1), 511 (1987).

[86] Yamashita, S., Yamamoto, T., Nakazawa, Y., Tamura, M., and Kato, R. Gapless spin liquid of an organic triangular compound evidenced by thermodynamic measurements, *Nature communications* **2**, 275 (2011).

[87] Yamashita, M., Nakata, N., Senshu, Y., Nagata, M., Yamamoto, H. M., Kato, R., Shibauchi, T., and Matsuda, Y. Highly mobile gapless excitations in a two-dimensional candidate quantum spin liquid, *Science* **328**(5983), 1246–1248 (2010).

[88] Yamashita, M., Shibauchi, T., and Matsuda, Y. Thermal-Transport Studies on Two-Dimensional Quantum Spin Liquids, *ChemPhysChem* **13**(1), 74–78 (2012).

[89] Anisimov, M., Bogach, A., Glushkov, V., Demishev, S., Samarin, N., Gavrilkin, S., Mitsen, K., Shitsevalova, N., Levchenko, A., Filippov, V., et al. Defect mode in LaB_6, *Acta Phys Pol A* **126**(1), 350–1 (2014).

[90] Müller, T., Joss, W., Van Ruitenbeek, J., Welp, U., Wyder, P., and Fisk, Z. Magnetic field dependence of the many-body enhancement on the Fermi surface of CeB_6, *Journal of Magnetism and Magnetic Materials* **76**, 35–36 (1988).

[91] Boulanger, M.-E., Laliberté, F., Dion, M., Badoux, S., Doiron-Leyraud, N., Phelan, W. A., Koohpayeh, S. M., Fuhrman, W. T., Chamorro, J. R., McQueen, T. M., Wang, X. F., Nakajima, Y., Metz, T., Paglione, J., and Taillefer, L. Field-dependent heat transport in the Kondo insulator SmB_6: Phonons scattered by magnetic impurities, *Phys. Rev. B* **97**, 245141 (2018).

[92] Biswas, P. K., Salman, Z., Neupert, T., Morenzoni, E., Pomjakushina, E., von Rohr, F., Conder, K., Balakrishnan, G., Hatnean, M. C., Lees, M. R., Paul, D. M., Schilling, A., Baines, C., Luetkens, H., Khasanov, R., and Amato, A. Low-temperature magnetic fluctuations in the Kondo insulator SmB_6, *Phys. Rev. B* **89**, 161107 (2014).

[93] Fuhrman, W. T., Leiner, J., Nikolić, P., Granroth, G. E., Stone, M. B., Lumsden, M. D., DeBeer-Schmitt, L., Alekseev, P. A., Mignot, J.-M., Koohpayeh, S. M., Cottingham, P., Phelan, W. A., Schoop, L., McQueen, T. M., and Broholm, C. Interaction Driven Subgap Spin Exciton in the Kondo Insulator SmB_6, *Phys. Rev. Lett.* **114**, 036401 (2015).

[94] Xu, Y., Cui, S., Dong, J., Zhao, D., Wu, T., Chen, X., Sun, K., Yao, H., and Li, S. Bulk Fermi surface of charge-neutral excitations in SmB_6 or not: a heat-transport study, *Phys. Rev. Lett.* **116**(24), 246403 (2016).

[95] Nave, C. P. and Lee, P. A. Transport properties of a spinon Fermi surface coupled to a U(1) gauge field, *Phys. Rev. B* **76**(23), 235124 (2007).

[96] Yamashita, M., Nakata, N., Kasahara, Y., Sasaki, T., Yoneyama, N., Kobayashi, N., Fujimoto, S., Shibauchi, T., and Matsuda, Y. Thermal-transport measurements in a quantum spin-liquid state of the frustrated triangular magnet κ-(BEDT-TTF)$_2$Cu$_2$ (CN)$_3$, *Nature Physics* **5**(1), 44–47 (2009).

[97] Capponi, S. and Assaad, F. Spin and charge dynamics of the ferromagnetic and antiferromagnetic two-dimensional half-filled Kondo lattice model, *Phys. Rev. B* **63**(15), 155114 (2001).

[98] Cooley, J., Aronson, M., Fisk, Z., and Canfield, P. High pressure insulator-metal transition in SmB_6, *Physica B: Condensed Matter* **199–200**, 486 – 488 (1994).

[99] Gabáni, S., Bauer, E., Berger, S., Flachbart, K., Paderno, Y., Paul, C., Pavlík, V., and Shitsevalova, N. Pressure-induced Fermi-liquid behavior in the Kondo insulator SmB_6: Possible transition through a quantum critical point, *Phys. Rev. B* **67**, 172406 (2003).

[100] Barla, A., Derr, J., Sanchez, J., Salce, B., Lapertot, G., Doyle, B., Rüffer, R., Lengsdorf, R., Abd-Elmeguid, M., and Flouquet, J. High-pressure ground state of SmB_6: electronic conduction and long range magnetic order, *Phys. Rev. Lett.* **94**(16), 166401 (2005).

[101] Pixley, J., Yu, R., Paschen, S., and Si, Q. Global Phase Diagram and Momentum Distribution of Single-Particle Excitations in Kondo insulators, *arXiv preprint arXiv:1509.02907* (2015).

[102] Kagan, Y., Kikion, K., and Prokof'ev, N. Heavy fermions in the Kondo lattice as neutral quasiparticles, *Physica B: Condensed Matter* **182**(3), 201–208 (1992).

[103] Senthil, T., Sachdev, S., and Vojta, M. Fractionalized Fermi Liquids, *Phys. Rev. Lett.* **90**, 216403 (2003).

[104] Senthil, T., Vojta, M., and Sachdev, S. Weak magnetism and non-fermi liquids near heavy-fermion critical points, *Phys. Rev. B* **69**, 035111 (2004).

[105] Coleman, P., Marston, J. B., and Schofield, A. J. Transport anomalies in a simplified model for a heavy-electron quantum critical point, *Phys. Rev. B* **72**, 245111 (2005).

[106] Knolle, J. and Cooper, N. R. Excitons in topological Kondo insulators-theory of thermodynamic and transport anomalies in SmB_6, *Phys. Rev. Lett.* **118**, 096604 (2017).

[107] Anderson, P. Breaking the log-jam in many-body physics: Fermi surfaces without Fermi liquids, *Physica Scripta* **T42**, 11–16 (1992).

[108] Grover, T., Trivedi, N., Senthil, T., and Lee, P. A. Weak Mott insulators on the triangular lattice: possibility of a gapless nematic quantum spin liquid, *Phys. Rev. B* **81**(24), 245121 (2010).

[109] Lee, S.-S. and Lee, P. A. U(1) gauge theory of the Hubbard model: Spin liquid states and possible application to κ-(BEDT- TTF)$_2$Cu$_2$(CN)$_3$, *Phys. Rev. Lett.* **95**(3), 036403 (2005).

[110] Motrunich, O. I. Orbital magnetic field effects in spin liquid with spinon Fermi sea: Possible application to κ-(ET)$_2$Cu$_2$(CN)$_3$, *Phys. Rev. B* **73**, 155115 (2006).

[111] Katsura, H., Nagaosa, N., and Lee, P. A. Theory of the thermal Hall effect in quantum magnets, *Phys. Rev. Lett.* **104**(6), 066403 (2010).

[112] Mross, D. F. and Senthil, T. Charge Friedel oscillations in a Mott insulator, *Phys. Rev. B* **84**, 041102 (2011).

[113] Sodemann, I., Chowdhury, D., and Senthil, T. Quantum oscillations in insulators with neutral Fermi surfaces, *Phys. Rev. B* **97**, 045152 (2018).

[114] Chowdhury, D., Sodemann, I., and Senthil, T. Mixed-valence insulators with neutral Fermi surfaces, *Nature communications* **9**(1), 1766 (2018).

[115] Coleman, P., Miranda, E., and Tsvelik, A. Are Kondo insulators gapless?, *Physica B: Condensed Matter* **186**, 362–364 (1993).

[116] Baskaran, G. Majorana Fermi Sea in Insulating SmB_6: A proposal and a Theory of Quantum Oscillations in Kondo Insulators, *arXiv preprint arXiv:1507.03477* (2015).

[117] Erten, O., Chang, P.-Y., Coleman, P., and Tsvelik, A. M. Skyrme insulators: Insulators at the brink of superconductivity, *Phys. Rev. Lett.* **119**, 057603 (2017).

[118] Heath, J. and Bedell, K. Exotic quantum statistics and thermodynamics from a number-conserving theory of Majorana fermions, *Journal of Physics A: Mathematical and Theoretical* .

[119] Heath, J. T. and Bedell, K. S. Collective Excitations and Robust Stability in a Landau-Majorana Liquid, *Journal of Physics: Condensed Matter* **32**(48), 485602 (2020).

[120] Shen, H. and Fu, L. Quantum Oscillation from In-Gap States and a Non-Hermitian Landau Level Problem, *Phys. Rev. Lett.* **121**, 026403 (2018).

[121] Thomas, S. M., Ding, X., Ronning, F., Zapf, V., Thompson, J. D., Fisk, Z., Xia, J., and Rosa, P. F. S. Quantum Oscillations in Flux-Grown SmB_6 with Embedded Aluminum, *Phys. Rev. Lett.* **122**, 166401 (2019).

[122] Fuhrman, W. and Nikolić, P. Magnetic impurities in Kondo insulators and the puzzle of samarium hexaboride, *Phys. Rev. B* **101**, 245118 Jun (2020).

[123] Fuhrman, W., Chamorro, J., Alekseev, P., Mignot, J.-M., Keller, T., Rodriguez-Rivera, J., Qiu, Y., Nikolić, P., McQueen, T., and Broholm, C. L. Screened moments and extrinsic in-gap states in samarium hexaboride, *Nature communications* **9**(1), 1539 (2018).

[124] Geballe, T., Menth, A., Buehler, E., and Hull, G. Properties of SmB_6 doped with Eu and Gd, *Journal of Applied Physics* **41**(3), 904–905 (1970).

[125] Gabáni, S., Flachbart, K., Pavlik, V., Orendáč, M., Konovalova, E., Paderno, Y., and Šebek, J. Investigation of in-gap states in SmB_6, *Czechoslovak Journal of Physics* **52**(2), 279–282 (2002).

[126] Orendáč, M., Gabáni, S., Pristáš, G., Gažo, E., Diko, P., Farkašovský, P., Levchenko, A., Shitsevalova, N., and Flachbart, K. Isosbestic points in doped SmB_6 as features of universality and property tuning, *Phys. Rev. B* **96**(11), 115101 (2017).

[127] Konovalova, E., Paderno, Y. B., Lundstrem, T., Finkel'shtein, L., Efremova, N., and Dudnik, E. Effect of vacancies and foreign metal ions on the valent state of samarium in SmB_6, *Soviet Powder Metallurgy and Metal Ceramics* **21**(10), 820–823 (1982).

[128] Gabáni, S., Flachbart, K., Pavlík, V., Herrmannsdörfer, T., Konovalova, E., Paderno, Y., Briančin, J., and Trpčevská, J. Magnetic properties of SmB_6 and $Sm_{1-x}La_xB_6$ solid solutions, *Czechoslovak Journal of Physics* **52**(1), A225–A228 (2002).

[129] Nefedova, E., Alekseev, P., Klement'ev, E., Lazukov, V., Sadikov, I., Khlopkin, M., Tsetlin, M., Konovalova, E., and Paderno, Y. B. Imperfection of the Sm sublattice and valence instability in compounds based on SmB_6, *Journal of Experimental and Theoretical Physics* **88**(3), 565–573 (1999).

[130] Wolf, B., Blick, R., Bruls, G., Lüthi, B., Fisk, Z., Smith, J., and Ott, H. Magnetoacoustic quantum oscillations in the heavy fermion superconductor UBe_{13}, *Zeitschrift für Physik B Condensed Matter* **85**(2), 159–160 (1991).

[131] Corcoran, R., Meeson, P., Probst, P., Springford, M., Wolf, B., Blick, R., Bruls, G., Lüthi, B., Fisk, Z., Smith, J., et al. Comment on the observation of magnetoacoustic quantum oscillations in UBe_{13}, *Zeitschrift für Physik B Condensed Matter* **91**(2), 135–137 (1993).

[132] Terashima, T., Terakura, C., Umeda, Y., Kimura, N., Aoki, H., and Kunii, S. Ferromagnetism vs Paramagnetism and False Quantum Oscillations in Lanthanum-Doped Ca_6, *Journal of the Physical Society of Japan* **69**(8), 2423–2426 (2000).

[133] Canfield, P. C. and Fisher, I. R. High-temperature solution growth of intermetallic single crystals and quasicrystals, *Journal of Crystal Growth* **225**(2-4), 155–161 (2001).

[134] Gabáni, S., Flachbart, K., Konovalova, E., Orendáč, M., Paderno, Y., Pavlık, V., and Šebek, J. Properties of the in-gap states in SmB_6, *Solid State Communications* **117**(11), 641–644 (2001).

[135] Hartstein, M., Liu, H., Hsu, Y.-T., Tan, B. S., Ciomaga Hatnean, M., Balakrishnan, G., and Sebastian, S. E. Intrinsic Bulk Quantum Oscillations in a Bulk Unconventional Insulator SmB_6, *iScience* **23**(11), 101632 (2020).

[136] Sera, M., Kobayashi, S., Hiroi, M., Kobayashi, N., and Kunii, S. Thermal conductivity of RB_6 (R= Ce, Pr, Nd, Sm, Gd) single crystals, *Phys. Rev. B* **54**(8), R5207 (1996).

[137] Popov, P., Novikov, V., Sidorov, A., and Maksimenko, E. Thermal conductivity of LaB_6 and SmB_6 in the range 6–300 K, *Inorganic Materials* **43**(11), 1187–1191 (2007).

[138] Yamashita, M. Boundary-limited and glassy-like phonon thermal conduction in $EtMe_3Sb[Pd(dmit)_2]_2$, *Journal of the Physical Society of Japan* **88**(8), 083702 (2019).

[139] Pristáš, G., Gabáni, S., Flachbart, K., Filipov, V., and Shitsevalova, N. Investigation of the Energy Gap in $Sm_{1-x}B_6$ and $Sm_{1-x}La_xB_6$ Kondo Insulators, *JPS Conf. Proc.* **3**, 012021 (2014).

[140] Blundell, S. *Magnetism in Condensed Matter.* Oxford University Press, (2001).

[141] Anderson, J. R. and Lane, S. S. High-Frequency dc Haas-van Alphen Oscillations in Aluminum, *Phys. Rev. B* **2**, 298–309 (1970).

[142] Larson, C. O. and Gordon, W. L. Low-Field de Haas–van Alphen Study of the Fermi Surface of Aluminum, *Physical Review* **156**, 703–715 (1967).

[143] Boyne, C. M. and Mackinnon, L. An investigation of the third-zone Fermi surface of aluminium using ultrasonic quantum oscillations, *Journal of Physics F: Metal Physics* **8**(4), 629 (1978).

[144] Ashcroft, N. The fermi surface of aluminium, *Philosophical Magazine* **8**(96), 2055–2083 (1963).

[145] Xiang, Z., Lawson, B., Asaba, T., Tinsman, C., Chen, L., Shang, C., Chen, X., and Li, L. Bulk Rotational Symmetry Breaking in Kondo Insulator SmB_6, *Phys. Rev. X* **7**(3), 031054 (2017).

[146] Zhang, L., Song, X.-Y., and Wang, F. Quantum Oscillation in Narrow-Gap Topological Insulators, *Phys. Rev. Lett.* **116**, 046404 (2016).

[147] Pal, H. K., Piéchon, F., Fuchs, J.-N., Goerbig, M., and Montambaux, G. Chemical potential asymmetry and quantum oscillations in insulators, *Phys. Rev. B* **94**, 125140 (2016).

[148] Erten, O., Ghaemi, P., and Coleman, P. Kondo Breakdown and Quantum Oscillations in SmB_6, *Phys. Rev. Lett.* **116**, 046403 (2016).

[149] Thomson, A. and Sachdev, S. Fractionalized Fermi liquid on the surface of a topological Kondo insulator, *Phys. Rev. B* **93**, 125103 (2016).

[150] Paul, I., Pépin, C., and Norman, M. Kondo breakdown and hybridization fluctuations in the Kondo-Heisenberg lattice, *Phys. Rev. Lett.* **98**(2), 026402 (2007).

[151] Ramos, E., Franco, R., Silva-Valencia, J., Foglio, M. E., and Figueira, M. S. The role of short-range magnetic correlations in the gap opening of topological kondo insulators, *Journal of Physics: Condensed Matter* **29**(34), 345601 (2017).

[152] Pal, H. K. Quantum oscillations from inside the Fermi sea, *Phys. Rev. B* **95**(8), 085111 (2017).

[153] Pal, H. K. Unusual frequency of quantum oscillations in strongly particle-hole asymmetric insulators, *Phys. Rev. B* **96**, 235121 (2017).

[154] Wu, Q. and Sun, L. Puzzle maker in SmB_6: accompany-type valence fluctuation state, *Reports on Progress in Physics* **80**(11), 112501 (2017).

[155] Harrison, N. Highly asymmetric nodal semimetal in bulk smb_6, *Phys. Rev. Lett.* **121**(2), 026602 (2018).

[156] Ram, P. and Kumar, B. Theory of quantum oscillations of magnetization in Kondo insulators, *Phys. Rev. B* **96**, 075115 (2017).

[157] Ram, P. and Kumar, B. Inversion and magnetic quantum oscillations in the symmetric periodic Anderson model, *Phys. Rev. B* **99**, 235130 (2019).

[158] Peters, R., Yoshida, T., and Kawakami, N. Quantum oscillations in strongly correlated topological Kondo insulators, *arXiv preprint arXiv:1901.05099* **100**(8), 085124 (2019).

[159] Pal, H. K. Anomalies in a slightly doped insulator with strong particle-hole asymmetry and a narrow gap: The case of SmB_6, *Phys. Rev. B* **99**, 045149 (2019).

[160] Sakhya, A. P. and Maiti, K. Anomalous ground state properties of SmB_6-a density functional theoretical study, *arXiv preprint arXiv:1904.03594* (2019).

[161] Robinson, P. J., Valentine, M. E., Granmoe, A., Drichko, N., Chamorro, J. R., Rosa, P. F., McQueen, T. M., and Alexandrova, A. N. Dynamical Bonding Driving Mixed Valency in a Metal Boride, *Angewandte Chemie* **132**(27), 11089–11095 (2020).

[162] Skinner, B. Properties of the donor impurity band in mixed valence insulators, *Phys. Rev. Materials* **3**(10), 104601 (2019).

[163] Terashima, T. T., Matsuda, Y. H., Kohama, Y., Ikeda, A., Kondo, A., Kindo, K., and Iga, F. Magnetic-Field-Induced Kondo Metal Realized in YbB_{12}, *Phys. Rev. Lett.* **120**(25), 257206 (2018).

[164] Fisk, Z., Matthias, B. T., and Corenzwit, E. Rare earth impurities in YB_6 and ZrB_{12}, *Proceedings of the National Academy of Sciences* **64**(4), 1151–1154 (1969).

[165] Kasaya, M., Iga, F., Negishi, K., Nakai, S., and Kasuya, T. A new and typical valence fluctuating system, YbB_{12}, *Journal of Magnetism and Magnetic Materials* **31**, 437–438 (1983).

[166] Sugiyama, K., Iga, F., Kasaya, M., Kasuya, T., and Date, M. Field-induced metallic state in YbB_{12} under high magnetic field, *Journal of the Physical Society of Japan* **57**(11), 3946–3953 (1988).

[167] Iga, F., Kasaya, M., Suzuki, H., Okayama, Y., Takahashi, H., and Mori, N. Transport properties under high pressure of the dense Kondo compounds CePdSn and YbB_{12}, *Physica B: Condensed Matter* **186**, 419–421 (1993).

[168] Iga, F., Shimizu, N., and Takabatake, T. Single crystal growth and physical properties of Kondo insulator YbB_{12}, *Journal of magnetism and magnetic materials* **177**, 337–338 (1998).

[169] Iga, F., Kasaya, M., and Kasuya, T. Specific heat measurements of YbB12 and $Yb_xLu_{1-x}B_{12}$, *Journal of Magnetism and Magnetic Materials* **76**, 156–158 (1988).

[170] Iga, F., Takakuwa, Y., Takahashi, T., Kasaya, M., Kasuya, T., and Sagawa, T. XPS study of rare earth dodecaborides: TmB_{12}, YbB_{12} and LuB_{12}, *Solid state communications* **50**(10), 903–905 (1984).

[171] Susaki, T., Sekiyama, A., Kobayashi, K., Mizokawa, T., Fujimori, A., Tsunekawa, M., Muro, T., Matsushita, T., Suga, S., Ishii, H., et al. Low-energy electronic structure of the Kondo insulator YbB_{12}, *Phys. Rev. Lett.* **77**(20), 4269 (1996).

[172] Kim, D., Grant, T., and Fisk, Z. Limit cycle and anomalous capacitance in the Kondo insulator SmB_6, *Phys. Rev. Lett.* **109**(9), 096601 (2012).

[173] Weng, H., Zhao, J., Wang, Z., Fang, Z., and Dai, X. Topological crystalline kondo insulator in mixed valence ytterbium borides, *Phys. Rev. Lett.* **112**, 016403 (2014).

[174] Hagiwara, K., Ohtsubo, Y., Matsunami, M., Ideta, S.-i., Tanaka, K., Miyazaki, H., Rault, J. E., Le Fevre, P., Bertran, F., Taleb-Ibrahimi, A., et al. Surface Kondo effect and non-trivial metallic state of the Kondo insulator YbB_{12}, *Nature communications* **7**, 12690 (2016).

[175] Sato, Y., Xiang, Z., Kasahara, Y., Taniguchi, T., Kasahara, S., Chen, L., Asaba, T., Tinsman, C., Murayama, H., Tanaka, O., et al. Unconventional thermal metallic state of charge-neutral fermions in an insulator, *Nature Physics* (2019).

[176] Kasaya, M., Iga, F., Takigawa, M., and Kasuya, T. Mixed valence properties of YbB_{12}, *Journal of Magnetism and Magnetic Materials* **47**, 429–435 (1985).

[177] Susaki, T., Takeda, Y., Arita, M., Mamiya, K., Fujimori, A., Shimada, K., Namatame, H., Taniguchi, M., Shimizu, N., Iga, F., et al. Temperature-dependent high-resolution photoemission study of the Kondo insulator YbB_{12}, *Phys. Rev. Lett.* **82**(5), 992 (1999).

[178] Flachbart, K., Gabáni, S., Neumaier, K., Paderno, Y., Pavlík, V., Schuberth, E., and Shitsevalova, N. Specific heat of SmB_6 at very low temperatures, *Physica B: Condensed Matter* **378**, 610–611 (2006).

[179] Iga, F., Suga, K., Takeda, K., Michimura, S., Murakami, K., Takabatake, T., and Kindo, K. Anisotropic magnetoresistance and collapse of the energy gap in $Yb_{1-x}Lu_xB_{12}$. In *Journal of Physics: Conference Series*, volume 200, 012064. IOP Publishing, (2010).

[180] Heinecke, M., Winzer, K., N. J. K. H., Grieb, H., Flachbart, K., and Paderno, Y. B. Quantum oscillations and the Fermi surface of LuB_{12}, *Z. Physik B* **98**, 231–237 (1995).

[181] Okuda, N., Suzuki, T., Ishii, I., Sayaka, H., Iga, F., Takabatake, T., Fujita, T., Kadomatsu, H., and Harima, H. Elastic quantum oscillation of LuB_{12}, *Physica B* **281–282**, 756–757 (2000).

[182] Yanase, A. and Harima, H. Band calculations on YbB_{12}, SmB_6 and CeNiSn, *Progress of Theoretical Physics Supplement* **108**, 19–25 (1992).

[183] Antonov, V., Harmon, B., and Yaresko, A. Electronic structure of mixed-valence semiconductors in the LSDA+ U approximation. II. SmB_6 and YbB_{12}, *Phys. Rev. B* **66**(16), 165209 (2002).

[184] Harima, H., Yanase, A., and Kasuya, T. Energy bandstructure of YB_{12} and LuB_{12}, *Journal of Magnetism and Magnetic Materials* **47**, 567–569 (1985).

[185] Kayama, S., Tanaka, S., Miyake, A., Kagayama, T., Shimizu, K., and Iga, F. Pressure Induced Insulator-to-Metal Transition at 170 GPa of Kondo Semiconductor YbB_{12}. In *Proceedings of the International Conference on Strongly Correlated Electron Systems (SCES2013)*, 012024, (2014).

[186] Hartstein, M., Hsu, Y.-T., Modic, K. A., Porras, J., Loew, T., Le Tacon, M., Zuo, H., Wang, J., Zhu, Z., Chan, M. K., McDondald, R. D., Lonzarich, G. G., Keimer, B., Sebastian, S. E., and Harrison, N. Hard antinodal gap revealed by quantum oscillations in the pseudogap regime of underdoped high-T_c superconductors, *Nature Physics* **16**, 841–847 (2020).

[187] Timusk, T. and Statt, B. The pseudogap in high-temperature superconductors: an experimental survey, *Reports on Progress in Physics* **62**(1), 61 (1999).

[188] Norman, M. R., Pines, D., and Kallin, C. The pseudogap: friend or foe of high-T_c?, *Advances in Physics* **54**(8), 715–733 (2005).

[189] Sebastian, S. E., Harrison, N., Palm, E., Murphy, T., Mielke, C., Liang, R., Bonn, D., Hardy, W., and Lonzarich, G. A multi-component Fermi surface in the vortex state of an underdoped high-T_c superconductor, *Nature* **454**(7201), 200 (2008).

[190] Barišić, N., Chan, M. K., Li, Y., Yu, G., Zhao, X., Dressel, M., Smontara, A., and Greven, M. Universal sheet resistance and revised phase diagram of the cuprate high-temperature superconductors, *Proceedings of the National Academy of Sciences* **110**(30), 12235–12240 (2013).

[191] Marshall, D., Dessau, D., Loeser, A., Park, C., Matsuura, A., Eckstein, J. N., Bozovic, I., Fournier, P., Kapitulnik, A., Spicer, W., et al. Unconventional electronic structure evolution with hole doping in $Bi_2Sr_2CaCu_2O_{8+\delta}$: Angle-resolved photoemission results, *Phys. Rev. Lett.* **76**(25), 4841 (1996).

[192] Norman, M., Ding, H., Randeria, M., Campuzano, J., Yokoya, T., Takeuchi, T., Takahashi, T., Mochiku, T., Kadowaki, K., Guptasarma, P., et al. Destruction of the Fermi surface in underdoped high-T_c superconductors, *Nature* **392**(6672), 157–160 (1998).

[193] Hossain, M., Mottershead, J., Fournier, D., Bostwick, A., McChesney, J., Rotenberg, E., Liang, R., Hardy, W., Sawatzky, G., Elfimov, I., et al. In situ doping control of the surface of high-temperature superconductors, *Nature Physics* **4**(7), 527–531 (2008).

[194] Fujita, K., Kim, C. K., Lee, I., Lee, J., Hamidian, M., Firmo, I., Mukhopadhyay, S., Eisaki, H., Uchida, S., Lawler, M., et al. Simultaneous transitions in cuprate momentum-space topology and electronic symmetry breaking, *Science* **344**(6184), 612–616 (2014).

[195] Platé, M., Mottershead, J., Elfimov, I., Peets, D., Liang, R., Bonn, D., Hardy, W., Chiuzbaian, S., Falub, M., Shi, M., et al. Fermi surface and quasiparticle excitations of overdoped $Tl_2Ba_2CuO_{6+\delta}$, *Phys. Rev. Lett.* **95**(7), 077001 (2005).

[196] Vignolle, B., Carrington, A., Cooper, R., French, M., Mackenzie, A., Jaudet, C., Vignolles, D., Proust, C., and Hussey, N. Quantum oscillations in an overdoped high-T_c superconductor, *Nature* **455**(7215), 952–955 (2008).

[197] Riggs, S. C., Vafek, O., Kemper, J., Betts, J., Migliori, A., Balakirev, F., Hardy, W., Liang, R., Bonn, D., and Boebinger, G. Heat capacity through the magnetic-field-induced resistive transition in an underdoped high-temperature superconductor, *Nature Physics* **7**(4), 332 (2011).

[198] Laliberté, F., Chang, J., Doiron-Leyraud, N., Hassinger, E., Daou, R., Rondeau, M., Ramshaw, B., Liang, R., Bonn, D., Hardy, W., et al. Fermi-surface reconstruction by stripe order in cuprate superconductors, *Nature communications* **2**(1), 1–6 (2011).

[199] Sebastian, S. E., Harrison, N., Altarawneh, M., Liang, R., Bonn, D., Hardy, W., and Lonzarich, G. Fermi-liquid behavior in an underdoped high-T_c superconductor, *Phys. Rev. B* **81**(14), 140505 (2010).

[200] Ramshaw, B., Sebastian, S., McDonald, R., Day, J., Tan, B., Zhu, Z., Betts, J., Liang, R., Bonn, D., Hardy, W., et al. Quasiparticle mass enhancement approaching optimal doping in a high-T_c superconductor, *Science* **348**(6232), 317–320 (2015).

[201] Blanco-Canosa, S., Frano, A., Schierle, E., Porras, J., Loew, T., Minola, M., Bluschke, M., Weschke, E., Keimer, B., and Le Tacon, M. Resonant X-ray scattering study of charge-density wave correlations in $\mathrm{YBa_2Cu_3O_{6+x}}$, *Phys. Rev. B* **90**(5), 054513 (2014).

[202] Sebastian, S. E. and Proust, C. Quantum oscillations in hole-doped cuprates, *Annu. Rev. Condens. Matter Phys.* **6**(1), 411–430 (2015).

[203] Sebastian, S. E., Harrison, N., and Lonzarich, G. G. Towards resolution of the Fermi surface in underdoped high-T_c superconductors, *Reports on Progress in Physics* **75**(10), 102501 (2012).

[204] Sebastian, S. E., Harrison, N., Balakirev, F., Altarawneh, M., Goddard, P., Liang, R., Bonn, D., Hardy, W., and Lonzarich, G. Normal-state nodal electronic structure in underdoped high-T_c copper oxides, *Nature* **511**(7507), 61 (2014).

[205] Ghiringhelli, G., Le Tacon, M., Minola, M., Blanco-Canosa, S., Mazzoli, C., Brookes, N., De Luca, G., Frano, A., Hawthorn, D., He, F., et al. Long-range incommensurate charge fluctuations in $\mathrm{(Y,Nd)Ba_2Cu_3O_{6+x}}$, *Science* **337**(6096), 821–825 (2012).

[206] Chang, J., Blackburn, E., Holmes, A., Christensen, N. B., Larsen, J., Mesot, J., Liang, R., Bonn, D., Hardy, W., Watenphul, A., et al. Direct observation of competition between superconductivity and charge density wave order in $\mathrm{YBa_2Cu_3O_{6.67}}$, *Nature Physics* **8**(12), 871–876 (2012).

[207] Tan, B., Harrison, N., Zhu, Z., Balakirev, F., Ramshaw, B., Srivastava, A., Sabok-Sayr, S., Dabrowski, B., Lonzarich, G. G., and Sebastian, S. E. Fragile charge order in the

nonsuperconducting ground state of the underdoped high-temperature superconductors, *Proceedings of the National Academy of Sciences* **112**(31), 9568–9572 (2015).

[208] Comin, R. and Damascelli, A. Resonant X-ray scattering studies of charge order in cuprates, *Annual Review of Condensed Matter Physics* **7**, 369–405 (2016).

[209] Allais, A., Chowdhury, D., and Sachdev, S. Connecting high-field quantum oscillations to zero-field electron spectral functions in the underdoped cuprates, *Nature communications* **5**(1), 1–10 (2014).

[210] Harrison, N. and Sebastian, S. Protected nodal electron pocket from multiple-q ordering in underdoped high temperature superconductors, *Phys. Rev. Lett.* **106**(22), 226402 (2011).

[211] Millis, A. J. and Norman, M. Antiphase stripe order as the origin of electron pockets observed in 1/8-hole-doped cuprates, *Phys. Rev. B* **76**(22), 220503 (2007).

[212] Yao, H., Lee, D.-H., and Kivelson, S. A. Fermi-surface reconstruction in a smectic phase of a high-temperature superconductor, *Phys. Rev. B* **84**(1), 012507 (2011).

[213] Lee, P. A., Nagaosa, N., and Wen, X.-G. Doping a Mott insulator: Physics of high-temperature superconductivity, *Reviews of Modern Physics* **78**(1), 17 (2006).

[214] Yang, K.-Y., Rice, T., and Zhang, F.-C. Phenomenological theory of the pseudogap state, *Phys. Rev. B* **73**(17), 174501 (2006).

[215] Harrison, N. Robustness of the biaxial charge density wave reconstructed electron pocket against short-range spatial antiferromagnetic fluctuations, *Phys. Rev. B* **97**(24), 245150 (2018).

[216] Dai, Z., Zhang, Y.-H., Senthil, T., and Lee, P. A. Pair-density waves, charge-density waves, and vortices in high-T_c cuprates, *Phys. Rev. B* **97**, 174511 (2018).

[217] Doiron-Leyraud, N., Badoux, S., De Cotret, S. R., Lepault, S., LeBoeuf, D., Laliberté, F., Hassinger, E., Ramshaw, B., Bonn, D., Hardy, W., et al. Evidence for a small hole pocket in the Fermi surface of underdoped $YBa_2Cu_3O_y$, *Nature communications* **6**(1), 1–7 (2015).

[218] Yu, F., Hirschberger, M., Loew, T., Li, G., Lawson, B. J., Asaba, T., Kemper, J., Liang, T., Porras, J., Boebinger, G. S., Singleton, J., Keimer, B., Li, L., , and Ong, N. P. Magnetic phase diagram of underdoped $YBa_2Cu_3O_y$ inferred from torque magnetization and thermal conductivity, *Proceedings of the National Academy of Sciences* **113**(45), 12667–12672 (2016).

[219] Harrison, N. and Sebastian, S. Magnetotransport signatures of a single nodal electron pocket constructed from Fermi arcs, *Phys. Rev. B* **92**(22), 224505 (2015).

[220] Wosnitza, J., Wanka, S., Hagel, J., Balthes, E., Harrison, N., Schlueter, J., Kini, A., Geiser, U., Mohtasham, J., Winter, R. W., et al. Two-dimensional fermi liquid with fixed chemical potential, *Phys. Rev. B* **61**(11), 7383 (2000).

[221] Potts, A., Shepherd, R., Herrenden-Harker, W., Elliott, M., Jones, C., Usher, A., Jones, G., Ritchie, D., Linfield, E., and Grimshaw, M. Magnetization studies of Landau level broadening in two-dimensional electron systems, *Journal of Physics: Condensed Matter* **8**(28), 5189 (1996).

[222] Harrison, N., Balicas, L., Brooks, J., and Tokumoto, M. Critical state in a low-dimensional metal induced by strong magnetic fields, *Phys. Rev. B* **62**(21), 14212 (2000).

[223] Keimer, B., Kivelson, S. A., Norman, M. R., Uchida, S., and Zaanen, J. From quantum matter to high-temperature superconductivity in copper oxides, *Nature* **518**(7538), 179–186 (2015).

[224] Bean, C. P. Magnetization of high-field superconductors, *Reviews of Modern Physics* **36**(1), 31 (1964).

[225] Mackenzie, A., Julian, S., Lonzarich, G., Carrington, A., Hughes, S., Liu, R., and Sinclair, D. Resistive upper critical field of $Tl_2Ba_2CuO_6$ at low temperatures and high magnetic fields, *Phys. Rev. Lett.* **71**(8), 1238 (1993).

[226] Campbell, A. M. and Evetts, J. E. *Critical currents in superconductors*. Taylor & Francis, (1972).

[227] Shakeripour, H., Petrovic, C., and Taillefer, L. Heat transport as a probe of superconducting gap structure, *New Journal of Physics* **11**(5), 055065 (2009).

[228] Wu, T., Mayaffre, H., Krämer, S., Horvatić, M., Berthier, C., Kuhns, P. L., Reyes, A. P., Liang, R., Hardy, W., Bonn, D., et al. Emergence of charge order from the vortex state of a high-temperature superconductor, *Nature communications* **4**(1), 1–6 (2013).

[229] Chang, J., Blackburn, E., Ivashko, O., Holmes, A., Christensen, N. B., Hücker, M., Liang, R., Bonn, D., Hardy, W., Rütt, U., et al. Magnetic field controlled charge density wave coupling in underdoped $YBa_2Cu_3O_{6+x}$, *Nature communications* **7**, 11494 (2016).

[230] Marcenat, C., Demuer, A., Beauvois, K., Michon, B., Grockowiak, A., Liang, R., Hardy, W., Bonn, D., and Klein, T. Calorimetric determination of the magnetic phase diagram of underdoped ortho II $YBa_2Cu_3O_{6.54}$ single crystals, *Nature communications* **6**, 7927 (2015).

[231] Kačmarčík, J., Vinograd, I., Michon, B., Rydh, A., Demuer, A., Zhou, R., Mayaffre, H., Liang, R., Hardy, W., Bonn, D., et al. Unusual Interplay between Superconductivity and Field-Induced Charge Order in $YBa_2Cu_3O_y$, *Phys. Rev. Lett.* **121**(16), 167002 (2018).

[232] Wang, Y., Li, L., and Ong, N. P. Nernst effect in high-T_c superconductors, *Phys. Rev. B* **73**(2), 024510 (2006).

[233] Anderson, P. W. and Kim, Y. Hard superconductivity: theory of the motion of Abrikosov flux lines, *Reviews of Modern Physics* **36**(1), 39 (1964).

[234] Giamarchi, T. and Bhattacharya, S. Vortex phases. In *High Magnetic Fields*, 314–360. Springer (2002).

[235] Giamarchi, T. and Le Doussal, P. Elastic theory of flux lattices in the presence of weak disorder, *Phys. Rev. B* **52**(2), 1242 (1995).

[236] Klein, T., Joumard, I., Blanchard, S., Marcus, J., Cubitt, R., Giamarchi, T., and Le Doussal, P. A Bragg glass phase in the vortex lattice of a type II superconductor, *Nature* **413**(6854), 404–406 (2001).

[237] Stamp, P. C. E., Forro, L., and Ayache, C. Kosterlitz-Thouless transition of fluxless solitons in superconducting $YBa_2Cu_3O_{7-\delta}$ single crystals, *Phys. Rev. B* **38**, 2847–2850 Aug (1988).

[238] Fiory, A. T., Hebard, A. F., Mankiewich, P. M., and Howard, R. E. Renormalization of the Mean-Field Superconducting Penetration Depth in Epitaxial $YBa_2Cu_3O_7$ Films, *Phys. Rev. Lett.* **61**, 1419–1422 Sep (1988).

[239] Matsuda, Y., Komiyama, S., Onogi, T., Terashima, T., Shimura, K., and Bando, Y. Thickness dependence of the Kosterlitz-Thouless transition in ultrathin $YBa_2Cu_3O_{7-\delta}$ films, *Phys. Rev. B* **48**, 10498–10503 Oct (1993).

[240] Li, Q., Hücker, M., Gu, G., Tsvelik, A., and Tranquada, J. Two-dimensional superconducting fluctuations in stripe-ordered $La_{1.875}Ba_{0.125}CuO_4$, *Phys. Rev. Lett.* **99**(6), 067001 (2007).

[241] Minnhagen, P. The two-dimensional Coulomb gas, vortex unbinding, and superfluid-superconducting films, *Reviews of Modern Physics* **59**(4), 1001 (1987).

[242] Strachan, D., Lobb, C., and Newrock, R. Dynamic scaling and two-dimensional high-T_c superconductors, *Phys. Rev. B* **67**(17), 174517 (2003).

[243] Halperin, B. and Nelson, D. R. Resistive transition in superconducting films, *Journal of Low Temperature Physics* **36**(5-6), 599–616 (1979).

[244] Kadin, A., Epstein, K., and Goldman, A. M. Renormalization and the Kosterlitz-Thouless transition in a two-dimensional superconductor, *Phys. Rev. B* **27**(11), 6691 (1983).

[245] Ammirata, S., Friesen, M., Pierson, S. W., Gorham, L. A., Hunnicutt, J. C., Trawick, M., and Keener, C. Dynamic scaling for 2D superconductors in zero magnetic field, *Physica C: Superconductivity* **313**(3-4), 225–231 (1999).

[246] Blatter, G., Feigel'man, M. V., Geshkenbein, V. B., Larkin, A. I., and Vinokur, V. M. Vortices in high-temperature superconductors, *Reviews of Modern Physics* **66**(4), 1125 (1994).

[247] Gammel, P., Schneemeyer, L., and Bishop, D. SQUID picovoltometry of $YBa_2Cu_3O_7$ single crystals: Evidence for a finite-temperature phase transition in the high-field vortex state, *Phys. Rev. Lett.* **66**(7), 953 (1991).

[248] Koch, R., Foglietti, V., Gallagher, W. J., Koren, G., Gupta, A., and Fisher, M. Experimental evidence for vortex-glass superconductivity in Y-Ba-Cu-O, *Phys. Rev. Lett.* **63**(14), 1511 (1989).

[249] Pierson, S. W., Friesen, M., Ammirata, S., Hunnicutt, J. C., and Gorham, L. A. Dynamic scaling for two-dimensional superconductors, Josephson-junction arrays, and superfluids, *Phys. Rev. B* **60**(2), 1309 (1999).

[250] Repaci, J., Kwon, C., Li, Q., Jiang, X., Venkatessan, T., Glover III, R., Lobb, C., and Newrock, R. Absence of a Kosterlitz-Thouless transition in ultrathin $YBa_2Cu_3O_{7-\delta}$ films, *Phys. Rev. B* **54**(14), R9674 (1996).

[251] Garland, J. and Lee, H. J. Influence of a magnetic field on the two-dimensional phase transition in thin-film superconductors, *Phys. Rev. B* **36**(7), 3638 (1987).

[252] Reyren, N., Thiel, S., Caviglia, A., Kourkoutis, L. F., Hammerl, G., Richter, C., Schneider, C., Kopp, T., Rüetschi, A.-S., Jaccard, D., et al. Superconducting interfaces between insulating oxides, *Science* **317**(5842), 1196–1199 (2007).

[253] Xing, Y., Zhang, H.-M., Fu, H.-L., Liu, H., Sun, Y., Peng, J.-P., Wang, F., Lin, X., Ma, X.-C., Xue, Q.-K., et al. Quantum Griffiths singularity of superconductor-metal transition in Ga thin films, *Science* **350**(6260), 542–545 (2015).

[254] Baity, P., Shi, X., Shi, Z., Benfatto, L., and Popović, D. Effective two-dimensional thickness for the Berezinskii-Kosterlitz-Thouless-like transition in a highly underdoped $La_{2-x}Sr_xCuO_4$, *Phys. Rev. B* **93**(2), 024519 (2016).

[255] Frey, E., Nelson, D. R., and Fisher, D. S. Interstitials, vacancies, and supersolid order in vortex crystals, *Phys. Rev. B* **49**(14), 9723 (1994).

[256] Pereg-Barnea, T., Turner, P., Harris, R., Mullins, G., Bobowski, J., Raudsepp, M., Liang, R., Bonn, D., and Hardy, W. Absolute values of the London penetration depth in $YBa_2Cu_3O_{6+y}$ measured by zero field ESR spectroscopy on Gd doped single crystals, *Phys. Rev. B* **69**(18), 184513 (2004).

[257] Jiang, H., Yuan, T., How, H., Widom, A., Vittoria, C., and Drehman, A. Measurements of anisotropic characteristic lengths in YBCO films at microwave frequencies, *Journal of applied physics* **73**(10), 5865–5867 (1993).

[258] Hsu, Y.-T., Hartstein, M., Davies, A. J., Hickey, A. J., Chan, M. K., Porras, J., Loew, T., Taylor, S. V., Liu, H., Eaton, A. G., Le Tacon, M., Zuo, H., Wang, J., Zhu, Z., Lonzarich, G. G., Keimer, B., Harrison, N., and Sebastian, S. E. Unconventional quantum vortex matter state hosts quantum oscillations in the underdoped high-temperature cuprate superconductors, *Proceedings of the National Academy of Sciences* **118**(7), e2021216118 (2021).

[259] Hüfner, S., Hossain, M., Damascelli, A., and Sawatzky, G. Two gaps make a high-temperature superconductor?, *Reports on Progress in Physics* **71**(6), 062501 (2008).

[260] Yeh, N.-C., Chen, C.-T., Hammerl, G., Mannhart, J., Tajima, S., Yoshida, K., Schmehl, A., Schneider, C., and Schulz, R. Spatial homogeneity and doping dependence of quasiparticle tunneling spectra in cuprate superconductors, *Physica C: Superconductivity and its applications* **364**, 450–457 (2001).

[261] Dai, P., Mook, H. A., Hunt, R. D., and Doğan, F. Evolution of the resonance and incommensurate spin fluctuations in superconducting $YBa_2Cu_3O_{6+x}$, *Phys. Rev. B* **63**(5), 054525 (2001).

[262] Yu, G., Li, Y., Motoyama, E., and Greven, M. A universal relationship between magnetic resonance and superconducting gap in unconventional superconductors, *Nature Physics* **5**(12), 873 (2009).

[263] Sebastian, S. E., Harrison, N., Liang, R., Bonn, D., Hardy, W., Mielke, C., and Lonzarich, G. Quantum oscillations from nodal bilayer magnetic breakdown in the underdoped high temperature superconductor $YBa_2Cu_3O_{6+x}$, *Phys. Rev. Lett.* **108**(19), 196403 (2012).

[264] Janssen, T., Haworth, C., Hayden, S., Meeson, P., Springford, M., and Wasserman, A. Quantitative investigation of the de Haas-van Alphen effect in the superconducting state, *Phys. Rev. B* **57**(18), 11698 (1998).

[265] Terashima, T., Haworth, C., Takeya, H., Uji, S., Aoki, H., and Kadowaki, K. Small superconducting gap on part of the Fermi surface of YNi_2B_2C from the de Haas-van Alphen effect, *Phys. Rev. B* **56**(9), 5120 (1997).

[266] Bergk, B., Drechsler, S., Canfield, P., and Wosnitza, J. Detailed study of the de Haas-van Alphen effect in the Shubnikov state of $LuNi_2B_2C$, *The European Physical Journal B* **85**(2), 57 (2012).

[267] Maki, K. Quantum oscillation in vortex states of type-II superconductors, *Phys. Rev. B* **44**(6), 2861 (1991).

[268] Miyake, K. de Haas-van Alphen oscillations in superconducting states as a probe of gap anisotropy, *Physica B: Condensed Matter* **186**, 115–117 (1993).

[269] Yasui, K. and Kita, T. Theory of the de Haas–van Alphen effect in type-II superconductors, *Phys. Rev. B* **66**(18), 184516 (2002).

[270] Norman, M. and Davis, J. S. Quantum oscillations in a biaxial pair density wave state, *Proceedings of the National Academy of Sciences* **115**(21), 5389–5391 (2018).

[271] Dai, Z., Senthil, T., and Lee, P. A. Modeling the pseudogap metallic state in cuprates: Quantum disordered pair density wave, *Phys. Rev. B* **101**, 064502 Feb (2020).

[272] Yu, Y. and Kivelson, S. A. Fragile superconductivity in the presence of weakly disordered charge density waves, *Phys. Rev. B* **99**(14), 144513 (2019).

[273] Lee, D., Dubeck, L., and Rothwarf, F. Transverse energy gap in 2H-NbSe$_2$, *Physics Letters A* **53**(5), 379–380 (1975).

[274] Corcoran, R., Harrison, N., Haworth, C., Hayden, S., Meeson, P., Springford, M., and Van der Wel, P. De Haas-van Alphen effect in the superconducting state, *Physica B: Condensed Matter* **206**, 534–541 (1995).

[275] Hackl, R., Kaiser, R., and Schicktanz, S. Gap mode, superconducting gap and phonon mode in V$_3$Si and Nb$_3$Sn, *Journal of Physics C: Solid State Physics* **16**(9), 1729 (1983).

[276] Ekino, T., Fujii, H., Kosugi, M., Zenitani, Y., and Akimitsu, J. Superconducting energy gap in YNi$_2$B$_2$C, *Physica C: Superconductivity* **235**, 2529–2530 (1994).

[277] De Wilde, Y., Iavarone, M., Welp, U., Metlushko, V., Koshelev, A. E., Aranson, I., Crabtree, G. W., and Canfield, P. C. Scanning tunneling microscopy observation of a square Abrikosov lattice in LuNi$_2$B$_2$C, *Phys. Rev. Lett.* **78**(22), 4273 (1997).

[278] Fletcher, J., Carrington, A., Kazakov, S., and Karpinski, J. Damping of the de Haas–van Alphen oscillations in the superconducting state of MgB$_2$, *Phys. Rev. B* **70**(14), 144501 (2004).

[279] Hedo, M., Inada, Y., Sakurai, K., Yamamoto, E., Haga, Y., Ōnuki, Y., Takahashi, S., Higuchi, M., Maehira, T., and Hasegawa, A. Magnetoresistance and de Haas-van Alphen oscillation in normal and superconducting CeRu$_2$, *Philosophical Magazine B* **77**(4), 975–1000 (1998).

[280] Ekino, T., Fujii, H., Nakama, T., and Yagasaki, K. Electron tunneling into superconducting CeRu$_2$, *Phys. Rev. B* **56**(13), 7851 (1997).

[281] Inada, Y., Yamagami, H., Haga, Y., Sakurai, K., Tokiwa, Y., Honma, T., Yamamoto, E., Ōnuki, Y., and Yanagisawa, T. Fermi surface and de Haas-van Alphen oscillation in both the normal and superconducting mixed states of UPd$_2$Al$_3$, *Journal of the Physical Society of Japan* **68**(11), 3643–3654 (1999).

[282] Aarts, J., Volodin, A., Menovsky, A., Nieuwenhuys, G., and Mydosh, J. Tunnelling spectroscopy on the heavy-fermion superconductors UPd$_2$Al$_3$ and UNi$_2$Al$_3$ in the normal state, *Europhysics Letters* **26**(3), 203 (1994).

[283] Jourdan, M., Huth, M., and Adrian, H. Superconductivity mediated by spin fluctuations in the heavy-fermion compound UPd_2Al_3, *Nature* **398**(6722), 47 (1999).

[284] Ohkuni, H., Inada, Y., Tokiwa, Y., Sakurai, K., Settai, R., Honma, T., Haga, Y., Yamamoto, E., Ōnuki, Y., Yamagami, H., et al. Fermi surface properties and de Haas–van Alphen oscillation in both the normal and superconducting mixed states of URu_2Si_2, *Philosophical Magazine B* **79**(7), 1045–1077 (1999).

[285] Naidyuk, Y. G., Löhneysen, H. v., Goll, G., Yanson, I., and Menovsky, A. Anisotropy of the superconducting energy gap in URu_2Si_2 studied by point-contact spectroscopy, *Europhysics Letters* **33**(7), 557 (1996).

[286] Morales, F. and Escudero, R. Pseudogap and superconducting energy gap in single crystals of URu_2Si_2 by point contact spectroscopy, *Journal of Low Temperature Physics* **154**(1-2), 68–75 (2009).

[287] Van der Wel, P., Caulfield, J., Hayden, S., Singleton, J., Springford, M., Meeson, P., Hayes, W., Kurmoo, M., and Day, P. De Haas-van Alphen oscillations near B_c2 in the organic superconductor κ-$(ET)_2Cu(NCS)_2$, *Synthetic Metals* **70**(1-3), 831–832 (1995).

[288] Sasaki, T., Biberacher, W., Neumaier, K., Hehn, W., Andres, K., and Fukase, T. Quantum liquid of vortices in the quasi-two-dimensional organic superconductor κ-$(BEDT\text{-}TTF)_2Cu(NCS)_2$, *Phys. Rev. B* **57**(17), 10889 (1998).

[289] Arai, T., Ichimura, K., Nomura, K., Takasaki, S., Yamada, J., Nakatsuji, S., and Anzai, H. Tunneling spectroscopy on the organic superconductor κ-$(BEDT\text{-}TTF)_2Cu(NCS)_2$ using STM, *Phys. Rev. B* **63**(10), 104518 (2001).